

# **Investigation on Compressive Devices Based on Dielectric Elastomer Actuators**

**by  
Shahram Pourazadi**

M.A.Sc., University of British Columbia, 2012

B.Sc., Isfahan University of Technology, 2010

Thesis Submitted in Partial Fulfillment of the  
Requirements for the Degree of  
Doctor of Philosophy

in the  
School of Engineering Science  
Faculty of Applied Sciences

© Shahram Pourazadi 2019  
SIMON FRASER UNIVERSITY  
Fall 2019

Copyright in this work rests with the author. Please ensure that any reproduction or re-use is done in accordance with the relevant national copyright legislation.

# Approval

**Name:** **Shahram Pourazadi**

**Degree:** **Doctor of Philosophy**

**Title:** **Investigation on Compressive Devices Based on Dielectric Elastomer Actuators**

**Examining Committee:** **Chair:** Bernhard Rabus  
Professor

**Carlo Menon**  
Senior Supervisor  
Professor

**Ash Parameswaran**  
Supervisor  
Professor

**Michael Adachi**  
Supervisor  
Assistant Professor

**Siamak Arzanpour**  
Internal Examiner  
Associate Professor  
Mechatronic Systems Engineering

**Federico Carpi**  
External Examiner  
Associate Professor  
Industrial Engineering  
University of Florence

**Date Defended/Approved:** November 20, 2019

## Abstract

Dielectric elastomer actuators (DEAs) are an emerging technology from the larger class of artificial muscle actuators, showing interesting properties such as softness and large actuation strains. A DEA can be used to create various types of motions (such as planar, rotary, and bending) and contact forces (such as tension, biaxial compression, and bending moment). Due to its interesting properties, there are a growing number of studies on improving DEA applicability, reliability, and characteristics. Additionally, despite limited commercial use, there is a growing global push toward commercializing DEA in various sectors.

In this thesis, in an effort to investigate practical applications of DEAs, their functionality is studied in applications where compressive forces are exerted by the actuator. Two different modalities in which DEAs could apply compressive forces to an encompassed object are identified. To narrow the focus of the thesis, a practical application is introduced and investigated for each modality. The first practical application, based on the first modality, introduces the use of DEAs as a compression bandage to improve blood circulation in the human leg. The proposed compression bandage could potentially enable a controlled variable compression around the lower leg. The second practical application, based on the second modality, proposes a novel gripper that uses DEAs as a mean to apply a soft touch on objects. The proposed gripper can apply up to 2N of grasping force to select objects. The gripper may be adopted as an end effectors for collaborative robotic arms, where a human operator is collaborating with the robotic arm to handle a delicate object.

Typically, DEAs are actuated using high electrical voltages of several kilovolts. This operating voltage gives rise to a safety concern for practical applications where DEAs are sought to be operated in proximity to the human body. Since the two aforementioned applications require or may require the operation of DEAs close to the human body, it is very important to study the electrical safety of DEAs and investigate methods to manage the risk of their high operating voltages. The last part of this thesis discusses the electrical safety of DEAs in scenarios where DEA circuitry is in contact with the human body and shows that they can be safely used. Critical parameters for identification of the electrical safety of DEAs are also introduced to assist in designing safer DEAs for such applications.

**Keywords:** Dielectric elastomer actuators; Active compression bandages; Soft grasping; Smart materials

With Love and Respect to My Family

&

to the Transcendent Force That Drives Me and Many Others to  
Discover Knowledge, Truth, and Facts.

## Acknowledgments

Foremost, I would like to thank my senior supervisor, Professor Carlo Menon, for all his guidance and efforts. Professor Menon's leadership, patience, attention, and smartness not only motivated and encouraged me throughout my work at SFU, but also inspired me to become a better researcher, a better leader, and a better person. I would like to thank Professor Menon for all the opportunities that he exposed to me.

I would like to thank my committee members, Professor Ash M. Parameswaran, Professor Michael Adachi, Professor Siamak Arzanpour, and Professor Federico Carpi for their valuable time, consideration, and feedback for my thesis. I should especially thank Professor Parameswaran for his energetic conversations and kind helps throughout my Ph.D. studies.

I would like to thank my collaborators Professor Mehrdad Moallem and his researcher Dr. Ali Shagerdmootaab for sharing their time, knowledge and work with me. I would also like to thank Dr. Victoria Claydon and Dr. Andrew Blaber from the SFU BPK department for their valuable collaboration during my Ph.D. work.

I am grateful to my labmates at Menrva's research group, particularly, Mahan Rahimi, Dr. Ausama H. Ahmad, Dr. Yasong Li, Dr. Jeff Krahn, Dr. Sadegh Ahmadi, Dr. Mojtaba Komeili, Juan Pablo Diaz Tellez, and Jamal Bahari for providing a collaborative and pleasant research environment.

This work was supported in part by the Natural Sciences and Engineering Research Council of Canada (NSERC), the Canadian Institutes of Health Research (CIHR), the Michael Smith Foundation for Health Research (MSFHR), and Canada Research Chair (CRC) program.

Heartfelt thanks to my parents, brothers, and sister, and last but not least my lovely wife, Banafsheh, for their love, support, and kindness.

# Table of Contents

Approval.....	ii
Abstract.....	iii
Dedication.....	iv
Acknowledgments.....	v
Table of Contents.....	vi
List of Tables.....	ix
List of Figures.....	x
List of Acronyms.....	xiii
<b>Chapter 1. Introduction.....</b>	<b>1</b>
1.1. Motivation.....	1
1.2. Objectives.....	4
1.3. Thesis Layout.....	4
1.4. Scientific Contribution.....	6
<b>Chapter 2. Background.....</b>	<b>9</b>
2.1. Dielectric elastomer actuators.....	9
2.2. DEA fabrication.....	12
2.3. Compression modalities of DEAs.....	12
2.3.1. Negative active compression.....	14
2.3.2. Positive active compression.....	15
2.4. DEA modeling.....	15
2.5. Potential applications of DEA as compressive devices.....	16
2.6. DEA electrical safety.....	17
<b>Chapter 3. Designing Active Compression Bandages Using DEAs.....</b>	<b>19</b>
3.1. Abstract.....	20
3.2. Introduction.....	20
3.3. Design.....	22
3.3.1. Pragmatic considerations.....	22
3.3.2. Analytical modeling.....	24
3.4. Methods and materials.....	26
3.4.1. Test set-up and calf prototype.....	26
3.4.2. Fabrication of the ACB.....	28
3.4.3. Mechanical testing.....	30
3.4.4. Finite element modeling.....	31
3.5. Results and discussion.....	33
3.5.1. Passive compression stocking pressure range.....	33
3.5.2. Active compression stocking.....	35
3.6. Limitations.....	41
3.7. Conclusion.....	42

<b>Chapter 4. Investigating the performance of DEA-based compression bandages on the flexible human calf.....</b>	<b>43</b>
4.1. Abstract.....	44
4.2. Introduction.....	45
4.3. Mechanical properties of the calf .....	46
4.4. Analytical modeling of the DEA on a simulated human calf .....	49
4.5. FEM analysis.....	51
4.6. Results and discussion.....	56
4.7. Limitations .....	62
4.8. Conclusion.....	64
<b>Chapter 5. Investigation on a soft Grasping Gripper Based on Dielectric Elastomer Actuators .....</b>	<b>66</b>
5.1. Abstract.....	66
5.2. Introduction.....	66
5.3. Materials and methods .....	67
5.3.1. Soft gripper prototype .....	67
5.3.2. Experimental set-up 1: Actuator Deformation Measurement set-up .....	71
5.3.3. Experimental set-up 2: Pickup force measurement set-up .....	72
5.4. Mathematical analysis .....	74
5.5. Results and Discussion .....	81
5.6. Conclusion.....	89
5.7. Limitations .....	90
<b>Chapter 6. Electrical Safety of DEAs in Proximity to the Human Body .....</b>	<b>91</b>
6.1. Abstract.....	91
6.2. Introduction.....	92
6.3. Safety standards.....	92
6.4. Electrical model for a DEA and human body.....	94
6.5. Hazardous scenarios.....	95
6.5.1. First scenario - High voltage power supply is touched .....	95
6.5.2. Second scenario - The charged DEA is touched.....	95
6.5.3. Third scenario – A charged DEA while attached to a power source is touched	99
Power source voltage output across the DEA stays equal or above the charged DEA voltage before the touch .....	99
Power source voltage output across the DEA drops below the charged DEA voltage before the touch.....	100
6.6. DEA geometrical parameter design .....	103
6.6.1. Planar DEA.....	103
6.6.2. Cylindrical DEA.....	104
6.7. Experimental Verification .....	108
6.7.1. Experimental procedure.....	110
6.7.2. Model verification.....	111
6.8. Case study - DEA active compression bandage .....	115

6.9. Conclusion.....	117
<b>Chapter 7. Conclusion .....</b>	<b>119</b>
<b>References.....</b>	<b>123</b>
<b>Appendix.       Nonlinear Control and Simulation of a Dielectric Elastomer                   Actuator-based Compression Bandage on Flexible Human Calf.....</b>	<b>135</b>
Abstract.....	135
Introduction .....	136
Analytical Modeling .....	136
Human calf .....	137
Silicon DEA bandage .....	139
Mechanical component. ....	139
Electrical component.....	139
Electromechanical component. ....	140
Controller Design .....	141
Simulations and Results.....	143
Conclusion .....	145
References.....	146

## List of Tables

Table 2-1.	Comparison of various actuator technologies. Reproduced with permission [15].....	10
Table 3-1.	Dimensions of DEA samples made for ankle, mid-calf and knee regions. ....	28
Table 4-1.	Constant parameters of the calf compliance relation expressed in Eq. 1. ....	49
Table 4-2.	Initial ACB lengths in centimeter.....	57
Table 6-1.	Geometrical properties of experimental DEA samples.....	111
Table 6-2.	Experimental and analytical capacitances for DEA Sample 1.....	112
Table 6-3.	Experimental and analytical capacitances for DEA Sample 2.....	112
Table 6-4.	Circuit parameters of experimental DEAs.....	113

## List of Figures

Figure 2-1.	Schematic of the working principle of a DEA. Reproduced with permission [15].	11
Figure 2-2.	Examples of different modes of DEA compressive force to an underlying object.	14
Figure 3-1.	A schematic of the ACB placed on the human calf	23
Figure 3-2.	ACB total pressure on a limb with different circumferences for elastomer with a thickness of 1.34 mm and different initial lengths $L_0$ . Dashed lines show ACB total pressure for activation with 11.3kV for the corresponding initial length.	26
Figure 3-3.	The calf prototype (CP): (a) dimensions in mm; discs have the same thickness; (b) structure of the CP; (c) CP with the skin on it.	27
Figure 3-4.	The DEA bandage: (a) fabricated sample in a mold; (b) a finalized sample after attaching the protective fabric and Velcro.	30
Figure 3-5.	Engineering strain-stress curve for the DEA bandage	31
Figure 3-6.	ACB meshed model and deformed geometry in ANSYS analysis.	32
Figure 3-7.	(a) Test setup to measure compression values of a commercial compression stocking; (b) compression values obtained for different sections.	34
Figure 3-8.	ACBs that are wrapped around the ankle and knee chambers	35
Figure 3-9.	Mechanical pressure ( $P_m$ ) vs. the stretch ratio in ACB samples prepared for different calf regions, calculated by FEM and analytical model.	37
Figure 3-10.	Actuation pressure ( $P_a$ ) vs. applied electric field obtained for ACBs at different calf regions.	38
Figure 3-11.	Total pressure ( $P_t$ ) vs. applied electric field obtained for ACBs at different calf regions. Dashed lines correspond to pressures that are applied by the commercial compression stocking.	39
Figure 3-12.	Effects of stacking multiple-layer DEA samples for the knee section on the (a) actuation pressure at different electric fields, and on (b) mechanical pressure for different stretch ratios. The thickness of each layer was kept unchanged at 1.34 mm.	40
Figure 3-13.	Effects of stacking multiple-layer DEA samples for knee section on the actuation pressure at different electric fields. The total thickness of the multilayer DEA was kept unchanged at 1.34 mm.	41
Figure 4-1.	Human calf. a Conical geometry of the calf and its six different regions. Each region is assumed to be 35 mm apart in height [117]. b Fitted curves to calf compliance data obtained from [117] the calf's different regions.	48
Figure 4-2.	Changes of the ACB radius on the compressible human calf.	51
Figure 4-3.	Flowchart of the analytical modeling of the ACB on the flexible calf.	53
Figure 4-4.	Geometry of the calf and ACB in FEM simulations	53
Figure 4-5.	Deformation plots showing the position of the ACB and the calf region at the end of each FEM load step. (a) ACB is radially stretched to the maximum radius of the calf region; (b) ACB is positioned at the top of the	

	calf region; (c) ACB is released to make contact with the calf region. The deformation plot of the electrically actuated ACB is similar to the plot (c) since the deformations are not considerable upon actuation. At each load step, wireframe lines show the geometries before deformation starts and solid shapes show the deformed geometries.....	55
Figure 4-6.	Analytical (solid lines) and FEM (circle markers) results for volume variations in various regions of the calf and different stretch ratios. ....	57
Figure 4-7.	Relative change in the calf volume after wrapping and actuating the ACB. Each color represents a stretch ratio. The secondary axis on the right-hand side shows the calf region's initial volume indicated by the solid line with circle markers. ....	58
Figure 4-8.	FEM (circle markers) and analytical (solid lines) results of the total pressure for regions 1 and 6.....	59
Figure 4-9.	The ACB total pressure in all calf regions for different stretch ratios.....	59
Figure 4-10.	Percentage of change in the ACB total pressure between the two cases of VC and NVC.....	60
Figure 4-11.	Difference between actual and expected values in mechanical pressure as a result of calf compressibility.....	60
Figure 4-12.	ACB actuation pressure for different calf regions.....	61
Figure 5-1.	Soft gripper with cylindrical DEA. (a) A cross-sectional view of the soft gripper and (b) view from the bottom.....	68
Figure 5-2.	CAD drawing of the two-piece chamber of the gripper.....	70
Figure 5-3.	Set-up to characterize the DEA deformation in the proposed gripper. ....	72
Figure 5-4.	Test set-up for force measurements.....	73
Figure 5-5.	Side view of the membrane at a chamber's window. (a) Membrane at relaxed state; (b) membrane at pre-stretch state; (c) membrane at pressurized and/or actuated state. ....	75
Figure 5-6.	DEA deformation profile at a single window of the gripper for an initial chamber pressure of $P=6\text{kPa}$ . ....	77
Figure 5-7.	Pressure-volume profile of the gripper's chamber and air.....	78
Figure 5-8.	DEA membrane and object contact at a single window of the gripper. ...	80
Figure 5-9.	Simulation results of the gripper's grasping force to an object of diameter 3.2cm with $V_c=1\text{L}$ and $P_0=6\text{kPa}$ . ....	80
Figure 5-10.	Sample data acquired from set-up 1.....	82
Figure 5-11.	DEA actuation deformation at the apex for various applied voltages and chamber volumes of a) $V_{c1}=0.6\text{L}$ , and b) $V_{c2}=1\text{L}$ . ....	84
Figure 5-12.	DEA actuation deformation at the apex for various electric fields and chamber volumes of a) $V_{c1}=0.6\text{L}$ , and b) $V_{c2}=1\text{L}$ . ....	86
Figure 5-13.	Sample experimental data on the small (3.3cm diameter) object from test set-up 2.....	87
Figure 5-14.	Gripper's grasping force for different object sizes. a) Grasping force versus the applied voltage. b) Grasping force versus the applied electric field. ....	88
Figure 6-1.	The UL and IEC standard curves for safe limits of amplitude versus current durations. The regions below the curves are safe. Reproduced with permission [79]. ....	93

Figure 6-2.	DEA circuit when it is in contact with the human body. ....	94
Figure 6-3.	Discharge circuit in the 2nd scenario. ....	96
Figure 6-4.	Simulated current-duration curves of DEA discharge circuit for the second scenario using the calculated critical capacitance given by equation (7). $V_0$ is 10kV for the bundle of curves with blue tone and 1kV for the bundle with red tone. The solid lines are the current response using the critical capacitance for $R=R_L + R_{ESR} = 10k\Omega$ . The dashed lines correspond to a similar capacitance as the solid lines but with a different resistance load. The critical capacitance is $0.258\mu F$ for the blue curves and $37.1\mu F$ for the red curves. ....	98
Figure 6-5.	DEA critical capacitance for different initial voltages and resistance loads based on the second scenario. ....	99
Figure 6-6.	Current-duration simulations of DEA discharge circuit for the second and third scenarios in logarithmic scale. Discharge curves are simulated using calculated critical capacitances for a given $V_0$ and $R=R_L + R_{ESR} = 10k\Omega$ . $V_0$ is 10kV for the upper curves and 1kV for the lower curves. ....	101
Figure 6-7.	DEA critical capacitance for different initial voltages and resistance loads based on the third scenario. ....	102
Figure 6-8.	Relaxed and stretched planar DEA. ....	103
Figure 6-9.	Initial area to thickness ratio for a safe planar DEA capacitor. The area under these curves represents the safe region. ....	104
Figure 6-10.	Cross-section of a cylindrical DEA relaxed and under stretch. a and b are the inner and outer radii of the stretched and actuated DEA while A and B are the similar values when relaxed. ....	105
Figure 6-11.	The safe values for geometrical parameters of stretched and actuated cylindrical DEA for different dielectric relative permittivity. The area under the curves shows the safe range. ....	106
Figure 6-12.	Stretched and actuated dielectric thickness to inner radii ratio for different lengths of cylindrical DEAs. The regions above the curves are safe. ....	107
Figure 6-13.	Initial thickness to inner radii ratio of a safe cylindrical DEA for different stretch ratios. The safe region is the area above the curves. ....	107
Figure 6-14.	Circuit of the DEA discharge to an equivalent human body load. ....	108
Figure 6-15.	The prototype of the DEA discharge circuit. ....	110
Figure 6-16.	Load voltage while the DEA is discharged. $\lambda$ represents the DEA stretch ratio in the longitudinal direction. ....	111
Figure 6-17.	Load voltages for $\lambda=1$ and 1.1 with their fitted exponential plots. ....	114
Figure 6-18.	DEA discharge current through $500\Omega$ load resistance for four different stretch ratios compared to the UL safety threshold. ....	114
Figure 6-19.	Status of the initial area to thickness ratio for DEA Sample 1 and Sample 2 inside Figure 6-9. Since both samples are under the safety limit curve, they are safe. ....	115
Figure 6-20.	DEA based compression garment. ....	116

## List of Acronyms

ACB	Active Compression Bandage
CP	Calf Prototype
CS	Compression Stocking
DEA	Dielectric Elastomer Actuator
FEM	Finite Element Modeling
IPC	Intermittent Pneumatic Compression
UL	Underwriters Laboratories

# Chapter 1.

## Introduction

In recent years there is a growing number of innovative actuators that are being introduced as alternatives to conventional rigid actuator systems. An interesting group of these novel actuators is artificial muscle actuators which are devices that mimic natural muscles in terms of being able to reversibly undergo expansion, contraction, rotation, or a mix of these motions only using one physical component [1]. Typically, artificial muscle actuators are higher in flexibility, versatility, and power to weight ratio in comparison with rigid actuators [2]. Because of these properties, artificial muscle actuators are considered as a potential disruptive emerging technology which although currently is in limited use, however, might have wide future applications across many industries and science fields [2], [3].

Dielectric elastomer actuators (DEAs) are a prominent type of artificial muscles that are soft, lightweight, energy-efficient, cost-effective and furthermore has the potential to operate as simultaneous actuator, sensor, and generator [2]. Electronically a DEA is considered as a capacitor that consists of at least one soft elastomeric dielectric membrane that is sandwiched between two compliant electrodes. Once actuated with electrical stimuli, a DEA shrinks along the dielectric thickness and expands in a transverse direction. This deformation creates or induces a force that can be used for various applications [4].

This thesis is an endeavor toward studying the potential use of DEAs for real-life practical applications.

### 1.1. Motivation

In many practical applications, devices that can safely interact with delicate items and also work in uncertain, unstructured environments are needed [5]. Examples of such practical applications are abundant in the fields of soft robotics and wearable technologies [6]. Soft actuating systems are a natural choice for such applications due to key features that are not otherwise available in conventional rigid systems. Particularly, soft actuation

systems are capable of going through large deformations and mechanically adapt to comply with different surfaces. Hence, there is a growing effort to investigate and develop soft actuation systems.

One stream of soft actuation systems, DEAs have attracted growing attention mainly due to their unique combination of properties. DEAs possess advantages such as being soft and compliant to surrounding surfaces, large actuation deformations, high efficiency, fast time response, cost-effectiveness (cheap and abundant elastomers and electrode materials), lightweight (density close to water) and ease of fabrication. Besides their ability to undergo large deformations, DEA's relatively high elastic energy density (5 to 40 times that of piezoelectrics), makes them extremely efficient as transducers, as they can store more energy when deformed for the same mass and volume of transducer material. These properties make DEAs one of the most promising technologies in terms of emergent soft actuators.

Many practical applications require soft actuation systems that induce some sort of compressive forces. DEAs can be configured to apply compressive forces in different directions, shapes, and forms. In this thesis, the focus is on configurations and practical applications in which a DEA is generally applying compressive forces to an object that it encompasses. Examples include compressive garments for human limbs, soft graspers, and soft peristaltic pumps. In general, the compressive forces of DEAs includes two components: a passive component resulting from the mechanical stress in the DEA's elastomer; and an active component induced by the voltage-driven actuation of the DEA. It is interesting to design and develop novel and functional actuators based on DEAs for such applications firstly, due to the unique properties that they offer and secondly, considering the limitations of the conventional actuation systems such as rigidity and bulkiness.

DEAs have been studied and proposed for the area of wearable devices [5]. Light, slim, soft, and portable actuation structure of DEAs has enabled new exploration opportunities in the wearable area which was not possible by the limitation of conventional rigid systems. DEAs have been studied as wearable haptic, tactile, and prosthetic devices. One class of the wearables that have profound applications for human health are compression bandages. Compression bandages are typically used to provide compression therapy and improve blood circulation in the human body especially lower

extremities. Applying an effective compression in the lower leg has implications in several disorders related to blood circulation insufficiency. Examples of such disorders include edema, deep vein thrombosis, and orthostatic hypotension. DEAs, while placed around a limb, are able to apply a variable compression and present a potential candidate for active compression bandages. Hence, in this thesis, DEAs as means of compression therapy for the lower human body are investigated.

Soft robotics is another field of study where DEAs has been proposed [5]. Soft robotics is a subfield of robotics which deals with building robots from highly compliant materials and structures, similar to what is typically found in biological systems. Soft robotics is a growing area since there is an increasing number of robots that need to safely interact with delicate and unstructured surroundings and collaborate with humans. Particularly, with the emergence of collaborative robots (cobots), which enables side by side cooperation of a human worker and a robot, the need for robotics systems that are soft and compliant is relevant more than ever. Cobots, are equipped with proper hardware, software, and operation designs to allow safe interaction with humans. To further increase the safety of cobots, soft robotics is considered to reduce the potential incidents arising from harsh, rapid, and dangerous impacts of conventional hard systems yet [7]. Gripping end effectors are one of the essential parts of a majority of cobots, particularly in applications such as pick and place, food manipulation, and part assembly. Thus, gripping systems, which provide intrinsic softness and compliance, could be developed to potentially improve the safety of cobots for such applications. Since DEAs can potentially produce large deformations while inducing little but effective pressure to contact surfaces, their potential use as soft grasping end effectors is investigated in this thesis.

Besides the two underlying applications in this thesis, there are many other applications where DEAs are envisioned to be operated while being near or even in direct contact with the human body. Noting that DEAs are generally activated by high voltages (Typically higher than 1 kV) and can store high voltage charges, the safety of the mentioned DEA-based devices is a huge concern. Therefore, the study of the electrical safety of DEAs in the mentioned applications is of paramount relevance and hence studied in this thesis.

## 1.2. Objectives

The goal of the studies in this Ph.D. thesis is to explore and investigate practical applications of DEAs, particularly, applications that require DEAs to apply compressive forces. The focus of this thesis is to characterize the behavior and performance of DEAs in such practical applications and is not to create novel computation and fabrication methods for DEAs in general. Two potential applications of DEAs are considered, one is compression bandages and the other is soft grasping grippers. Considerations about electrical safety when DEAs are operated in close proximity to the human body are also investigated. The safety considerations are important for both of the above-mentioned applications as direct human contact with DEAs may occur.

4 main objectives are proposed as the required millstones toward the goal of this Ph.D. thesis. objectives 1 to 4 are as follow:

OBJECTIVE 1: Identify the modalities of DEA compressive forces. (In this objective, two compression modalities are introduced.)

OBJECTIVE 2: Use the first modality identified in OBJECTIVE 1 for a practical application (Active compression bandage for the human lower leg)

OBJECTIVE 3: Use the second modality identified in OBJECTIVE 1, for a practical application (Robotic soft grasping gripper)

OBJECTIVE 4: Identify conditions for the electrical safety of DEAs in practical applications that put DEAs close to the human body.

## 1.3. Thesis Layout

The format of this thesis is paper-based (that is, each of the main chapters 3 to 7 is adapted from a published journal paper) and the following chapters of this thesis (chapter 2 and onward) are arranged as follows.

Chapter 2 provides a high-level background on DEAs including materials and methods used for the fabrication of DEAs and general methods used for analytical modeling of DEAs. Besides, chapter 2 presents a complimentary literature review to the introduction sections of chapters 3 to 7. Also, OBJECTIVE 1 is addressed in chapter 2,

section 2.3. Different configurations and modes of compression application by DEAs are discussed. Two compression modalities, namely negative and positive active pressure, are introduced for further investigation in this thesis. In chapter 2, the literature is also reviewed to provide background insights on two chosen applications namely active compression bandages and soft grasping grippers. Finally, this chapter provides a literature review regarding the electrical safety of DEAs in applications where close interaction of a DEA with the human body is anticipated.

OBJECTIVE 2 is addressed in chapters 3 and 4. Chapters 3 and 4 present the achievements toward OBJECTIVE 2 by investigating the application of negative active pressure modality for DEA-based active compression bandage (ACB) for the human lower leg. The ACB is designed to apply a passive compression around the lower leg which is reduced upon actuation of the DEA. Specifically, Chapter 3 addresses investigation on the ACB by characterizing its performance through mathematical simulations and experiments. DEA-based bandages are prototyped and tested on a custom-made human leg mock-up, the mock-up simulating general geometrical dimensions of the average human lower leg. Analytical and Finite Element models which are validated by experimental data are developed to build the basis for further investigation of the proposed ACB in Chapter 4.

Chapter 4 presents an analysis considering the interaction of the ACB with the flexible and compliant human lower leg. The verified mathematical models that are developed in Chapter 3, are further incorporated with developed human leg compliance models, to further simulate and study the performance of the DEA-based compression bandages in the application of variable compression on the human lower leg.

Chapter 5 presents the achievements toward OBJECTIVE 3 which describes an investigation on a soft grasping gripper using the positive active pressure modality. The gripper is designed to apply compression on a target object which is increased by activation of the DEA. A prototype of the gripper is manufactured, and the device is characterized using analytical and experimental analysis.

Chapter 6 presents the achievements toward OBJECTIVE 4 which studies the electrical safety of DEAs in proximity to the human body. Electrical safety standards based

on IEC and UL standards are considered to draw consideration for designing DEAs, particularly in planar and cylindrical configurations.

Chapter 7 concludes the study of the Ph.D. thesis with a discussion of future work.

References throughout the thesis are consolidated at the end of the thesis in 0.

Appendix A presents a preliminary work toward a future improving aspect of OBJECTIVE 2. Analytical models are adapted from chapters 3 and 4 to design and simulate a nonlinear controller based on the input-output linearization control strategy.

## 1.4. Scientific Contribution

In this thesis, DEA-based devices are proposed for use in real-life applications. The research builds peer-reviewed scientific literature that could provide researchers with insights on the design and development of future DEA-based devices and furthermore presents related mathematical and experimental analysis.

The performed research on the electrical safety of DEAs is focused to address one of the biggest challenges and limitations of the DEA devices and is expected to have a considerable impact. It is hoped that the community of researchers who are developing future DEAs-based devices could benefit from the outcomes of this aspect of the research.

Corresponding research for the fulfillment of objectives 2-4 is verified by peer-reviewed journal publication. The research, which exclusively was performed during this Ph.D. thesis, contributed to 4 first-authored individual journal articles, all of which are published and available on the internet. Chapters 3 to 6 of this thesis, each, are adapted from one of these 4 published articles [8]–[12]. The journal publications are as follows:

**Chapter 3:** Pourazadi S, Ahmadi S, Menon C. Towards the development of active compression bandages using dielectric elastomer actuators. *Smart Materials and Structures*. 2014 Apr 16;23(6):065007. Shahram Pourazadi performed the experiments and mathematical modeling and wrote the manuscript.

**Chapter 4:** Pourazadi S, Ahmadi S, Menon C. On the design of a DEA-based device to potentially assist lower leg disorders: an analytical and FEM investigation accounting for nonlinearities of the leg and device deformations. *Biomedical engineering*

online. 2015 Dec;14(1):103. Shahram Pourazadi performed mathematical modeling and wrote the manuscript.

**Chapter 5:** Pourazadi S, Bui HT, Menon C. Investigation on a soft grasping gripper based on dielectric elastomer actuators. Smart Materials and Structures. 2018 Dec 10. Shahram Pourazadi performed the experiments and mathematical modeling and planned and wrote the manuscript.

**Chapter 6:** Pourazadi S, Shagerdmootaab A, Chan H, Moallem M, Menon C. On the electrical safety of dielectric elastomer actuators in proximity to the human body. Smart Materials and Structures. 2017 Oct 3;26(11):115007. Shahram Pourazadi conducted the mathematical and experimental analysis, collaborated to plan and conduct the experiments, and wrote the manuscript.

Further peer-reviewed scientific contributions were developed during the Ph.D. work. The following peer-reviewed conference paper is a marginal improvement based on the work in chapter 4 of this thesis [10]. This paper is not essential toward meeting the objectives of the Ph.D. work, hence is reproduced in the appendix of this document for interested readers:

- Pourazadi S, Moallem M, Menon C. Nonlinear control and simulation of a dielectric elastomer actuator-based compression bandage on flexible human calf. International Conference on Bioinformatics and Biomedical Engineering 2017 Apr 26 (pp. 289-300). Springer, Cham.

The following publications were only marginally related to this thesis work and hence not reproduced in this document:

- Moein H, Schmill U, Komeili M, Pourazadi S, Menon C. Effect of the Leg Volume Change on the Performance of an Active Compression Brace Based on Shape Memory Alloys. Journal of Medical and Biological Engineering. 2017 Apr 1;37(2):248-61.
- Shagerdmootaab A, Pourazadi S, Moallem M, Menon C. Control of a high-voltage bidirectional dc-dc flyback converter for driving DEAs. IET Power Electronics. 2018 Apr 25;11(10):1698-705.

- Shen H, Pourazadi S, Rahimi M, Jiang X, Menon C. A preliminary investigation on a wearable sensory system for lower leg swelling detection. In 2017 8th IEEE Annual Information Technology, Electronics and Mobile Communication Conference (IEMCON) 2017 Oct 3 (pp. 261-265). IEEE.

## Chapter 2.

### Background

Given that the format of this thesis is paper-based, this chapter is planned to be complementary to the literature review of each of the subsequent chapters. This chapter is also aimed at addressing objective 1 of this thesis, “Identify modalities of DEA compressive forces”. To meet this objective, different modalities for applying compression to an enclosed object by DEAs are briefly discussed and two modalities are identified for further investigation in this thesis.

#### 2.1. Dielectric elastomer actuators

Dielectric elastomer actuators (DEAs) are a sub-category of electro-active polymers (EAPs) which consists of at least one layer of an elastic dielectric that is sandwiched between compliant electrodes. There is a growing desire to use DEAs in many applications due to the unique combination of properties that DEAs show. DEAs possesses advantages such as large actuation deformations (>100%), high energy density ( $>3.4 \text{ MJ/m}^3$ ), high efficiency (>80%), fast time response (<1ms), cost-effectiveness (cheap and abundant elastomers and electrode materials), lightweight (close to water) and ease of fabrication [5], [13], [14]. A comparison of various actuation systems is provided in Table 2-1 which shows interesting properties of DEAs relative to other actuation systems such as piezoelectric, shape memory, and electromagnetic devices.

**Table 2-1. Comparison of various actuator technologies. Reproduced with permission [15].**

Type (specific)	Maximum strain	Maximum pressure	Specific elastic energy density	Elastic energy density	Coupling efficiency $k^2$	Maximum efficiency	Specific density	Relative speed (full cycle)
	%	MPa	$J \cdot g^{-1}$	$J \cdot cm^{-3}$	%	%		
Dielectric elastomer (acrylic with prestrain)	380	7.2	3.4	3.4	85	60–80	1	Medium
Dielectric elastomer (silicone with prestrain)	63	3	0.75	0.75	63	90	1	Fast
Dielectric elastomer (silicone – nominal prestrain)	32	1.36	0.22	0.2	54	90	1	Fast
Electrostrictive polymer [P(VDF-TrFE)]	4.3	43	0.49	0.92	–	≈80 (est.)	1.8	Fast
Electrostatic devices (integrated force array)	50	0.03	0.0015	0.0025	50 (est.)	>90	1	Fast
Electromagnetic (voice coil)	50	0.1	0.003	0.025	–	>90	8	Fast
Piezoelectric ceramic (PZT)	0.2	110	0.013	0.1	52	>90	7.7	Fast
Piezoelectric single crystal (PZT-PT)	1.7	131	0.13	1	81	>90	7.7	Fast
Piezoelectric polymer (PVDF)	0.1	4.8	0.0013	0.0024	7	–	1.8	Fast
Shape memory alloy (TiNi)	>5	>200	>15	>100	5	<10	6.5	Slow
Shape memory polymer (polyurethane)	100	4	2	2	–	<10	1	Slow
Thermal (expansion – Al, $dT = 500$ K)	1	78	0.15	0.4	–	<10	2.7	Slow
Conducting polymer (PANI)	10	450	23	23	<1	<5 (est.)	≈1	Slow
Ionic gels (polyelectrolyte)	>40	0.3	0.06	0.06	–	30	≈1	Slow
Magnetostrictive (terfenol-D)	0.2	70	0.0027	0.025	–	60	9	Fast
Natural muscle (human skeletal)	>40	0.35	0.07	0.07	–	>35	1	Medium
Natural muscle (peaks in nature)	100	0.8	0.04	0.04	–	40	–	Slow–fast

Electrically, DEAs are capacitors that are capable of storing high voltage (usually more than 1kV) charges. Once the high voltage is applied to a DEA, the high voltage electric field through the dielectric medium exerts a Maxwell stress tensor to the soft dielectric [16], [17]. As a result of this stress tensor, the dielectric membrane deforms in the thickness and expands in the transverse direction as shown in Figure 2-1. The Maxwell stress along the membrane thickness  $\sigma_M$ , can be expressed as:

$$\sigma_M = \epsilon_0 \epsilon_r \left(\frac{V}{d}\right)^2 \quad (1)$$

where  $\epsilon_0=8.85 \times 10^{-12}$  F/m is the vacuum permittivity,  $\epsilon_r$  is the material's relative dielectric constant,  $V$  is the voltage applied across the DEA membrane, and  $d$  is the thickness of the DEA membrane. multiple layers of electrode sandwiched elastomers could be stacked together to improve the amount of generated Maxwell force.

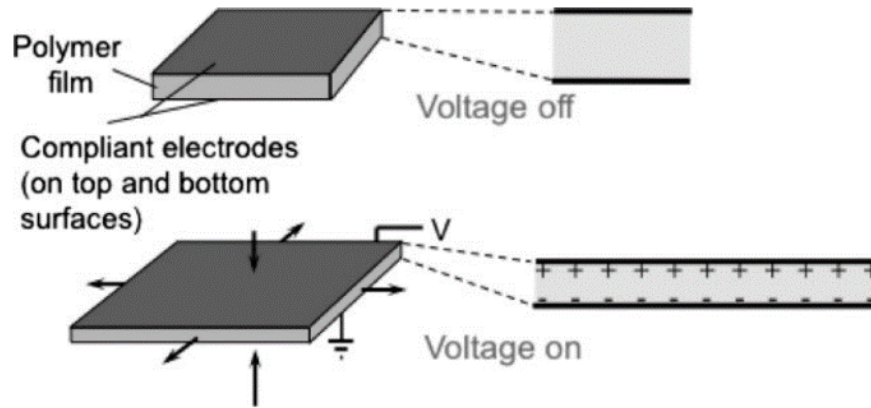


**Figure 2-1. Schematic of the working principle of a DEA. Reproduced with permission [15].**

Typically, the dielectric membrane in a DEA is made of very soft and stretchable Silicone or Acrylic elastomers which show hyperelastic and viscoelastic properties respectively [18]. The viscose element of acrylic elastomers is higher than silicone ones resulting in poorer electromechanical behavior including larger relaxation and steady-state times. Typical acrylic elastomers show very large stress relaxations of up to 500% within a settling time of 30 minutes for stretch ratios of less than 1.5 [19]. However, silicone elastomers could exhibit small stress relaxations of less than 4% within a settling time of 120 minutes for stretch ratios of up to 2 [20]. In general, silicone elastomers show faster electromechanical response and yield better reproducibility in cyclic actuations whereas

acrylic elastomers demonstrate larger actuation strains [21]. The nonlinear behavior in these materials complicates the mathematical expression of DEAs. The modeling of DEAs is discussed in section 2.4 of this chapter.

DEAs are developed and studied in various shapes and configurations. The studied configurations include: planar [22], [23], rolled [24]–[26], cylindrical [27], helical [28], [29], spherical [30], [31] tubular [4], [32] and laminate in unimorph and bimorph forms [33], [34]. The focus of this thesis is to investigate the performance of DEAs in practical applications where DEAs apply some sort of compressive force.

## **2.2. DEA fabrication**

As mentioned in the previous section a DEA consists of 2 parts; a dielectric membrane and compliant electrodes. The dielectric membrane is usually made of highly stretchable polymers, typically silicone or acrylic-based polymers [17], [33], [35], [36]. The dielectric elastomer either or could be acquired from commercial venues like VHB™ family of acrylic tapes from 3M™ or is fabricated using various fabrication techniques. Fabrication techniques for the dielectric layer include casting or moulding [4], [27], [31], spin or spray coating [33], [37], blade casting [38], [39] roll to roll method [40], Aerosol-jet printing [41], and 3D printing [42].

The electrode parts of a DEA are usually made of compliant materials. The most commonly used electrodes are based on carbon particles in forms of carbon powder, carbon grease and carbon powder in rubber matrix [43]–[45]. Silver particles and grease have been used as compliant electrodes as well [46], [47]. A wide range of methods are used to apply the electrodes on the elastomer layer of a DEAs that includes brushing [33], spraying in conjunction with shadow masking [37], [48], stamping [49], ion implantation [50], inkjet printing [45] and pad printing [51].

## **2.3. Compression modalities of DEAs**

DEAs could be used in the design of compressive devices in various ways and configurations. In this thesis, only configurations where a DEA is positioned around an object in generally a cylindrical shape and the DEA applies an inward radial compression

to the object are investigated. Other configurations such as where the DEA applies an outward compression to an object (i.e. the object is outside of the cylinder) or the DEA compression results from the longitudinal pressure along the length of the DEA are not addressed in this thesis.

The pressure applied by a DEA can be classified as passive or active. Passive compression is the pressure applied by the unactuated DEA and is due to the pre-stretch and mechanical stress of the DEA membrane. On the other hand, active compression is the pressure induced by electrically stimulating the DEA. The total compression applied by a DEA is the algebraic summation of the passive and active pressures.

Depending on the target application and design requirements for a DEA, compressive forces can be implemented in different modes. For example, compressive forces can be applied in radial or axial directions, the induced active pressure may be in the same direction than the passive pressure or in the opposite direction, or the active pressure may alter with time in an impact pulse, square pulse, linear, or nonlinear (e.g. sinusoidal) fashion depending on the desired electrical stimulation profile. Moreover, the active regions of the DEA could be continuous (as shown in Figure 2-2(b)) or limited to certain sections of the DEA to allow targeted compression variation on only certain regions of the underlying object (as shown in Figure 2-2(a)).

Considering the direction of the active pressure, a DEA could be actuated in two general modalities: 1- DEA actuation results in a decrease of the total compression (negative active compression); and 2- DEA actuation results in an increase of the total compression (positive active compression). In this thesis, practical applications based on these two compressive modalities and for DEAs that generally apply radial compressive forces are investigated.

In the following sections, each of the two modalities is discussed in more detail.

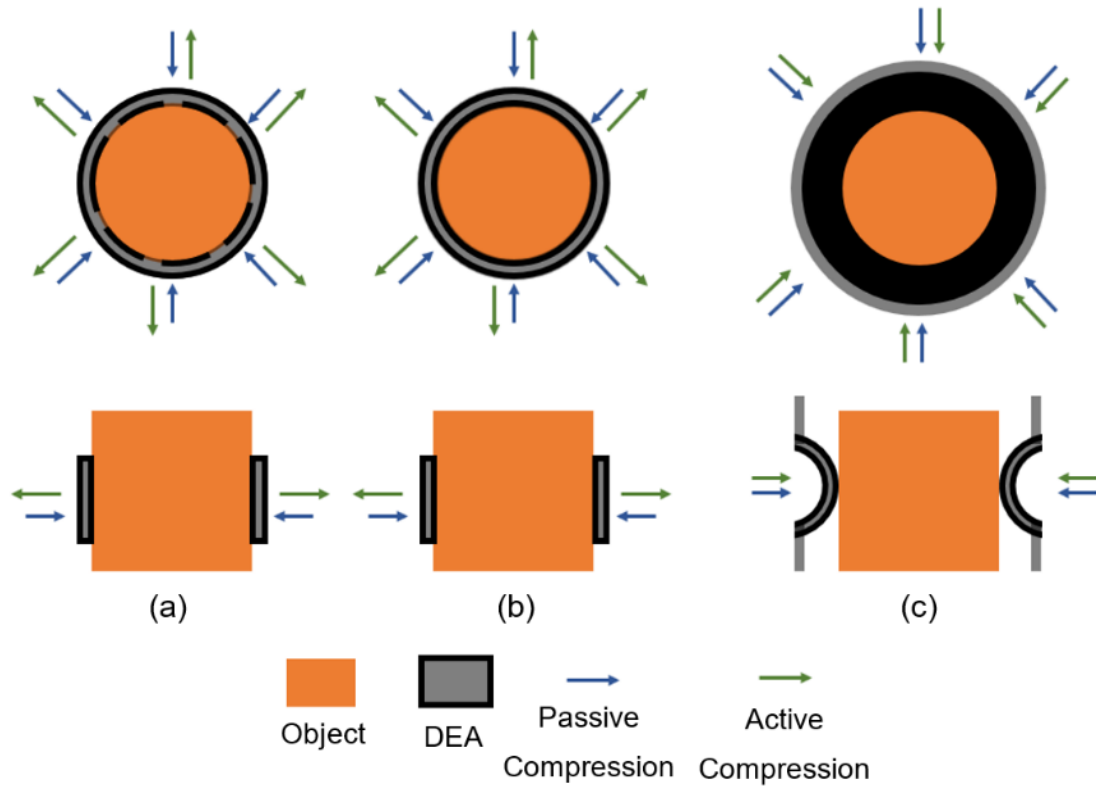


**Figure 2-2. Examples of different modes of DEA compressive force to an underlying object.**

### 2.3.1. Negative active compression

In this mode, the active pressure is directed outwardly and acts against the inward passive pressure as shown in Figure 2-2(b). Assuming a radial compression, the passive pressure is dependent on the hoop stress in the membrane which is subsequently resulted due to the mechanical pre-stretch [27]. Once the DEA is electrically activated, the electric field across the membrane's thickness creates a Maxwell stress tensor [52] which relaxes the radial passive pressure and hence results in reduced total compression [27]. This configuration is advantageous in scenarios where a compression should be applied to an object in default operations and reduced compression pulses are desired from time to time. Examples of such configuration and scenarios are presented in [27], [32]. For example, in [32] a cylindrical DEA, which is placed around a soft tube, is proposed to control fluidic flow in the tube. In default, the DEA applies a passive compression to the tube to limit the fluid flow inside the tube. This compression is then reduced upon activation of the cylindrical DEA, resulting in increased fluid flow.

### **2.3.2. Positive active compression**

In this mode, the active pressure acts in the same direction of the passive pressure as shown in Figure 2-2(c). In Figure 2-2(c), the DEA membrane is inflated, and the passive pressure is created due to the compression of the inflated parts against the object. When the DEA is actuated, the inflated parts undergo further buckling, resulting in increased total compression to the underlying object. This configuration is discussed in more detail in Chapter 5. Unlike the case in section 2.3.1, this configuration is advantageous in scenarios where increased compression pulses are desired from time to time. An example application of this DEA compression modality is proposed in [53] as a DEA-based wearable tactile display wrapped around a fingertip to apply a passive compression which is increased by application of voltage. Another example application is presented in [54] where a DEA is embedded in a wearable brace for the lower leg. The embedded DEA contributes to a passive compression applied by the brace and upon activation of the DEA, the induced compressive force is increased.

In this thesis, these two mentioned modalities have been considered and for two different practical applications. The analytical models and experimental procedures related to the first modality are discussed in Chapter 3 and Chapter 4, and related to the second modality is discussed in Chapter 5.

## **2.4. DEA modeling**

DEA modeling is an important aspect of the design and simulation of DEAs. Throughout this thesis, compressive forces of DEAs for different applications and under different boundary conditions and constraints are modeled. Since DEAs are capacitors that undergo mechanical stress variations within the dielectric medium by application of high voltages, in order to effectively model the behavior of DEAs, the electromechanical coupling of the electrical and mechanical components of a DEA should be considered. The mechanical component of a DEA typically describes stress-strain relationships of a DEA medium while the electrical component describes the electrical dynamics of a DEA's circuitry. To integrate the mechanical and electrical components, equation (1) is used by relating the Maxwell stress in the dielectric medium to the voltage across the dielectric membrane.

Both analytical and finite element modeling (FEM) of DEAs, particularly DEA that apply radial compressive forces, are developed for several boundary conditions in literature [4], [27], [44]. Carpi *et al.* and Ahmadi *et al.* constrained DEAs in the axial direction and derive models for the strain and stress in the radial direction [4], [27]. Whereas, Carpi *et al.* considered free boundary conditions on the ends of the DEA in an earlier study [44] and derived expressions along the axial and radial directions.

As mentioned earlier, DEAs are typically made from silicone or acrylic elastomers which are extremely stretchable. Hence, nonlinear solid mechanics is required to represent the behavior of these rubber-like materials. Nonlinear stress-strain relations are usually used in the mechanical component of a DEA modeling to incorporate the nonlinear performance of these elastomers. There are many articles in the literature that study the nonlinear properties and performances of silicone and acrylic-based DEAs [55]–[57].

## **2.5. Potential applications of DEA as compressive devices**

DEAs in general, are being studied for various novel applications in different sectors such as robotics, medical, optics, aerospace, and entertainment [18], [19], [58]–[61]. DEAs are a good candidate for applications that require compressive elements due to their ability in providing uniform radial or axial passive and active compression [4], [27], [32], [59].

In this thesis, DEAs are explored as compressive elements for two potential applications based on the two compression modalities introduced in the previous section. The first application, which is based on the negative active compression modality, introduces DEA as an active compression bandage to enhance blood circulation for the lower leg. Insufficiency in blood circulation in the lower leg can develop serious disorders such as orthostatic intolerance, edema, deep vein thrombosis and varicose veins [62]. One of the methods to improve blood circulation is by applying effective external mechanical compression on human lower extremities [63]–[65]. The current commonly used compression devices have some limitations that negatively influence their treatment efficacy. Specifically, medical stockings are not beneficial in passive orthostasis [66], and pneumatic sleeves cannot be used during ambulatory situations [67]. Hence, the development of novel portable compression devices that are able to exert efficient and

controlled compression is deemed necessary. In this thesis, cylindrical DEAs are investigated as a potential novel compression modality that is portable, lightweight and efficient. The proposed cylindrical DEA applies a passive compression when it is wrapped around the lower leg and reduces the compression when it is actuated with high voltage.

The second potential application, which is based on positive active compression modality, explores object grasping by cylindrical DEAs. Recently there is a growing number of researches that focus on developing soft grippers that can handle delicate objects. Tendency is toward grippers with simplified structures and components that are often designed using compliant surfaces[68]. Gripping mechanisms that use compliant surfaces include pneumatic channels embedded in elastomer fingers [69], [70] , hydrostatic skeletons [71], inflatable rubber pockets [72], material jamming [73], [74] and vacuum suction [75]. All of these mechanisms require the gripper to be connected to at least one continuous air pressure line and consume a considerable amount of power per grasp [68]. Thus, it is interesting to develop soft grippers with novel actuation mechanisms that reduce power consumption.

Bending DEAs are proposed for novel soft grippers [39], [76]. However, these designs are able to provide very small forces of less than 2.4mN. Recently an improved bending DEA-based soft gripper has been proposed by Shintake et al. that provides larger grasping forces using electro-adhesion[60]. In this thesis, a different take on DEA-based soft grippers using cylindrical DEAs, that undergo buckling, is explored. The explored design is discussed in more detail in chapter 6.

## **2.6. DEA electrical safety**

In some applications, DEAs are sought to be operated in proximity or in contact with the human body [27], [53], [77], [78]. Since DEAs are actuated with high voltages and are able to store high voltage charges, it is important to consider the electrical safety of their operation for the mentioned applications in case of a high voltage discharge to the human body.

Although DEAs are capacitive devices that run with HV voltages and can store amounts of electrical charges, the HV discharge from DEA devices is not necessarily dangerous. In general, the main concerns with HV discharges are deep skin and tissue

burns and cardiovascular injuries such as ventricular fibrillation [79]. However, these concerns can be avoided by limiting the current and energy level in the HV exposures. The risk level of HV exposures mainly depends on the current intensity-duration and the charge-duration of the current waveform exposed to the body [79], [80]. For capacitive devices, the current-duration characteristics can be directly related to the capacitance of the device and lower capacitances induce less risk [79]. Thus, high voltage discharge from DEAs, as capacitive devices, is not necessarily harmful as their capacitance is generally low and less than 300pF per cm<sup>2</sup> of the DEA surface [23]. Moreover, many scientific works justify the electrical safety of HV discharges through the human body, although they primarily focus on devices that generate HV pulses such as fence energizers, stun guns, cattle prods, and high-frequency generator leak detectors [80]–[83]. These studies showed that HV pulses can be far from life-threatening and introduced safe limits for HV discharges to the human body.

To date, there are few works that address the electrical safety of DEAs by either physical insulation [77], [84] or by briefly suggesting a current limit in DEA circuitry [53], [78]. To the best of the author's knowledge, currently, there is no extensive study that provides a procedure for the design of DEAs such that they are inherently safe, even when in accidental contact with the skin. Therefore, to reduce the potential threats of DEA devices, a conservative design approach considering the worst-case scenario of high voltage discharge to the human body should be considered. This thesis, therefore, addresses this topic by using available electrical safety standards and studies the design of safe DEA-based devices. While DEAs can be manufactured in a large variety of geometries and configurations, this thesis focuses on the most common configurations presented in the literature, namely flat and cylindrical shapes. These shapes are also of primary interest when designing DEA-based wearable soft robotic systems, such as constrictive garments [27].

## Chapter 3.

# Designing Active Compression Bandages Using DEAs

This chapter aims at achieving the objective 2 of the thesis: “using the first modality identified in OBJECTIVE 1, i.e. negative active pressure, for a realistic application”. To meet this objective, the design of DEA-based active compression bandages (ACBs), to enable variable compression around human lower extremities, is considered. This objective comprises two sub-objectives:

2.1. Designing a DEA-based ACB by characterizing its performance through mathematical simulations and experiments; and

2.2. Considering the interaction of the ACB with the flexible and compliant human lower extremity.

This chapter specifically addresses objective 2.1. whereas chapter 4 addresses objective 2.2. In this chapter, the application of DEAs for exerting active compressive forces on a human limb to potentially improve blood circulation in the lower extremity is explored. The literature is reviewed to present the background on the importance of active compression therapy on the human lower leg and then an active compression bandage based on DEAs is proposed as a solution that is aiming at addressing the shortcomings of the current compression therapy modalities. This chapter also discusses the fabrication of DEA-based compression bandages and demonstrates the performance of the bandages through mathematical modeling and experimentation. The contents of this chapter are adapted from the following publication and modified to comply with the format of this thesis:

Pourazadi S, Ahmadi S, Menon C. Towards the development of active compression bandages using dielectric elastomer actuators. *Smart Materials and Structures*. 2014 Apr 16;23(6):065007.

### **3.1. Abstract**

Disorders associated with the lower extremity venous system are common and significantly affect the life quality of a large number of individuals. These disorders include orthostatic hypotension, edema, deep vein thrombosis (DVT) and any other condition related to insufficient venous blood return. The commonly recommended treatment for these disorders is the use of hosiery compression stockings. In this research, an active compression bandage (ACB) based on the technology of dielectric elastomeric actuators (DEA) was designed, prototyped, and tested. A customized calf prototype (CP) was developed to measure the pressure applied by the ACB. Experimental results performed with the CP showed that the pressure applied by the ACB could electrically be controlled to be either below or above the pressure exerted by commercially available compression stockings. An analytical model was used to provide the design criteria. A finite element model (FEM) was also developed to simulate the electromechanical behavior of the DEA. Comparison of the experimental results with the FEM and analytical models showed that the modeling could accurately predict the behavior of the ACB. The FEM was subsequently used to study how to improve the ACB performance by varying geometrical parameters such as the ACB thickness.

### **3.2. Introduction**

Typically, the blood pressure in lower extremities is higher comparing to other parts of the body due to the hydrostatic pressure resulted from gravitational or other sources of acceleration. Thus, the blood flow in these areas is low and it is harder for the blood to return back to the heart. In general, while standing, blood tends to accumulate in the legs due to venous pooling and capillary filtration [85]. The mechanisms in the lower extremity such as veins valves operation and muscle contraction help the blood to return. Sometimes these mechanisms do not operate properly and result in a decrease in blood flow and an increase in blood volume. Therefore, the amount of blood accumulated in the legs increases and the amount of blood driven to other parts of the body reduces. This venous pooling and reduction in blood flow can cause hypotension, blood clots, edema, and varicose veins. Each of these disorders has its own stream of significance, method of diagnosis and treatment [62]. In order to compensate for venous pooling, an effective

external compression should be applied to lower extremities [63]. In this way, blood pressure and flow are enhanced and blood could return to heart readily.

Compression stockings are one of the existing compression garments which are widely used in this regard. They offer graded compression to the lower extremities with the highest compression at the ankle. This compression reduces venous hypertension and helps the calf muscle pump causing the reduction of edema, improvement of microcirculation, and prevention of skin breakdown [86], [87]. The efficacy of compression stockings for different disorders has been studied in the literature [66], [88]–[90]. Although these garments have shown promising improvements, in many cases their efficacy is questionable and has been challenged [66], [89]. A specific disadvantage of compression stockings is that their compliance should be customized for every single user in order to maximize their efficiency [66], [90]. In addition, stockings are not suitable to provide variable (time-dependent) compression, which was shown in different studies to be more efficient than a static compression [91], [92]. For clinical use, variable compression of lower extremities is implemented by using intermittent pneumatic compression (IPC) systems [93]. IPC consists of several cuffs which are normally wrapped around leg using Velcro [94]. The cuffs are connected to an electric pump using tubes, which are inflated with air. IPC helps reducing venostasis and improves venous return by simulating normal leg muscle activity [93]. IPC can be used for a range of limb geometries and sizes while the compression is regulated by the pump and therefore addresses the shortcomings of compression stockings [95]. However, the presence of a pump and the sizable pneumatic cuffs make the IPC bulky and unsuitable for ambulatory use.

Because of these problems in these common mechanical devices, the need for smart emerging technologies is evident. The desired technology should be able to provide better compliance for the patients and help to alter the amount of compression based upon the need of the body and also apply different ranges of compression for a wide group of individuals with different leg dimensions and hemodynamic characteristics. This device should also actuate quickly in response to signals received from the sensors monitoring hemodynamics of the body. Also, unlike IPC, it should be portable and suitable for ambulatory use to be worn during activities of daily living.

In this chapter, a preliminary investigation on a novel technological approach based on silicone DEAs is explored. A silicone type elastomer has been used in this

chapter due to its better electromechanical stability compared with acrylic type elastomers. In order to utilize the DEA technology in a biomedical bandage, particular design criteria should be considered. A preliminary design has been investigated to point out the considerations that should be taken into account when designing such a bandage. This bandage is able to actively change its exerting compression thus it is referred to as *active compression bandage (ACB)* hereafter. As previously mentioned, the role of the bandage is to potentially eliminate and/or prevent venous pooling disorders corresponding to lower extremities in the human body. To limit the scope of this preliminary investigation, this work focused on the design of ACB prototypes for the calf.

This thesis chapter is organized as follows. In section 3.3, key parameters that should be taken into account for designing the ACB are discussed. In section 3.4, the experimental set-up and materials used in this study are explained and characterized. Also, the FEM procedure for numerical modeling of the experiments is described. In section 3.5, the experimental and simulation outcomes of the conventional and proposed bandage are reported and discussed in detail. Conclusions are drawn at the end of the chapter.

### **3.3. Design**

#### **3.3.1. Pragmatic considerations**

The role of ACB is to actively apply and alter the compression on the calf. When the bandage is wrapped around the calf, it exerts an initial mechanical compression. Once the bandage is activated by electrical voltage, the bandage reduces its thickness, resulting in a reduction of the circumferential compression around the calf. A schematic of the ACB on a human calf is shown in Figure 3-1. In order to design an efficient active bandage, two main parameters should be identified: the amount of circumferential pressure applied to the calf and the geometrical dimensions of the calf. In humans, the calf size varies with each individual. The calf size also changes with the individual undergoing different postures. Generally, standing upright yields greater calf dimensions due to the accumulation of blood in the lower extremities [96]. The required amount of external pressure on the calf varies depending on the severity of the previously mentioned disorders. Typically compression stockings are designed to apply compressions in the range of 15 to 50 mmHg [66], [87].



**Figure 3-1. A schematic of the ACB placed on the human calf**

While cylindrical/conical DEAs can be fabricated [4], [27], the ACB prototype is designed as a bandage rather than a seamless stocking in order to cover a wider range of compressions for different calf circumferences. In fact, one primary asset of utilizing flexible active bandages is that the bandage can provide a controllable pressure on calves with different sizes. Hence, the proposed bandage is a flat DEA that can be wrapped around the calf. This design could potentially bring different advantages including: (1) the ACB can be taken on and off easily; (2) the ACB could be worn to fit different calf sizes; (3) the compression magnitude can be tuned by the amount of initial pre-stretch of the bandage; and (4) the bandage can be provided into small size modules which can be wrapped around different segments of the leg. Each module could be controlled separately, hence providing several degrees of freedom on modes of the external compression. The bandages could be tuned to apply a gradient or constant pressure along the length of the leg. Also, the activation of the DEAs could provide a mode of compression similar to a linear peristaltic pump [4]. In the case of an actuator failure, it could be substituted with another module without the need for changing the entire system.

In this work, Velcro was used to connect the two edges of the flat DEA and obtain a conical shape (see Figure 3-1). However, different solutions should be investigated in a

potentially finalized device to make the ACB aesthetically appropriate to be worn by individuals with disorders associated with their lower extremity venous system.

### 3.3.2. Analytical modeling

There are two components associated with the pressure exerted by the ACB, namely the mechanical and the actuation pressure. The *mechanical pressure* is the initially applied pressure when the bandage is wrapped and pre-stretched around the leg and no electrical stimulus is provided. The *actuation pressure* is instead the pressure variation resulting from actuating the ACB. The actuation pressure is, therefore, the pressure difference when the ACB is electrically activated and deactivated.

The mechanical pressure is a function of the hoop stress of the bandage, which can be computed using the strain-energy density function,  $W$ . In its general form, the strain-energy density function can be written as [97]:

$$W = f(\lambda) \quad (1)$$

where the stretch ratio  $\lambda$  is defined as:

$$\lambda = \frac{2\pi r}{L_0} \quad (2)$$

and where  $L_0$  is the initial length of the flat DEA and  $r$  is the radius of the DEA when wrapped and stretched around the leg. Ogden model is a hyperelastic model that can be used to study the nonlinear behavior of elastomers. The strain-energy density function for the Ogden model can be defined as [98]:

$$W = \sum_{i=1}^N \frac{\mu_i}{\alpha_i} (\sum_j \lambda_j^{\alpha_i} - 3) \quad (3)$$

where  $\mu_i$  and  $\alpha_i$  are Ogden parameters,  $N$  is the order of the Ogden model and  $\lambda_j$  is the stretch ratio in the  $j$  principal direction. By using a second-order Ogden model and by considering a cylindrical geometry of the DEA, (1)-(3) can be used to compute the mechanical pressure as proposed by Ahmadi et al. [27] as follows:

$$P_m = \int_{\lambda_b}^{\lambda_a} - \frac{\mu_1(\lambda^{\alpha_1} - \lambda^{-\alpha_1}) + \mu_2(\lambda^{\alpha_2} - \lambda^{-\alpha_2})}{\lambda(\lambda^2 - 1)} d\lambda \quad (4)$$

where  $\lambda_a$  and  $\lambda_b$  are the stretch ratios respectively for the inner and outer radii of the elastomer, and  $\mu_1, \mu_2, \alpha_1,$  and  $\alpha_2$  are the parameters for the second-order Ogden model.

On the other hand, the actuation pressure is generated by the radial component of the Maxwell stress tensor,  $\sigma_r$  [26]:

$$\sigma_r = \frac{\varepsilon_0 \varepsilon_r E^2}{2} \quad (5)$$

where,  $\varepsilon_0$  is the vacuum permittivity,  $\varepsilon_r$  is the relative permittivity and  $E$  is the applied electric field through the dielectric. The actuation pressure as a function of the applied voltage ( $V$ ) can be derived from (5) as proposed in [27]:

$$P_a = \frac{\varepsilon_0 \varepsilon_r V^2}{2 \ln^2(b/a)} \frac{b^2 - a^2}{a^2 b^2} \quad (6)$$

where  $a$  is the final inner radius and  $b$  is the final outer radius.

The total pressure exerted by the ACB on the calf is determined by subtracting the actuation pressure from the mechanical pressure:

$$P_t = P_m - P_a \quad (7)$$

Equations (4), (6) and (7) show that the total pressure on the leg is a function of the material, stretch ratio and thickness of the elastomer. In addition, it is a function of the circumference of the leg and the voltage applied to the ACB. These three equations can, therefore, be used to select all these design parameters and identify suitable design criteria for the ACB. For instance, Figure 3-2 illustrates the total pressure the ACB applies to the leg for different circumferences of the leg. The pressure range that is displayed in this figure is the same used for mild grade compression stockings [66]. Figure 3-2 enables estimating the initial length of the ACB in case the limb circumference and the desired pressure are known. The degree of approximation of this estimation is discussed in section 3.5 when predictions of this analytical model are compared to the experimental data.

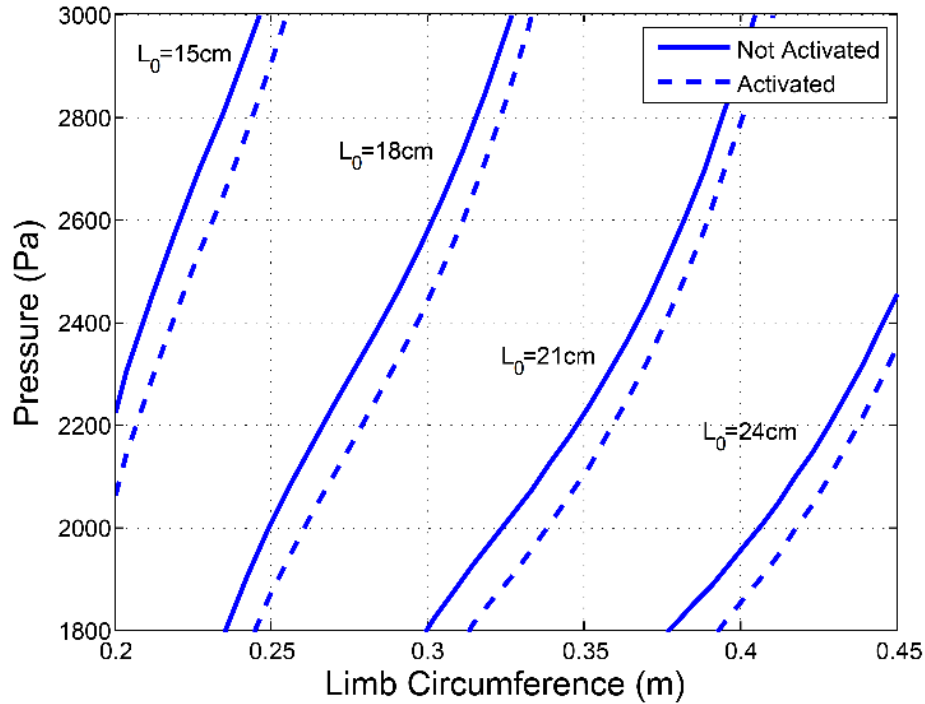


**Figure 3-2.** ACB total pressure on a limb with different circumferences for elastomer with a thickness of 1.34 mm and different initial lengths  $L_0$ . Dashed lines show ACB total pressure for activation with 11.3kV for the corresponding initial length.

### 3.4. Methods and materials

#### 3.4.1. Test set-up and calf prototype

A test set up was designed and developed to monitor and measure the range of pressure exerted by the ACB. This set-up consisted of a customized calf prototype (CP) and a pressure transducer connected to the CP with flexible tubes.

The CP was designed to have three chambers representing ankle, mid-calf and knee areas of the calf. These chambers could be either individually sealed to study a specific region of the calf or could be connected together to study the calf as a whole leg segment. The diameter size for each section of the CP was selected based on the reported average size of the human calf [21, 22]. It was also assumed that the human calf could be approximated to have a conical shape. The dimensions of the CP sections are shown in Figure 3-3(a). The calf segments were made by two disks, supported by two columns, representing tibia and fibula bones. The CP prototype is illustrated in Figure 3-3(b).

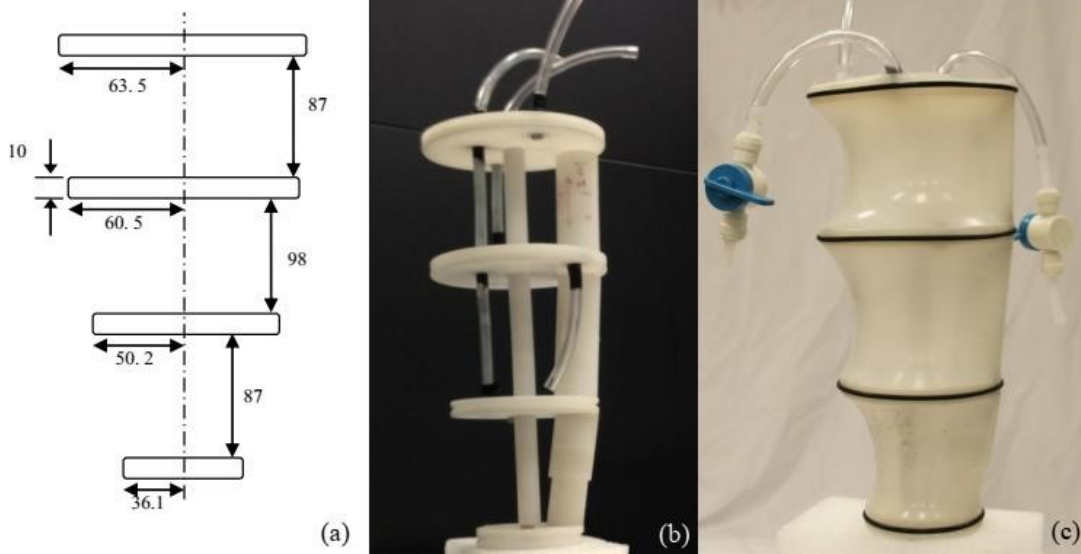


**Figure 3-3. The calf prototype (CP): (a) dimensions in mm; discs have the same thickness; (b) structure of the CP; (c) CP with the skin on it.**

Each chamber was covered by a flexible skin made of silicone elastomer as shown in Figure 3-3(c). The enclosed volume of each chamber enabled having a closed system. The pressure transducer connected to the CP tubing (not shown in Figure 3-3) detected small variations of the pressure exerted by the ACB wrapped around the CP. O-rings and silicone were used to seal the edges of the flexible skin and to make sure that there was no leakage from the chambers. To assure that the chambers were sealed properly, each chamber was examined by applying pressures larger than the one exerted by the commercial compression stockings. Initially, when the chambers were not filled, the skin was bent inward (see Figure 3-3(c)). Each chamber was filled up with a pressure  $P_s$ , which was required to line up the skin with the corresponding adjacent disks and reach the circumference size of the calf region.

The chambers were filled in with fluid and its pressure was monitored with a pressure transducer (Omegadyne PX309-001G5V) connected to the chambers through the tubing. The data from the pressure transducer was acquired using a data acquisition board and a customized LabVIEW program. The measured pressure reported by the pressure sensor was the total pressure of both the ACB and the skin. Thus, in each measurement, the pressure due to the skin itself was measured prior to wrapping the bandage. This pressure was then subtracted from the cumulative measured pressure ( $P_c$ ) in the test results. The CP enabled measuring the two components of the pressure exerted by the ACB, the mechanical ( $P_m$ ) and the actuation pressures ( $P_a$ ).

To actuate the ACB, a custom-made voltage box was used. The box was powered by a 5 VDC battery. The battery voltage was regulated and could be adjusted through the range of 2-5 volts. This adjustable voltage was then amplified with an EMCO Q101 amplifier supplying a range of 2.8-11.3kV at the output of the box. The terminals of the box were connected to copper electrodes embedded in the ACB, as discussed in the following section. The voltage box also had a discharge circuit with the ability to quickly short the two sides of the DEA through a flashlight.

### 3.4.2. Fabrication of the ACB

Different materials can be used for the fabrication of dielectric elastomers [19]. In general, the material should be very flexible and stretchable undergoing large strains and should have a high dielectric constant in order to increase the charges stored on the compliant electrodes. In this work, TC-5005 silicone by BJB [101] was used. The details on the general fabrication procedure of this polymer and the mechanical properties are provided in [27].

In this work, the ACB was designed to exert a compression range similar to the mildest grade of compression stockings which is approximately 15-20 mmHg (2000-2670 Pa) from knee to ankle [102]. It should be noted, however, that the exact amount of pressure exerted by these stockings is a function of the calf circumference. In this work, experiments were done to measure the precise amount of pressure exerted by a commercially available compression stocking (by Sigvaris) on the different segments of the CP. These values of pressure are presented in section 3.5.1. The ACB was designed in order to exert these specific values of pressure when wrapped around the CP. Table 3-1 reports the dimensions of the fabricated ACB. These values were determined by using FEM simulations, as presented in the following section 3.4.4.

**Table 3-1. Dimensions of DEA samples made for ankle, mid-calf and knee regions.**

Region	DEA elastomer length	DEA elastomer width	DEA thickness	Electrode length	Electrode Width	Velcro gap	Equivalent radius
Ankle	180	105	1.34	160	65	5	30.1
Mid-calf	223	125	1.34	210	85	3	36.3
Knee	250	125	1.34	235	85	3	40.6

\*unit is mm for all dimensions.

Molds were manufactured to fabricate a flat DEA. The molds were made from two plates of polyvinyl chloride (PVC) with thin polymethyl methacrylate (PMMA) bars as sidewall boundaries in order to yield the calculated dimensions. Three different samples of bandage were fabricated to fit the three sections of the CP, which are the ankle, mid-calf, and knee sections (see Figure 3-3).

Different materials could be used to fabricate compliant electrodes [45]. In this work, a mixture of carbon black (Vulcan XC-72R) in ethanol with a concentration of 20mg/ml was used, as it was shown to be a suitable low-cost procedure for DEAs [27]. The electrode could be applied to the surface of the TC-5005 in various ways. For example, the electrodes could be brushed or spray-coated on the cured surface of the elastomer. However, we found that electrode particles yield better adhesion to the polymer if the surface of each PVC mold plate was firstly spray-coated with electrode mixture and then polymer mixture was poured into the mold and left to cure. In this way, the polymer layer was diffused into the electrode layer and protected the electrode against detachment and scratches thus enhancing the life of the DEA. A strip of copper tape was also embedded into the polymer layer to easily interface it with the electrode layer during actuation. A piece of meshed cloth was placed around the copper strip to reinforce the copper interface with the polymer matrix as shown in Figure 3-4(a). A stretchable cloth and Velcro tapes were used to cover the ACB samples to avoid electrical contact between the ACB and the CP during testing. A completed ACB sample is shown in Figure 3-4(b).

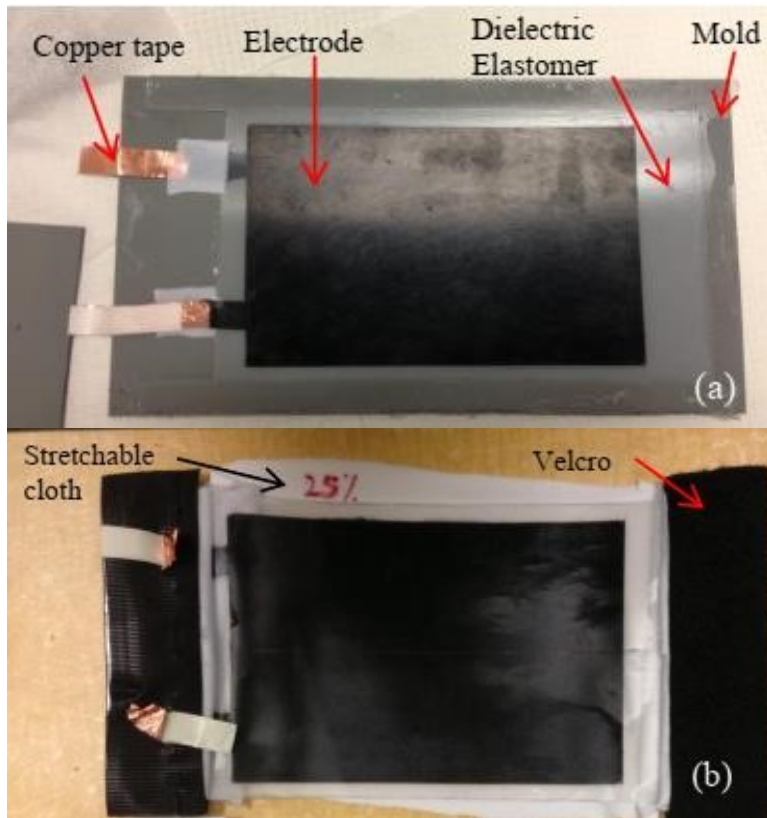


**Figure 3-4.** The DEA bandage: (a) fabricated sample in a mold; (b) a finalized sample after attaching the protective fabric and Velcro.

### 3.4.3. Mechanical testing

A tensile test was performed on the fabricated samples to obtain the mechanical properties of the DEA. Three samples fabricated using 25% of plasticizer were tested. Tests were repeated at least three times. The stress-strain curve for the DEA with 25% of the plasticizer component is shown in Figure 3-5. Ogden parameters used in (4) were obtained by finding the best fit for the stress-strain curve. The best-fitted parameters were as follows:  $\mu_1 = 380.3$  Pa,  $\alpha_1 = 8.972$  ,  $\mu_2 = 40049879.4$  Pa, and  $\alpha_2 = 0.003$  .

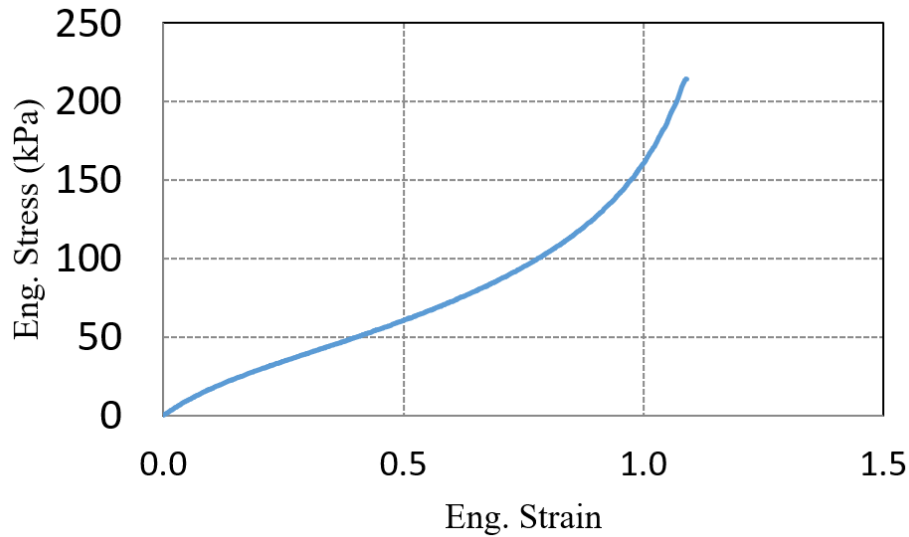


**Figure 3-5. Engineering strain-stress curve for the DEA bandage**

### 3.4.4. Finite element modeling

ANSYS software [103] was used to model the electromechanical behavior of the ACB. Experimentally, two steps were followed to test the ACB samples: (1) the bandage was firstly stretched and tightened by adjusting the Velcro part at its edges to conform to CP and (2) it was electrically activated to a specific voltage to achieve a desired actuation pressure. The same procedure could be modeled by FEM but, to simplify the model, it was assumed that the ACB sample originally had a cylindrical shape that would be reshaped to form the CP configuration. As shown in Figure 3-3, the CP had a shape similar to a truncated-cone with variable radius at different locations and therefore the pressure applied to stretch the sample varied from point to point. The initial radius of the cylindrical model geometry was obtained from knowing the initial length of the ACB (see Table 3-1). This initial length was calculated using an iterative procedure which is explained in the next section.

To reduce the calculation time, only half of the geometry of the ACB sample was modeled as the rotational symmetry exists about the axial direction as shown in Figure 3-6. In this figure, the initial cylindrical geometry is shown in transparent color. We could further reduce the geometry down and model one-quarter of a cylinder based on the rotational symmetry but since the edges of the ACB sample were not covered by electrodes and the Velcro gap adds asymmetrical effects, the minimum geometry to

include all symmetry and boundary effects was a half-cylinder shape. The Velcro gap was the distance that was formed due to the detachment of the bandage from the CP when the Velcro was tightened. The radius of the initial cylindrical geometry considering the Velcro gap was then defined as the equivalent radius.

To mesh the FEM model geometry, a 20-node quadratic ANSYS element (Solid226[103]) was used. This element type can be employed for multi-field simulations including structural, piezoelectric, thermal, electrostatic, and electric field analyses. Here, to study electromechanical effects of the DEA material, electrostatic and structural fields were coupled in a quasi-static analysis case. The change in Cauchy stress by electrical activations was calculated using Maxwell stress tensor built in the Solid226 element. To improve the accuracy of the FEM results in addition to choosing very fine mesh on the inner and outer surfaces of the geometry, the through-thickness direction was split into 12 segments giving reasonable model accuracy and computational time. The total number of elements was  $12 \times 38 \times 100 = 45600$ , and the total computational time to model both stretch and actuation stages was 85min on average by using an Intel Core i7-2670QM 2.2GHz with 8Gb of RAM.

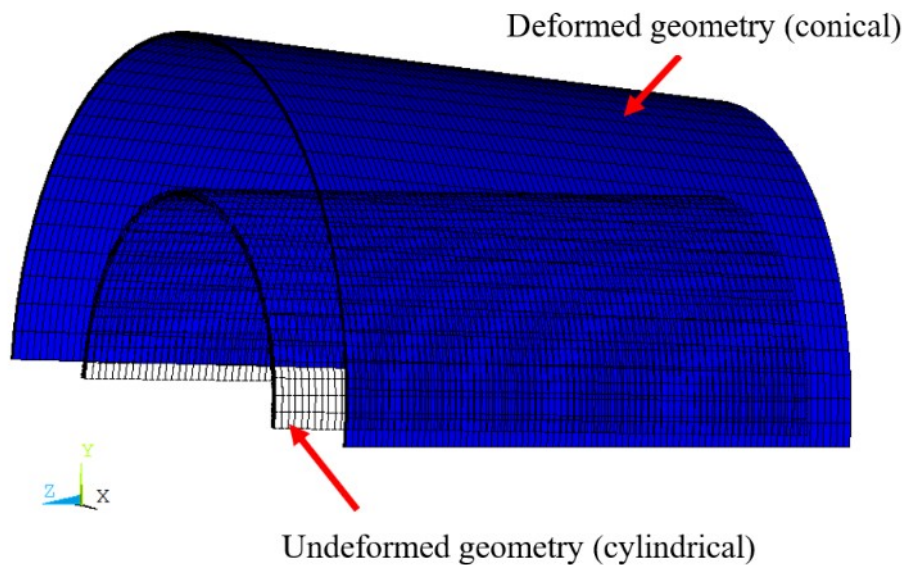


**Figure 3-6. ACB meshed model and deformed geometry in ANSYS analysis.**

The stretch and actuation stages were modeled incrementally and the stretch ratios and the mechanical and actuation pressures at each stage were reported as

outputs. The deformed shape is shown in blue color in Figure 3-6. The reported stretch ratio ( $\lambda$ ) is the changing inner radius of ACB geometry over its initial inner radius. The results are discussed in the next section.

## **3.5. Results and discussion**

### **3.5.1. Passive compression stocking pressure range**

Calf-length compression stockings (Knee-high Graded Support Therapy Socks, Sigvaris Inc, Peachtree City, USA) are designed to apply passive graded pressure of 15-20 mmHg from knee to ankle. Four, same size samples of these stockings were separately put on the CP to measure and verify their compression values. The chambers of CP were filled in with air until they form a conical shape for each segment as shown in Figure 3-7(a). At this stage, the cumulative pressure ( $P_c$ ) in each chamber was measured and recorded. The net pressure exerted by the compression stocking ( $P_n$ ) was obtained by subtracting the pressure required to deform the skin ( $P_s$ , see section 3.4.1) from the cumulative pressure ( $P_c$ ). The net pressures applied by the compression stockings on the ankle, mid-calf and knee sections of the CP were respectively  $20.6 \pm 1$  mmHg,  $16 \pm 0.9$  mmHg, and  $13 \pm 1.2$  mmHg. Figure 3-7(b) summarizes the performed experimental results.

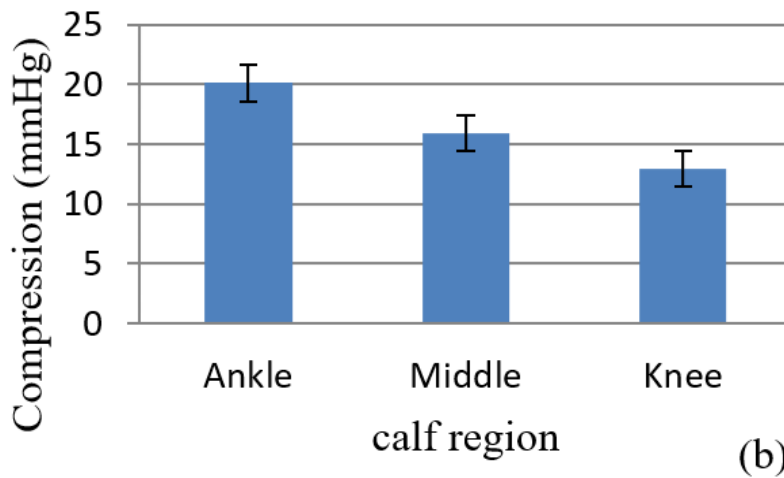
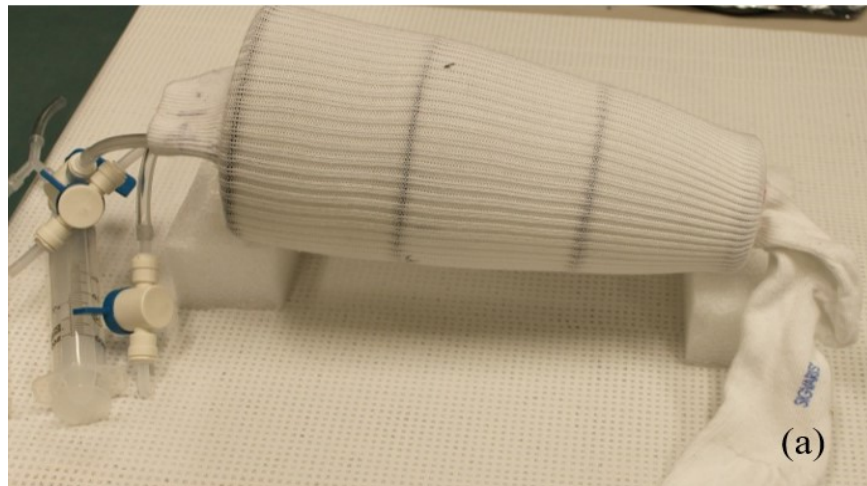
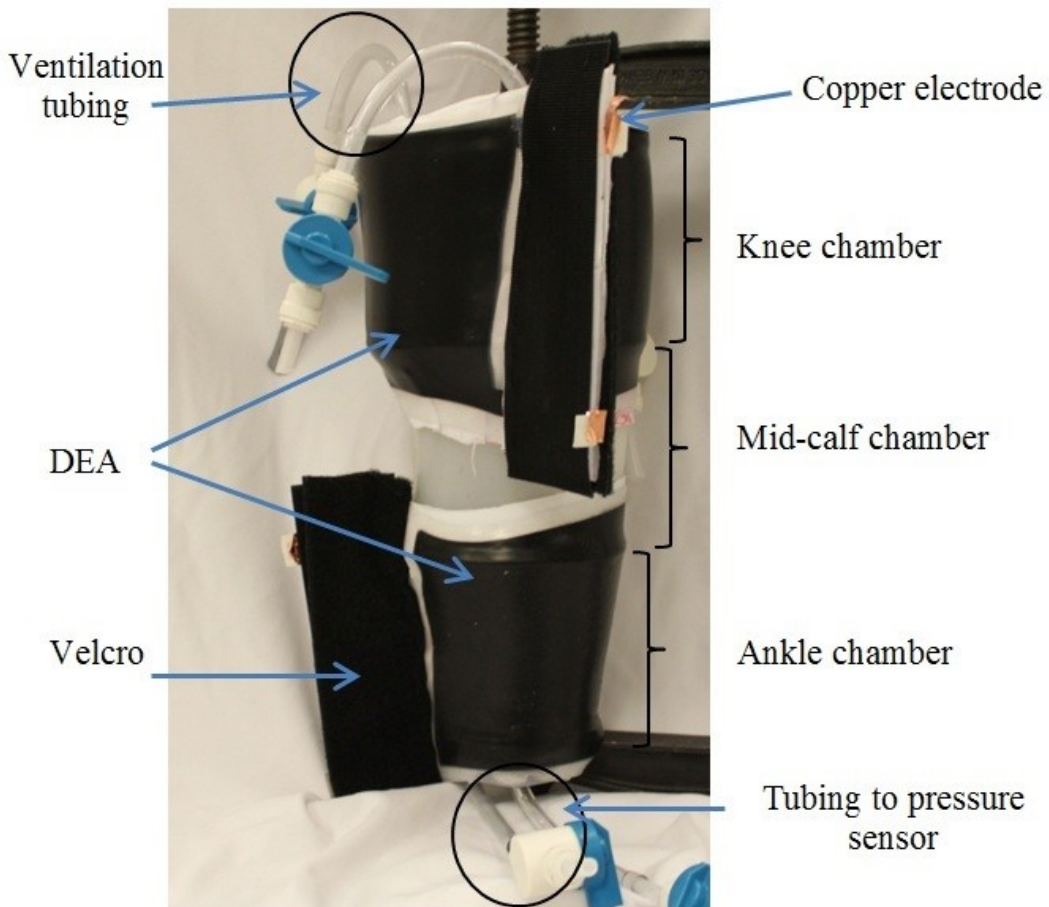


**Figure 3-7. (a) Test setup to measure compression values of a commercial compression stocking; (b) compression values obtained for different sections.**

The experimental measurements show compression values were close to those reported by the manufacturer. However, these data are deviating from those reported by Protheroe *et al.* [66]. The deviation might be due to a variety of reasons including: (1) the compression stockings tested by Protheroe *et al.* might have had a different size; (2) the experiments could have required the stockings to be cut off into small segments to fit the measurement system that was used in that work – cutting the stocking might have altered their performance; and (3) in this study, the measurement device had a conical geometry whereas in the work performed by Protheroe *et al.* the testing system was cylindrical.

### 3.5.2. Active compression stocking

In order to measure the compression exerted by the prepared ACBs, the CP was filled in with deionized water until the shape of its chambers became conical. Deionized water was used to reduce the risk of electrical shock while experimenting with high voltage. The amount of skin compression ( $P_s$ ) on the system was read prior to the wrapping of the bandage. The ACB was wrapped around the chamber as shown in Figure 3-8 and the cumulative pressure ( $P_c$ ) was recorded. As in the case of the measurements with the compression stockings, the mechanical pressure ( $P_m$ ) was obtained by subtracting the skin pressure ( $P_s$ ) from the cumulative pressure ( $P_c$ ). Upon electrical activation, the compression of the bandage was reduced. This drop of pressure was reported as the actuation pressure ( $P_a$ ).



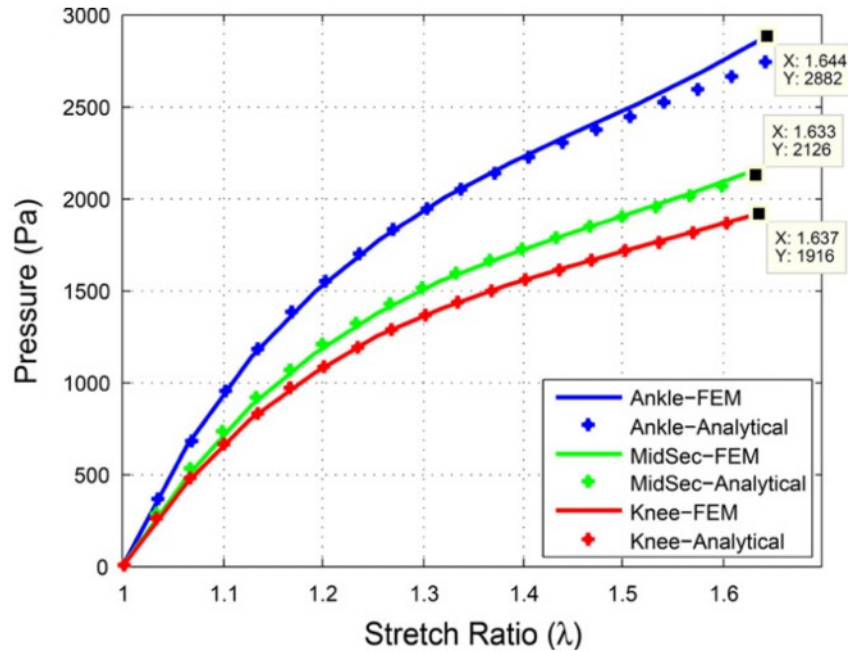
**Figure 3-8. ACBs that are wrapped around the ankle and knee chambers**

Figure 3-9 reports the results obtained by the simulations. This figure graphs the mechanical pressure exerted in different CP sections as a function of the stretch ratio of

the ACB elastomer. Since the CP sections had different circumferences, the same stretch ratios of the ACB corresponded to different mechanical pressures. For instance, a 1.5 stretch ratio in the ACB resulted in 2.48, 2.00 and 1.72 kPa pressures in ankle, mid-calf and knee sections respectively.

For this study, a precise ACB length and stretch ratio had to be selected in order to replicate the mechanical pressures exerted by the compression stockings previously analyzed (see Figure 3-7(b)) on the different CP segments. An iterative FEM procedure was used in order to find such an initial length and stretch ratio. For a defined segment of the CP, the iterative procedure was started by selecting an arbitrary initial length and calculating the final pressure. If such pressure was larger than the pressure exerted by the stockings, a larger ACB length was selected for the next simulation run. On the other hand, if the pressure was smaller, a smaller ACB length was chosen to increase the output pressure. This procedure was continued until the relative error between the FEM and compression stocking pressures became less than 2%. Figure 3-9 shows the final plot in which ACB samples with the finalized initial lengths were stretched with different stretch ratios. The square dots in Figure 3-9 represent the stretch ratios at which the ACB was estimated to reach the circumference of the CP and provide the same pressure exerted by the commercial compression stockings.

ACB samples were manufactured with the initial lengths identified by the FEM simulations – their dimensions are reported in Table 3-1. Experimental tests reported mechanical pressures of  $2.87 \pm 0.03$ ,  $2.15 \pm 0.01$  and  $1.92 \pm 0.04$  kPa respectively for ankle, mid-calf and knee sections. The deviation from FEM and experimental mechanical pressures was very small, namely 0.3%, 0.4%, and 0.5% respectively for the ankle, mid-calf and knee sections. The results obtained by the analytical modeling deviated from FEM by 4.9%, 1.1%, and 0.1% respectively for ankle, mid-calf and knee sections at the maximum stretch ratio. The analytical modeling assumed a cylindrical geometry with a final radius identical to the radius in the middle of the conical geometry of CP segments. The large error for the ankle was primarily due to the geometrical deviation from the conical shape of the ankle section. This error increased, especially for high stretch ratios. It should be noted that, in all sections, the deviation of the analytical modeling from FEM was however below 1% for stretch ratios less than 1.4.



**Figure 3-9. Mechanical pressure ( $P_m$ ) vs. the stretch ratio in ACB samples prepared for different calf regions, calculated by FEM and analytical model.**

Once the bandage was wrapped around the CP, it was actuated. Figure 3-10 shows the actuation pressure as a function of the applied electric field for the ACB samples at each CP section. In this experiment, although the ACB for the mid-calf section was stretched less than the one in the knee section, it produced larger actuation pressures as predicted in our simulations (see Figure 3-9). This result indicates that a smaller limb radius results in larger actuation pressures.

The maximum relative error between experimental and FEM results in Figure 3-10 was found to be 11.6% for the knee section. This value reduced to 1.5% and 10.2% for ankle and mid-calf sections respectively. A source of the mismatch between the experimental and modeling data was attributed to the fact that during the experiments the volume of the chambers was not perfectly set to a conical geometry – the shape did slightly change during actuation. Despite this error, experimental and FEM results displayed the same trend and were very close, as shown in Figure 3-10. Analytical simulations for the actuation pressure showed a maximum deviation from the FEM results of 1.5%, 7.3%, and 5.2% respectively for ankle, mid-calf and knee sections at the maximum applied electric field.

Figure 3-11 shows the total pressure ( $P_t$ ) when a voltage was applied to the ACBs for the three different sections of the calf. The highest set of lines corresponds to the ankle section, the middle set corresponds to mid-calf and the lowest set corresponds to the knee section. Horizontal dashed lines represent the compression value of the commercial compression stocking listed in Figure 3-7(b). Figure 3-11 demonstrates that the ACB samples could not only provide the same pressure applied by the commercial compression stockings but could also show variations around this pressure. In this figure, the error between FEM simulations and experiments was within the precision of the performed measurements. The pressure value at zero voltage shows the mechanical pressure of the ACB once it was wrapped around the CP. This value reduced upon the electrical actuation of the ACB. For example, the initial mechanical pressure of the ACB around the ankle CP segment was 2.87 kPa and upon actuation with  $8.43 \text{ V}/\mu\text{m}$  the pressure dropped to 2.73 kPa, corresponding to 5.2% drop in pressure. It should be noted that the estimation error of the analytical model in total pressure at the ankle section resulted from the estimation error in the corresponding mechanical pressure, as discussed previously (see Figure 3-9).

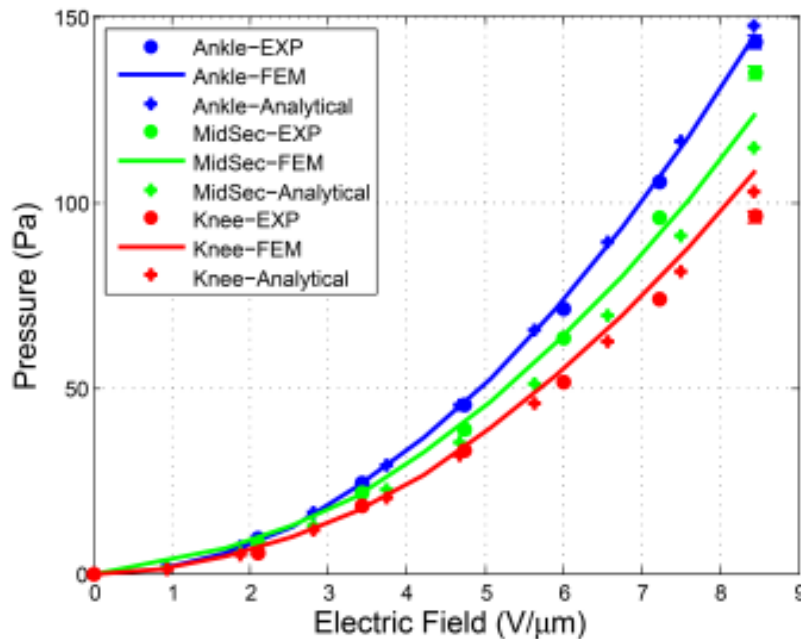


**Figure 3-10. Actuation pressure ( $P_a$ ) vs. applied electric field obtained for ACBs at different calf regions.**

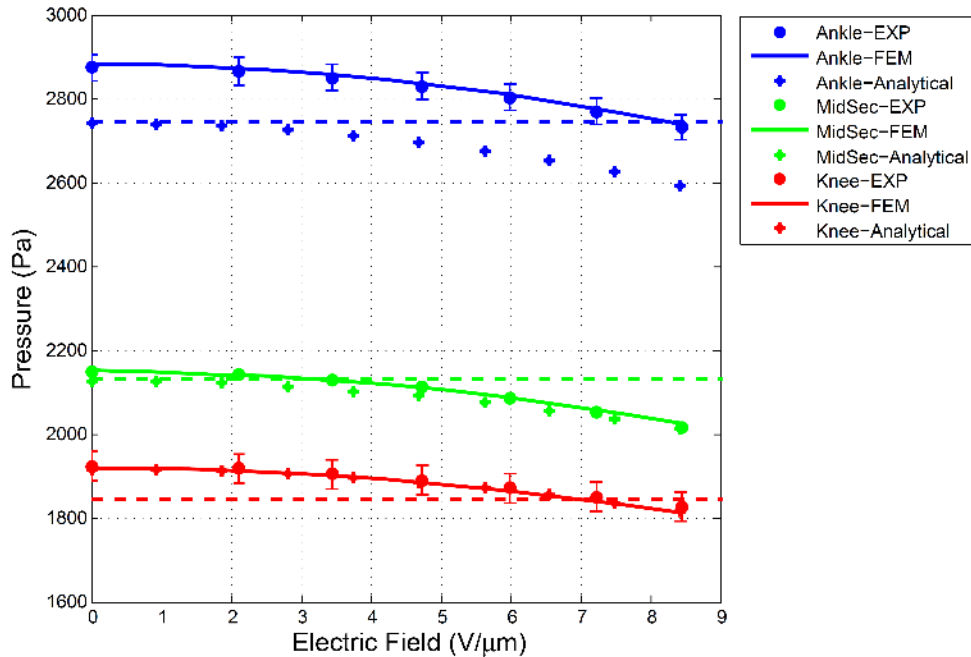


**Figure 3-11. Total pressure ( $P_t$ ) vs. applied electric field obtained for ACBs at different calf regions. Dashed lines correspond to pressures that are applied by the commercial compression stocking.**

The investigations presented in this work demonstrate that the ACB could potentially apply a variable pressure on human's lower limbs. The presented results show preliminary steps toward a smart compression bandage technology and there is room for further improvements. In order to investigate the possibility of increasing the actuation pressure, FEM simulations were carried out to predict the behavior of an ACB sample made by stacking multiple layers of the DEA.

Figure 3-12(a) shows the actuation pressure versus the applied electric field for multilayer DEA samples. This figure demonstrates that stacking multiple layers of DEA samples, each having a thickness of 1.34mm, could produce actuation pressures more than twice larger compared to a single layer DEA under the same electric field. However, it should be noted that stacking DEAs resulted in increasing the mechanical pressure of the ACB as illustrated in Figure 3-12(b). Thus, the relative pressure drop was not improved much; for example, the three-layer ACB yielded a 5.7% pressure drop compared to a 5.6% pressure drop of a single layer ACB. It should be noted that in Figure 3-12(b), the effect of the electrode layer on the stiffness of the multilayer DEA was neglected.

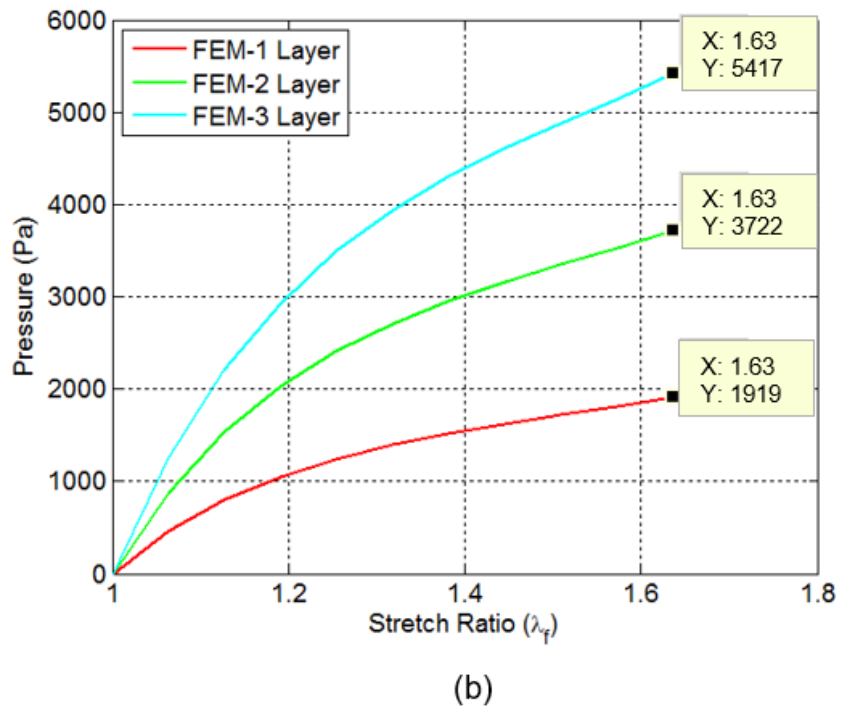
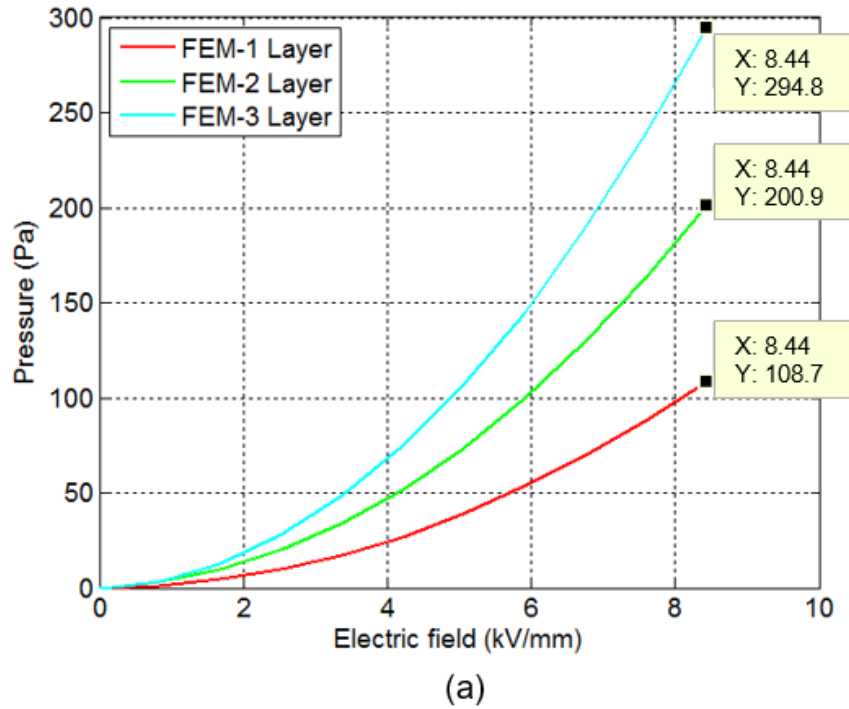


**Figure 3-12. Effects of stacking multiple-layer DEA samples for the knee section on the (a) actuation pressure at different electric fields, and on (b) mechanical pressure for different stretch ratios. The thickness of each layer was kept unchanged at 1.34 mm.**

Figure 3-13 shows the results for a multilayer DEA that was assumed to be constructed by stacking thin DEA films such that the overall thickness of the sample was

1.34mm, which is the same thickness of the previously analyzed one-layer DEA sample. Neglecting the electrode layer effects on the stiffness of the overall DEA, the mechanical pressure for the single-layer and all multilayer DEAs was the same since the thickness of the overall DEA remained unchanged. In this case, however, simulations reported that the amount of pressure drop improved to 8.0% for the three-layer ACB. The use of thin multilayers was therefore predicted to be advantageous. It should be noted that by reducing the thickness of each layer the voltage required to produce a defined electric field is reduced. Therefore, future work will focus on developing a thin multilayer ACB.

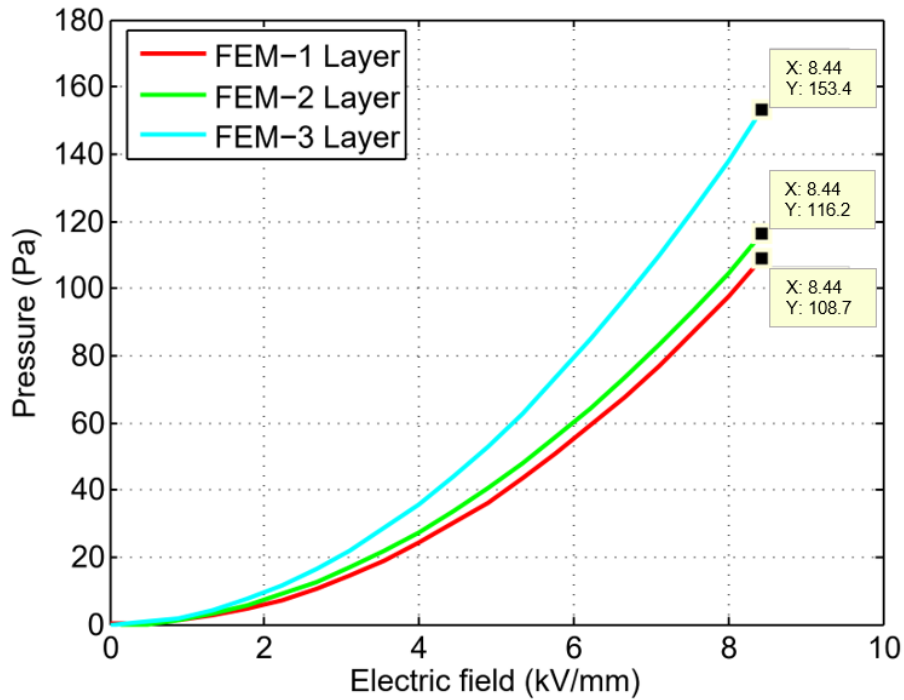


**Figure 3-13. Effects of stacking multiple-layer DEA samples for knee section on the actuation pressure at different electric fields. The total thickness of the multilayer DEA was kept unchanged at 1.34 mm.**

### 3.6. Limitations

While the proposed technology showed potentials to address disadvantages of compression stockings (by which only constant pressure can be applied) and pneumatic systems (that are not suitable for ambulatory use), it has some drawbacks which need to be addressed in future research activities. Specifically, it currently requires the use of high actuation voltages (kilovolts). Although the electrodes of ACB could be properly insulated, the risk of undesired electrical discharge is present. To reduce the voltage, a possible

solution is to use a multi-layer design. In this case, each layer would be thinner and would, therefore, require a lower voltage for a desired electric field. Another approach to reduce the high voltage risks is to use small DEA segments to limit the maximum discharge current, thus making the system inherently safe.

### **3.7. Conclusion**

In this chapter, a portable, modular and active compression bandage (ACB) based on dielectric elastomer actuator (DEA) technology was designed and prototyped. This DEA prototype could potentially be used in the treatment of different kinds of disorders associated with venous pooling in lower extremities such as DVT, orthostatic hypotension and edema. A calf prototype (CP) resembling the geometry of an average-sized human calf was designed and used as a test setup for pressure measurements. The CP was utilized to measure the compression values of the commercial compression stockings and the manufactured ACB samples. FEM simulations of the active bandage were carried out. Simulated FEM results had less than 12% deviation from the experimental data. An analytical model similar to the work of Ahmadi *et al.* [27] was also used to provide the design criteria. The analytical model proved to be suitable for the design of the ACB for stretch ratios of less than 1.4. The larger deviations from the experimental results were observed for the ankle section.

The performed research showed that the ACB could provide the same pressure exerted by compression stockings. In addition, the ACB pressure can be modulated when an electrical field is applied, thus proving that the ACB could potentially be used to provide variable mechanical pressure. This feature could potentially be used to facilitate blood return in individuals suffering from disorders associated with the lower extremities.

## Chapter 4.

### Investigating the performance of DEA-based compression bandages on the flexible human calf

Similar to chapter 3, also this chapter 4 aims at achieving the objective 2 of the thesis: “using the first modality identified in OBJECTIVE 1, i.e. negative active pressure, for a realistic application”. As stated in chapter 4, this objective comprises two sub-objectives:

2.1. Designing a DEA-based ACB by characterizing its performance through mathematical simulations and experiments; and

2.2. Considering the interaction of the ACB with the flexible and compliant human lower extremity.

This chapter 4 specifically addresses objective 2.2. complimenting chapter 3 which addresses objective 2.1. Here, the behavior of the DEA-based active compression bandage, which was proposed in the previous chapter, is further explored by mathematically examining the interaction of the bandage with the flexible human calf. Literature is reviewed to calculate a mathematical model for the volumetric changes of human calf upon application of compression. The obtained model is then used to analytically simulate the performance of the bandage on the flexible calf. The results are validated using a software-based non-linear FEM analysis. The contents of this chapter are adapted from the following publication and may have been modified to comply with the format of this thesis:

Pourazadi S, Ahmadi S, Menon C. On the design of a DEA-based device to potentially assist lower leg disorders: an analytical and FEM investigation accounting for nonlinearities of the leg and device deformations. Biomedical engineering online. 2015 Dec;14(1):103.

## 4.1. Abstract

One of the recommended treatments for disorders associated with lower extremity venous insufficiency is the application of external mechanical compression. Compression stockings and elastic bandages are widely used for the purpose of compression therapy and are usually designed to exert a specified value or range of compression on the leg. However, the leg deforms under external compression, which can lead to undesirable variations in the amount of compression applied by the compression bandages. In this chapter, the use of an active compression bandage (ACB), whose compression can be regulated through an electrical signal, is investigated. The ACB is based on the use of dielectric elastomer actuators. This chapter specifically investigates, via both analytical and non-linear numerical simulations, the potential pressure that the ACB can apply when the human leg compliance is taken into account. The work underpins the need to account for the compressibility of the leg when designing compression garments for lower extremity venous insufficiency.

A mathematical model is used to simulate the volumetric change of a calf when compressed. Suitable parameters for this calf model are selected from the literature where the calf, from ankle to knee, is divided into six different regions. An analytical electromechanical model of the ACB, which considers its compliance as a function of its pre-stretch and electricity applied, is used to predict the ACB's behavior. Based on these calf and ACB analytical models, a simulation is performed to investigate the interaction between the ACB and the human calf with and without an electrical stimulus applied to the ACB. This simulation is validated by a non-linear analysis performed using software based on the finite element method (FEM). In all simulations, the ACB's elastomer is stretched to a value in the range between 140 and 220 % of its initial length.

Using data from the literature, the human calf model, which is examined in this work, has different compliancy in its different regions. For example, when a 28.5 mmHg (3.8 kPa) of external compression is applied to the entire calf, the ankle shows a 3.7 % volume change whereas the knee region undergoes a 2.7 % volume change. The results present the actual pressure in the different regions of the calf for different values of the ACB's stretch ratio when it is either electrically activated or not activated and when the leg compliance is either considered or not considered. For example, results of the performed simulation show that about 10 % variation in compression in the ankle region is expected

when the ACB initially applies 6 kPa and the compressibility of the calf is first considered and then not considered. Such a variation reduces to 5 % when the initial pressure applied by the ACB reduced by half.

Comparison with non-linear FEM simulations shows that the analytical models used in this work can closely estimate the interaction between an active compression bandage and a human calf. In addition, compliance of the leg should not be neglected when either designing a compression band or predicting the compressive force it can exert. The methodology proposed in this work can be extended to other types of elastic compression bandages and garments for biomedical applications.

## **4.2. Introduction**

As discussed in the previous chapter 3, compression therapy is suggested to prevent and cure lower leg disorders associated with blood flow insufficiency. Compression to the lower part of the leg mimics the natural muscle contraction and helps blood return. It also increases the pressure of the interstitial fluid and decreases the superficial venous pressure. Thus, the leakage of fluids to interstitial space is reduced [104]. In this regard, compression stocking (CS) is one of the recommended devices that apply mechanical compressions to the lower leg area. CS reduces venous hypertension and helps the leg muscle pump, which improves filtration, prevents skin breakdown, and eventually results in the reduction of edema and venous pooling. Another mechanical device that prevents these disorders is intermittent pneumatic compression (IPC). IPC increases blood flow and improves blood return by simulating normal leg muscle activity. The efficacy of CSs has been questioned [66], [89] and IPCs are typically bulky and therefore not suitable for ambulatory use. Thus, dielectric elastomer actuators (DEAs) were introduced in the previous chapter as active compression bandages (ACBs) to address the shortcomings of the currently available devices. In particular, DEAs can apply a variable (time-dependent) mechanical compression using an input electrical stimulus. Variable compression has been shown to be more efficient than a static compression in different studies [92], [105].

The quantity of external compression is an important factor in treating the previously mentioned disorders in the lower extremities. For instance, it was shown that an external compression of 35–40 mmHg was required at the ankle to prevent edema in

patients with severe venous disease [106]. Also [107] suggested that in order to optimize the venous flow in the lower leg, graded compression of 18 mmHg at the ankle, 14 mmHg at mid-calf, and 8 mmHg at the knee is required. Thus, the bandages used for compression therapy should be designed to apply the proper range of compression. Typically, the amount of pressure exerted by elastic bandages is a function of the calf geometry. In practice, the calf is compressible and its volume and geometry change upon compression. Thus, the amount of compression that elastic bandages exert differs depending on the volume and shape of the calf. In this regard, Stenger et al. suggested that volumetric changes of the leg should be considered prior to the design of elastic bandages [63]. Therefore, it is interesting to study and identify how profound the calf compressibility would affect the behavior of the DEA bandage.

In this chapter, an analytical study and a numerical simulation based on the finite element method (FEM) are proposed to simulate the interaction between the ACB and the calf. The results of this study assist in predicting how calf compressibility affects the performance of an ACB and the use of this technology in future clinical studies.

### 4.3. Mechanical properties of the calf

The human calf compresses upon the application of pressure. The geometry and size of the calf change considerably with the application of external compression. The relationship between changes in volume to changes in external pressure is often determined by its compliance (C):

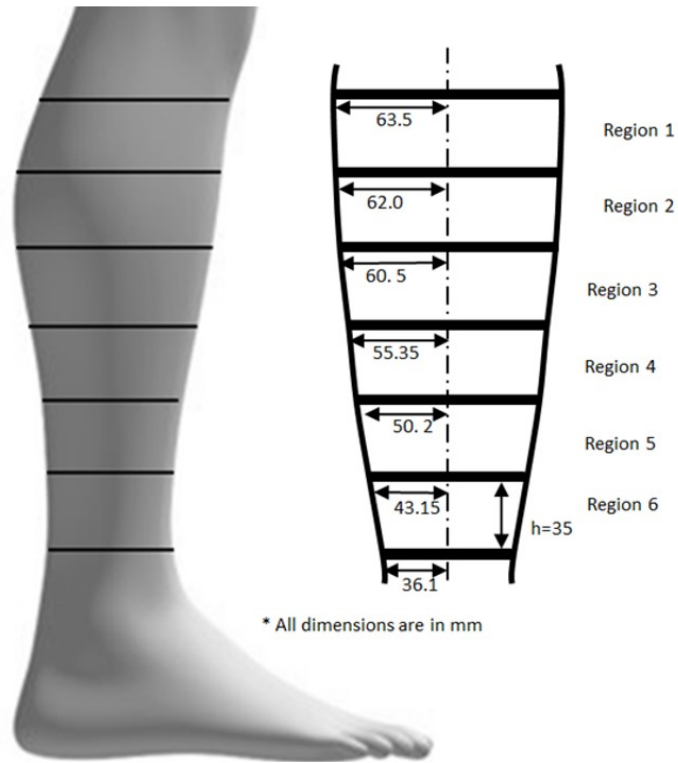
$$C = \frac{\delta \Delta V}{\delta P}. \quad (1)$$

The compliance is a nonlinear function of external pressure and different regions of the calf show different values. There are several works in the literature that studied and measured the calf compliance with different methodologies [108]–[115]. The common clinical method of calf compliance measurement is to apply external pressure proximal to the knee with congestion cuffs and then monitor the volume changes in the calf area using plethysmography [108]–[112]. In this method, it is assumed that the volume change in the limb is equivalent to a volume change of the underlying venous vessel. This assumption, however, is argued to be not very accurate [115]. Moreover, this method is believed to not precisely predict the compliance of the calf as the external pressure is applied proximal to

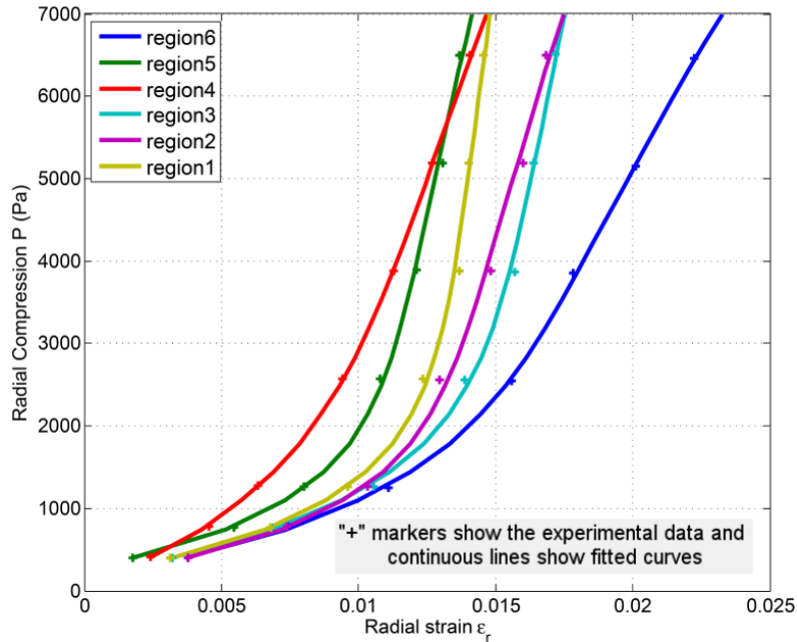
the knee and not to the calf itself. A more sophisticated method was however used to accurately measure the calf compliance by monitoring cross-sectional changes of the calf under application of external pressure to the calf area [114], [115]. Specifically, Thirsk et al. [115] proposed a procedure that removed possible artifacts, such as involuntary muscle contractions, from the measurements to obtain accurate measurements. In that work, compliance was measured in six regions of the leg, from the ankle to the knee (labeled as region 6 to 1 from now onward as it is shown in Figure 4-1(a), in 3 human subjects. The calf compliance was presented in the plots of calf cross-sectional area change versus external pressure change.

In this work, the compliance data acquired by Thirsk et al. [115] was digitalized from their published report. The values of the percentage change in the cross-section area of the calf were divided by 2 to obtain the radial strain. This operation is considered to be a valid conversion assuming a uniform geometrical shape of the calf cross-section [116]. True stress-strain data points were calculated from the pressure-radius change data set for each of the six regions of the calf. A curve fitting was then used to fit the best function for the relation between the true radial stress ( $P$ ) in “Pa” on the calf and the true radial strain ( $\epsilon_r$ ). The stress-strain curves for all calf regions are depicted in Figure 4-1(b). For all regions, the best-fitted curves were found to be an exponential function of the form presented in Eq. (2). The curves in Figure 4-1(b) are a continuation of curves that yield 0 strain at 0 pressure, thus a single exponential term cannot accurately follow this behavior and a second term was added in Eq. (2) to address this issue. The corresponding constant parameters are provided in Table 4-1.

$$\epsilon_r = a \cdot e^{b \cdot P} + c \cdot e^{d \cdot P} \quad (2)$$



(a)



(b)

Figure 4-1. Human calf. a Conical geometry of the calf and its six different regions. Each region is assumed to be 35 mm apart in height [117]. b Fitted curves to calf compliance data obtained from [117] the calf's different regions.

**Table 4-1. Constant parameters of the calf compliance relation expressed in Eq. 1.**

Region	a	b	c	d
6	0.013392	7.898E-05	-0.01600	-0.001137
5	0.009989	4.967E-05	-0.01465	-0.001386
4	0.008678	7.532E-05	-0.00913	-0.000828
3	0.01373	3.492E-05	-0.01686	-0.001133
2	0.01188	5.511E-05	-0.01466	-0.001392
1	0.012223	2.731E-05	-0.01513	-0.001263

#### 4.4. Analytical modeling of the DEA on a simulated human calf

In this section, an analytical model of the cylindrical DEA is combined with the model of the human calf described by (2). The total pressure applied by the ACB consists of two components, the mechanical pressure which is the pressure resulting from the mechanical stress in the ACB before actuating the ACB, and the actuation pressure, which is the pressure variation after actuating the ACB. The ACB is assumed to be made out of a flat DEA with length  $L$ . This flat DEA can be bent to form a cylinder with an external radius of  $R = \frac{L}{2\pi}$ . The ACB is stretched radially as it is wrapped around the calf and the following stretch ratio  $\lambda$  can be used:

$$\lambda = \frac{r}{R} \quad (3)$$

where  $r$  is the radius of the ACB when it conforms to the calf. Since the geometry of the calf is conical, the ACB undergoes different stretch ratios along the height of the calf.

In the analytical modeling of this work, it was assumed that the conical geometry of each calf region was formed from a finite number of small cylindrical geometries with finite heights. The simulation procedure, which is explained in this section, was done for each of these small cylindrical geometries and the final values of radius and pressure were averaged over the entire calf region. As the stretch ratio of the ACB changed the amount of compression that was exerted on the calf was also changed. The amount of this compression was obtained using the following equation [27].

$$P_m = \int_{\lambda_b}^{\lambda_a} -\frac{\mu_1(\lambda^{\alpha_1} - \lambda^{-\alpha_1}) + \mu_2(\lambda^{\alpha_2} - \lambda^{-\alpha_2})}{\lambda(\lambda^2 - 1)} d\lambda \quad (4)$$

where  $\lambda_a$  and  $\lambda_b$  are stretch ratios of inner and outer radii of the cylindrical DEA respectively, and  $\mu_1, \mu_2, \alpha_1, \alpha_2$  are the ogden parameters for the DEA material. As the ACB compression was being applied, the calf radius changed. Assuming  $R_c$  as the radius of the undeformed calf (as shown in Figure 4-2),  $\lambda_c$  was defined as the calf stretch ratio:

$$\lambda_c = \frac{r}{R_c} = \frac{R}{R_c} \lambda \quad (5)$$

$$\lambda_c = 1 - \varepsilon_r. \quad (6)$$

Substituting (2) in (6) and using (5), the calf radius after application of  $P_m$  was obtained:

$$r = R_c - R_c(ae^{bP_m} + ce^{dP_m}). \quad (7)$$

In order to find the equilibrium state for  $r$  and  $P_m$ , the set of coupled equations, (4) and (7), was solved. Since the equations were nonlinear and neither  $r$  nor  $P_m$  could be written in terms of each other explicitly, a closed-form analytical solution could not be obtained. Hence, an iterative procedure was used to solve (4) and (7) for the final calf radius  $r$  and the external mechanical pressure  $P_m$  applied by ACB. In the first iteration of this procedure, the calf was undeformed and the ACB was stretched to  $R_c$ . Using (4) a compression  $P_m$  was obtained. Then using (7) a new calf radius  $r$  was calculated. In the next iteration,  $P_m$  was re-calculated using the new calf radius and subsequently, a new calf radius was calculated. These iterations are continued until the value of  $r$  changes less than 0.01 % of the initial radius  $R_c$ .

Once the bandage was wrapped and equilibrium was reached for the radius, the actuation phase was modeled and analyzed. The actuation pressure was calculated from the following equation [27]:

$$P_a = \frac{\varepsilon_0 \varepsilon_r V^2}{2 \ln^2(b/a)} \frac{b^2 - a^2}{a^2 b^2}. \quad (8)$$

As discussed earlier the total ACB pressure on the calf was composed of  $P_a$  and  $P_m$  and is given by:

$$P_t = P_m - P_a \quad (9)$$

As it is evident in (9), the ACB total pressure was reduced upon actuation. Thus, the radius of the calf was increased which in turn resulted in an increase of the ACB

mechanical pressure. So, equations (7) and (9) could be solved to find the final equilibrium state of the calf radius  $r$  and the total pressure  $P_t$  from the actuated ACB. These equations were solved similar to the previously mentioned iterative procedure. The steps of this iterative procedure are summarized in Figure 4-3.

The developed analytical model facilitated the ability to predict the behavior of the ACB on the flexible calf. Moreover, it provided a tool to design the ACB parameters in such a way to achieve desired compressions on the lower leg. Using the analytical model, simulations were carried out for the six regions of the calf and the results are discussed in the following sections.

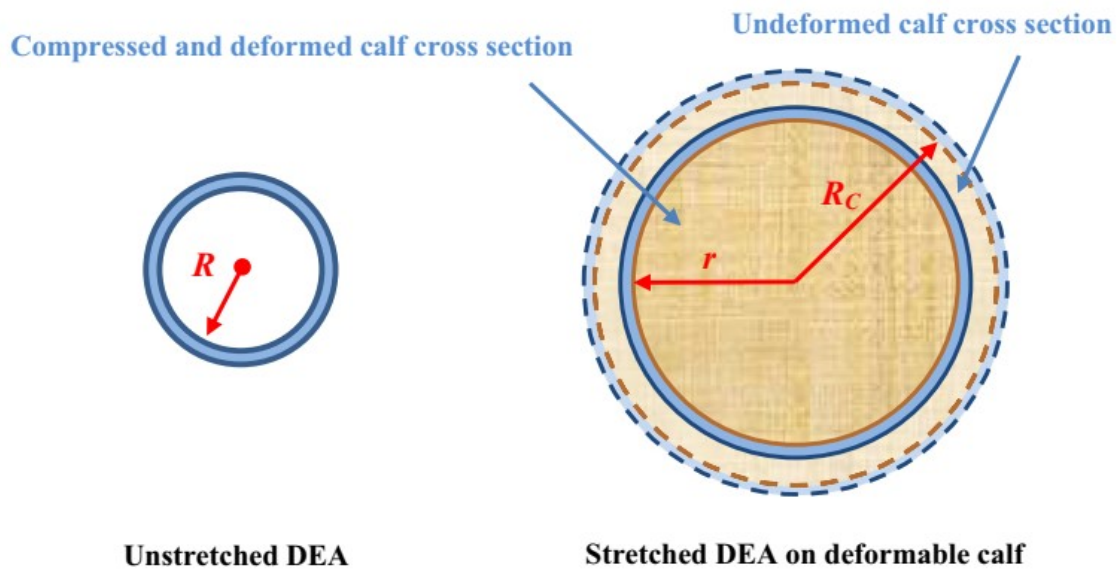


Figure 4-2. Changes of the ACB radius on the compressible human calf.

## 4.5. FEM analysis

Finite element modeling showed promising results for cylindrical and conical DEA geometries in previous chapter 3 and also in literature [27]. In the previous chapter, FEM was used to analyze the behavior of the ACB on a lower human leg geometry. The calf was assumed to be incompressible and the volume change effects in the lower leg region were neglected. However, in reality, the calf volume changes when external pressure is applied. To numerically analyze the behavior of the ACB on the compressible human calf, ANSYS software (Ansys Mechanical APDL 2011 ANSYS Inc V14.0) was used.

In this chapter, the ACB was originally modeled as a cylinder (as shown in Figure 4-4) and a 2nd-order Ogden model was used to approximate its hyperelastic behavior. Ogden parameters from chapter 3 were used. A truncated cone with specific dimensions (as shown in Figure 4-4) was modeled for each calf region. A total of six regions were studied. The cone height for all regions was 35 mm. Every calf region had a different material property and required different nonlinear model parameters. A Hyper-elastic Response Function model was used to model the calf material in each region. In this model, the material's compressibility is specified by  $d_1$  parameter which is the inverse value of the bulk modulus. Further details of this material model, which is a built-in model in Ansys, can be found in Ansys documentation [103].

After creating the ACB and calf regions in the model, a fine FEM mesh was needed to be generated to obtain high-accuracy results. By selecting a finer mesh, although the accuracy of results was improved, the simulation time was rapidly increased as well. Therefore, an optimum mesh size was needed to be determined to achieve accurate results within a reasonable simulation time. As there was rotational symmetry for both the ACB and the calf geometries, only 1/4th of the geometries were modeled (as seen in Figure 4-4). For the ACB, the geometry was meshed into 3 segments along the thickness, 15 segments along the circumference, and 20 segments along the height of the 1/4th cylinder.

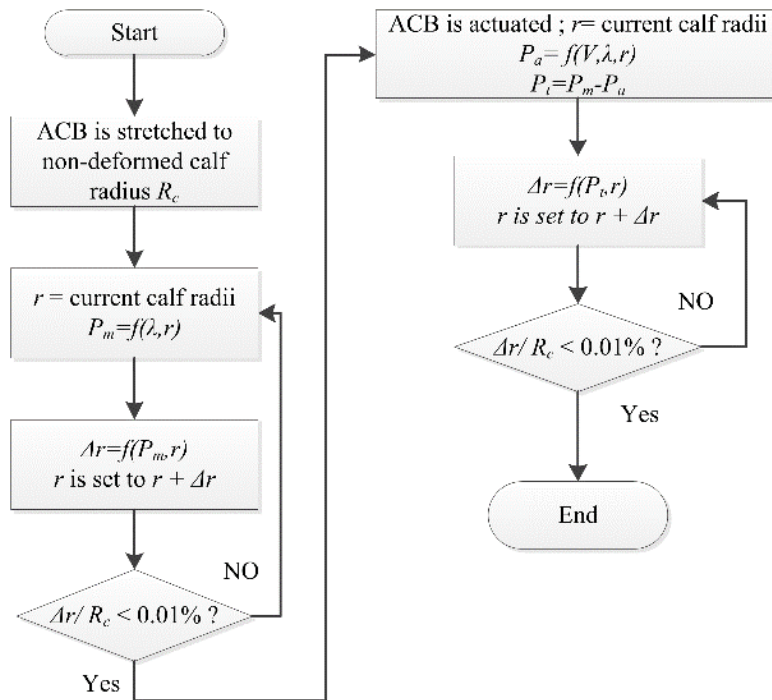
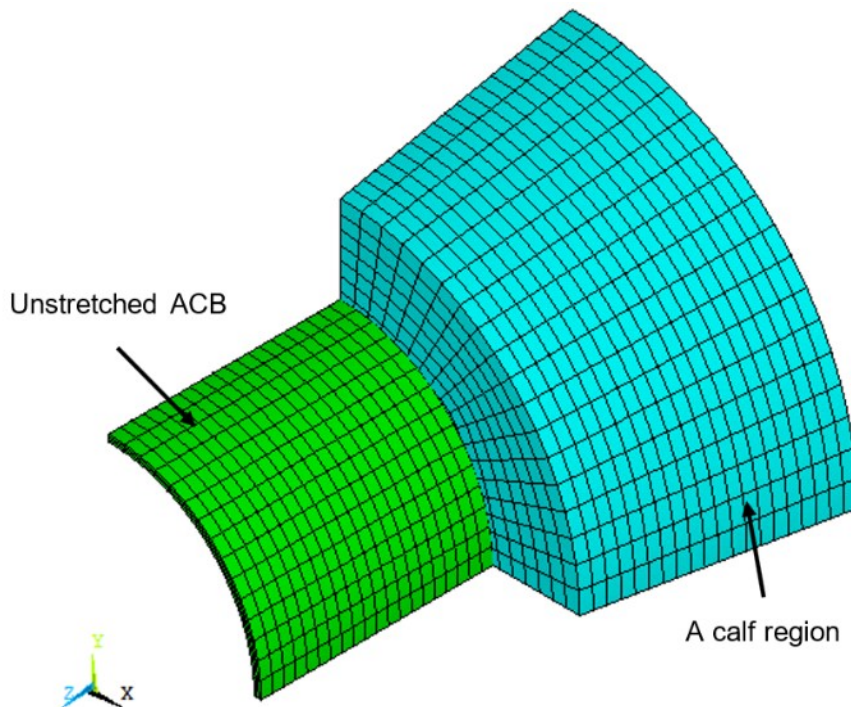


Figure 4-3. Flowchart of the analytical modeling of the ACB on the flexible calf.



MENVA/MODELING DEA-STOCKINGS

Figure 4-4. Geometry of the calf and ACB in FEM simulations

The calf geometry was also meshed into  $18 \times 18 \times 20$  segments respectively along its radial, circumferential and axial directions. Also, a total of 300 contact elements and 360 target elements were used in the model. To include the electro-active properties of the ACB in simulations, Solid226 (a higher-order 3-D 20-node solid element with electrostatic material option) was selected. Also, Solid186 (a higher-order 3-D 20-node solid element) was chosen for the calf geometry. For the contact areas of the ACB Conta174 (a 3-D 8-node surface-to-surface contact element) and for the calf's contact area Targe170 (a 3-D target element) was used. Moreover, a frictionless contact was assumed between the solid geometries.

In reality, an ACB bandage was wrapped around the calf and then was actuated. To avoid modeling a complicated contact problem and to reduce the calculation time, an alternative procedure which gave identical results was considered. The simulation steps were: (1) the sides of the ACB were fixed (to keep the height constant at 35 mm) and the ACB was stretched radially to the size of the largest radius of the calf region; (2) the stretched ACB was then displaced to perfectly locate on the calf region; (3) the radial constraint was removed to release the ACB and make contact with the calf region. The sides of both the ACB and the calf segment were kept fixed and the contact pressure and volume changes were reported as outputs. The ratio of the average calf radius (mean of smaller and larger calf radii) to the initial ABC's inner radius was defined as the stretch ratio ( $\lambda$ ) which was chosen to vary from 1.4 to 2.2 in this study; (4) the ACB was actuated by applying an electrical potential difference of 11.3 kV between the top and bottom surfaces of the ACB. The pressure difference and volume changes were the outputs of this step. Simulation steps are shown in Figure 4-5.

In the FEM setup explained above, there were 900 ACB elements, 6480 calf elements, and 660 contact elements. The total computation time for an ACB sample in contact with the calf region 6 varied from 5.5 to 9.5 h for stretch ratios of 1.4 and 2.2, respectively. It was found that the most time-consuming step is the 3rd step as the ACB makes initial contact with the calf region. A desktop PC with AMD FX™ -8350 eight-core (4.7 GHz) processor and 16 GB of RAM was used. All CPU cores were fully utilized using ANSYS High Performance Computing (HPC) feature. To study the effect of mesh size on the accuracy of results, a second run was performed by selecting  $4 \times 20 \times 25 = 2000$  ACB elements,  $20 \times 20 \times 25 = 10,000$  calf elements, 500 contact elements, and 500 target elements. If the ACB sample was deformed to a stretch ratio of 2.2 the simulation finished

after 42.5 h and the mechanical pressure after a full contact in step 3 was 6091.2 Pa. However, the coarser mesh size that was selected originally gave a nearly similar mechanical pressure, 6102.8 Pa. The relative error for such large pressures was less than 0.19 % with coarser mesh size but the calculation time was about 4.5 times shorter. Therefore, the coarser mesh size was chosen and simulations were performed for five different stretch ratios (range of 1.4–2.2 with 0.2 increments) and for all six calf regions. The results are discussed in the next section.

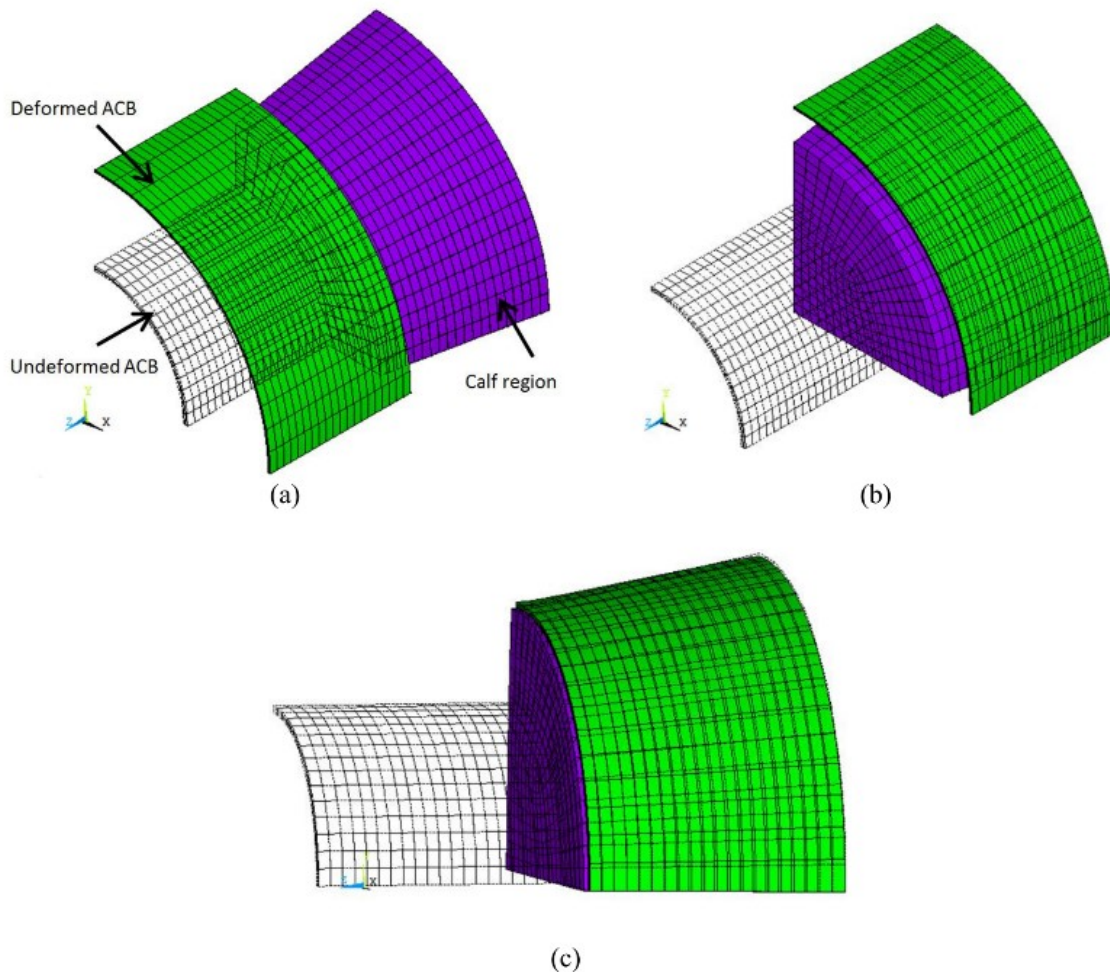


**Figure 4-5.** Deformation plots showing the position of the ACB and the calf region at the end of each FEM load step. (a) ACB is radially stretched to the maximum radius of the calf region; (b) ACB is positioned at the top of the calf region; (c) ACB is released to make contact with the calf region. The deformation plot of the electrically actuated ACB is similar to the plot (c) since the deformations are not considerable upon actuation. At each load step, wireframe lines show the geometries before deformation starts and solid shapes show the deformed geometries.

## 4.6. Results and discussion

Different sizes of ACBs were investigated to study the effect of the initial length of the ACB and also cover a wide range of compressions on the calf. An ACB thickness of 1 mm with a dielectric constant of 7.41 was used for the simulations. Ogden parameters similar to chapter 3 were used to simulate the hyperelastic behavior of the elastomer. Also, the ACB was actuated with 11.3 kV DC voltage for all simulations.

The initial lengths of the bandage were determined in order for the ACB to undergo a certain range of stretch ratio (i.e. 1.4–2.2) considering the non-deformed shape of the calf. However, as discussed earlier, the calf deforms under compression and thus the actual stretch ratio differs from the initially desired stretch ratio. In this work, the results are presented in terms of the initially desired stretch ratio for better consistency. Table 4-2 shows the values of the ACB lengths for the different calf regions and initial stretch ratios.

The simulation results of the analytical and FEM modeling that were explained in “Analytical modeling of the DEA on a simulated human calf” and “FEM analysis” are followed in this section. Figure 6 shows the final volume of the different calf regions for different initial stretch ratios of the ACB after the ACB was wrapped and actuated. In this figure, the analytical and FEM results are represented with solid lines and circle markers, respectively. The maximum relative difference between the analytical and the FEM simulations was 2.4 % which was happening in region 6 for  $\lambda = 2.2$ . The detailed list of the volumes is listed in [https://static-content.springer.com/esm/art%3A10.1186%2Fs12938-015-0088-3/MediaObjects/12938\\_2015\\_88\\_MOESM1\\_ESM.xlsx](https://static-content.springer.com/esm/art%3A10.1186%2Fs12938-015-0088-3/MediaObjects/12938_2015_88_MOESM1_ESM.xlsx).

Figure 4-7 shows the relative change in the volume of the different calf regions ( $E_v$ ), defined by Eq. (10) versus different initial stretch ratios of the ACB.

$$E_v = \frac{V_0 - V_A}{V_0} \times 100 \quad (10)$$

where  $V_0$  was the initial calf volume and  $V_A$  was the calf volume after wrapping and actuation of the ACB that was given in Figure 4-6.  $V_0$  is also plotted on the secondary axis of Figure 4-7. The analytical simulations in Figure 4-7 suggest that after wrapping and actuating the ACB the calf underwent a maximum of approximately 4.4 % volume change at the ankle region.

**Table 4-2. Initial ACB lengths in centimeter.**

Calf region \ Stretch ratio	1.4	1.6	1.8	2	2.2
1	28.2	24.6	21.9	19.7	17.9
2	27.5	24.1	21.4	19.2	17.5
3	26.0	22.7	20.2	18.2	16.5
4	23.7	20.7	18.4	16.6	15.1
5	20.9	18.3	16.3	14.7	13.3
6	17.8	15.6	13.8	12.4	11.3

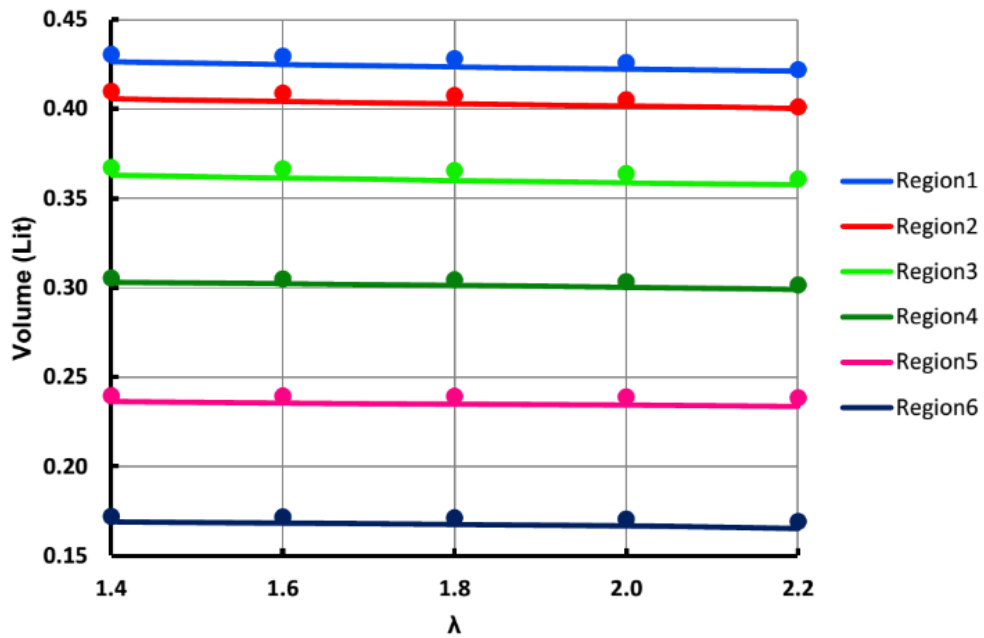


**Figure 4-6. Analytical (solid lines) and FEM (circle markers) results for volume variations in various regions of the calf and different stretch ratios.**

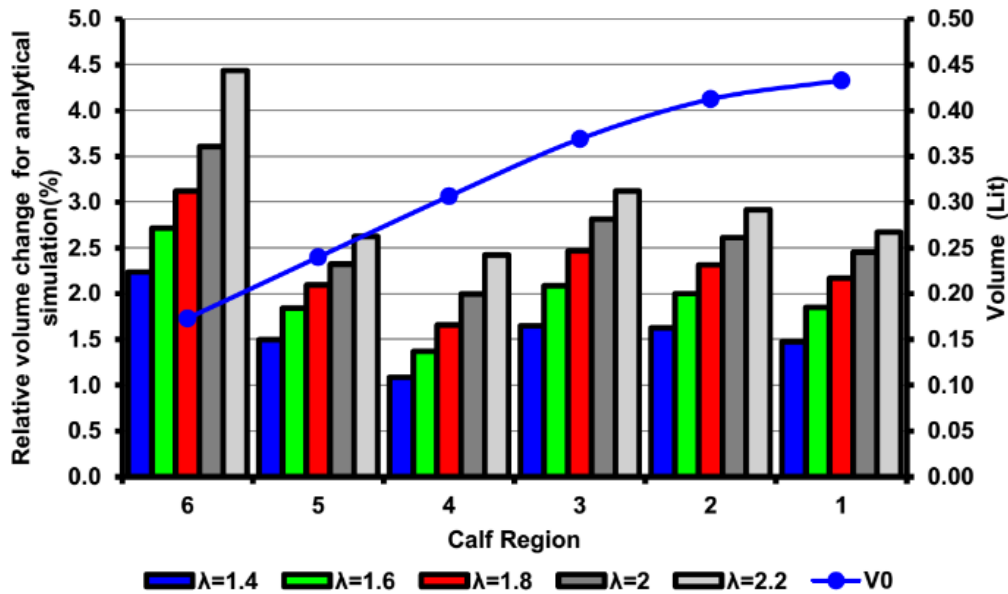


**Figure 4-7. Relative change in the calf volume after wrapping and actuating the ACB. Each color represents a stretch ratio. The secondary axis on the right-hand side shows the calf region's initial volume indicated by the solid line with circle markers.**

For a certain stretch ratio, the maximum relative volume change took place in region 6 while the minimum was in region 4. The effect of volume changes on the performance of the DEA bandage is shown in Figure 4-8 to Figure 4-12. Figure 4-8 shows the difference between the FEM and the analytical simulations for the total pressure on regions 1 and 6 for the two cases of considering a volume change (VC) and no volume change (NVC). The maximum difference between results from the analytical and FEM methods was 2.9 % in region 6 at  $\lambda = 1.4$ . The FEM simulation results are shown in Figure 4-6 and Figure 4-8 verified that the analytical model can closely estimate the ACB behavior on the human calf. For further reference, a table of total pressure results is included in [https://static-content.springer.com/esm/art%3A10.1186%2Fs12938-015-0088-3/MediaObjects/12938\\_2015\\_88\\_MOESM2\\_ESM.xlsx](https://static-content.springer.com/esm/art%3A10.1186%2Fs12938-015-0088-3/MediaObjects/12938_2015_88_MOESM2_ESM.xlsx).

Figure 4-9 shows the analytical results for the total pressure in all calf regions and illustrates the effect of considering volume change (VC) on the total pressure of the ACB. In this figure, each column group represents a specific initial stretch ratio for all sections of the calf. For each column, the bottom stack represents the total pressure after considering VC in the calf and the upper stack is the difference between considering VC and no volume change (NVC) in the calf.

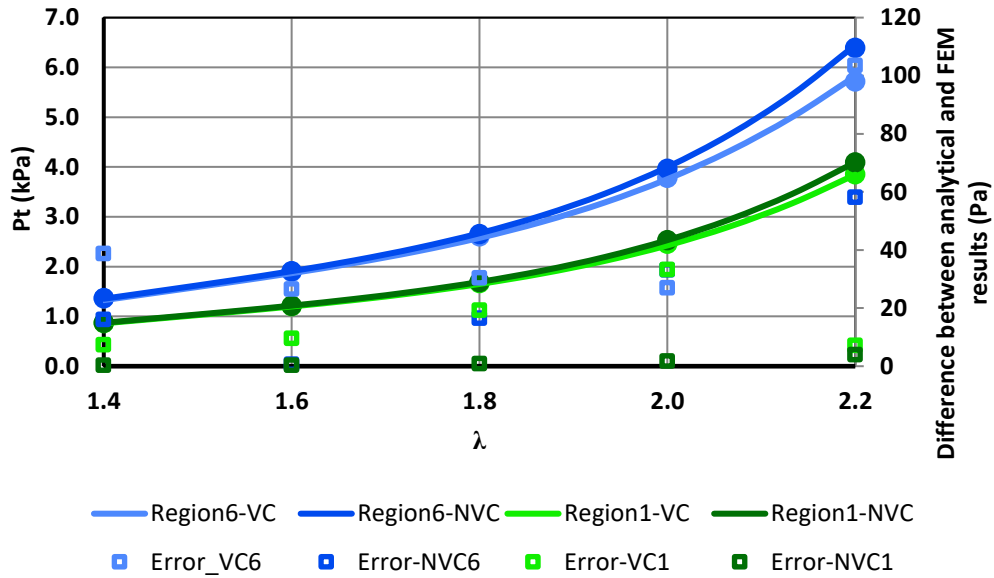


Figure 4-8. FEM (circle markers) and analytical (solid lines) results of the total pressure for regions 1 and 6.

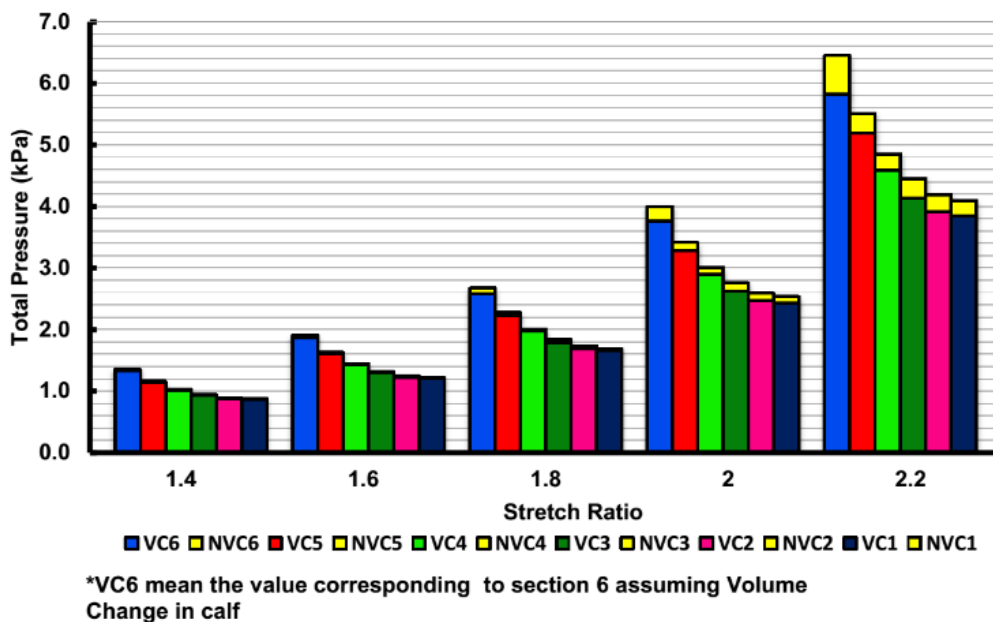


Figure 4-9. The ACB total pressure in all calf regions for different stretch ratios.

Thus, the combined height of each column represents the total pressure for the NVC case. Figure 4-9 shows that for a specific stretch ratio, the total pressure increases as we move from the knee to the ankle. It also shows that for a specific calf region the total pressure increased as the stretch ratio increased. However, the change in total pressure between the two cases of VC and NVC (shown by the second stack in each

column/yellow color) was not uniformly decreasing or increasing and is a function of the compliance of the calf region. This change in total pressure followed the same pattern as the relative volume change in Figure 4-7. Since region 4 has the lowest compliance (as shown in Figure 4-1(b)), the change in total pressure was minimal for this region. These changes in the total pressure are also illustrated in Figure 4-10. For a constant stretch ratio, the change in total pressure was the lowest for region 4. The maximum change in total pressure corresponded to the ankle (region 6) and a 2.2 stretch ratio with a 9.7 % change.

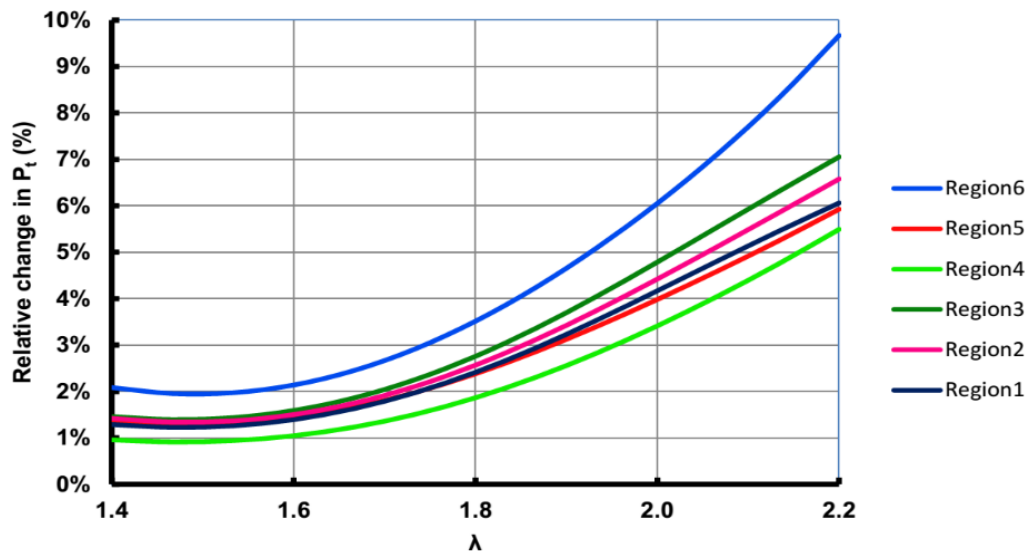


Figure 4-10. Percentage of change in the ACB total pressure between the two cases of VC and NVC.

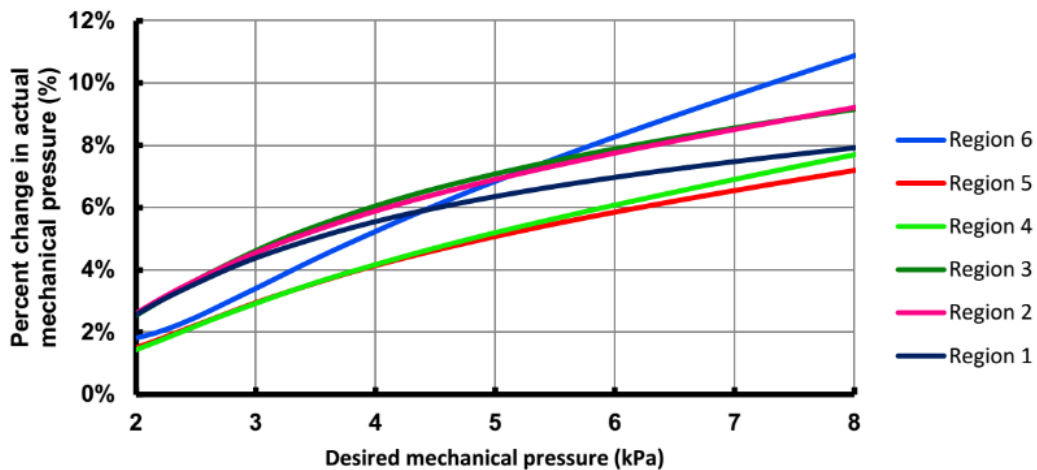
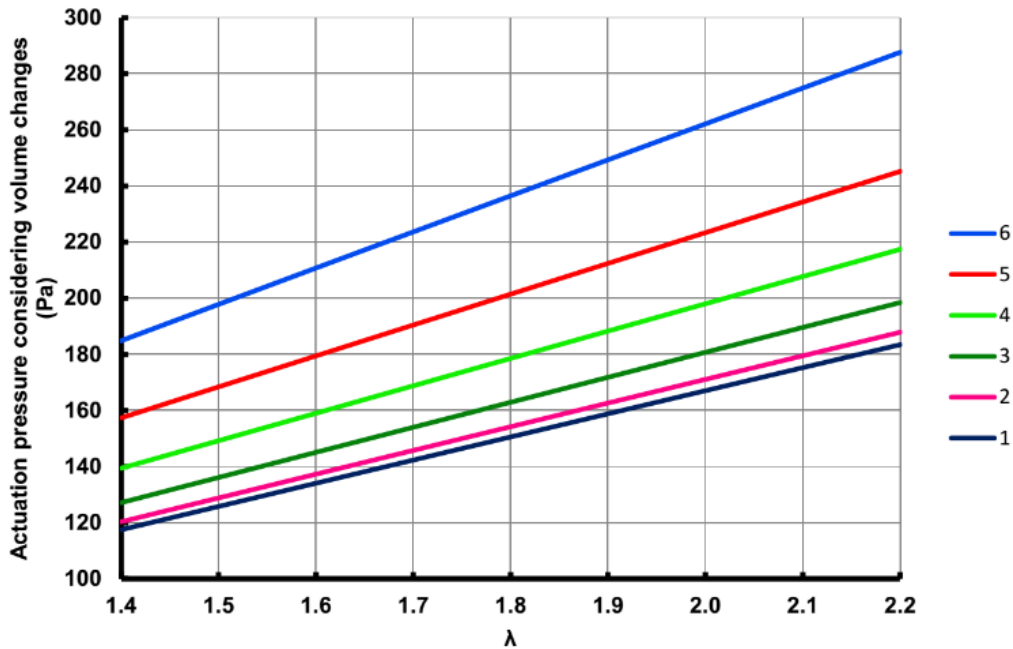


Figure 4-11. Difference between actual and expected values in mechanical pressure as a result of calf compressibility.



**Figure 4-12. ACB actuation pressure for different calf regions.**

These results imply that if the volume change in the ankle was considered, a total pressure of 5.82 kPa (43.6 mmHg) was achieved instead of 6.45 kPa (48.4 mmHg) which corresponds to a 630 Pa (4.7 mmHg) reduction in the total pressure. After region 6, region 3 had the highest change in total pressure with 7.1 % of change.

As mentioned earlier, the amount of pressure that the ACB exerted before electrical activation was denoted by mechanical pressure. The mechanical pressure of the ACB increased as the stretch ratio of the ACB increased. Also, this mechanical pressure generally increased as the radius of the calf reduced. Thus, for a specific stretch ratio, the amount of mechanical pressure was higher at the ankle section compared to other regions of the calf.

One of the important rationales for this study is better explained using Figure 4-11. Often the mechanical bandages are designed to provide a desired mechanical pressure. However, in practice, the amount of mechanical pressure changes due to the compressibility of the calf. In this case, the ACB can be stretched more to apply a higher amount of pressure and counteract the effect of volume change. Figure 4-11 shows the percent of change in actual mechanical pressure for a range of desired mechanical pressures. For example, if the bandage is designed to provide a desired mechanical pressure of 4.90 kPa (36.8 mmHg) on the ankle, the actual mechanical pressure would be

reduced by 6.7 % which is equivalent to 330 Pa (2.5 mmHg), making the actual mechanical pressure 4.57 kPa (34.3 mmHg). Variation of the actual compression from the desired compression by elastic bandages is an important fact that can lead to improper treatment of lower leg disorders [63]. Thus, it is proposed that the designed mechanical pressure be increased by the percentage suggested in Figure 4-11 to compensate for compression variations due to the changes in the calf volume.

In Figure 4-12 the actuation pressure of the ACB, which is the pressure drop of the ACB once activated with 11.3 kV voltage, is shown for different sections of the calf. A voltage of 11.3 kV was used in order to conduct a study consistent with chapter 3. As was also discussed in chapter 3, the amount of activation pressure increased as the radius of the calf was reduced. As shown in Figure 4-12, the actuation pressure changed almost linearly with respect to the changes in stretch ratio. The maximum actuation pressure was 287.7 Pa (2.2 mmHg) which corresponded to the ankle region.

As mentioned earlier, applying a graded compression that reduces from ankle to knee is one of the recommended treatments for disorders associated with lower leg blood pooling [63]. One way to generate a compression that gradually reduces from ankle to knee is by making independent ACB short modules with different sizes for different calf sections. Each ACB module covers a single region of the calf and can be stretched independently, allowing for various compression profiles along the calf. Figure 4-9 provides the required stretch ratios that each ACB at each calf section should have in order to apply the desired compression profile. In this modular design, every single module could be actuated individually in order to generate an arbitrary variable compression such as peristaltic compression. This modular design, although challenging, provides a high degree of freedom to cover a wide range of dynamic compression profiles.

## **4.7. Limitations**

This work investigated a recently proposed technology that potentially addresses some of the disadvantages of current compression therapy devices for the lower leg disorders. It should be noted that the investigated technology is still in its early stage of development, which justifies this study aimed at predicting the ACB behavior when a compressible human calf is considered.

The ACB faces some challenges and limitations that would need to be addressed in future studies. Specifically, DEAs are generally actuated with high actuation, which may pose limitations for use in wearable devices. The use of a stack of thin actuators could be used to address this challenge, as voltage could drastically be reduced. The use of a source not able to provide sufficient current to cause possible harm could also be considered.

Another aspect that should be considered is the prolonged use of ACB in contact with the human skin. Future studies should investigate the use of a layer of anti-allergic, breathable fabric laid at the interface between ACB and skin, which wicks away the skin sweat and moisture. Such fabrics are currently used in available compression garments [118]. The use of alternative materials for the ACB should also be studied.

Future studies should also consider the effect of the stress relaxation behavior of DEAs and its implications in the use of active compression garments, such as the one investigated in this work. It should, in fact, be noted that the stress relaxation in the ACB's elastomer may potentially present a considerable reduction in the mechanical compression of the ACB over time. The amount of relaxation depends on the material of the elastomer and is a function of time, temperature and stress/strain level. Typically, the level of relaxation is very large and considerable in acrylic elastomers, however, it is small particularly in silicone elastomers [19]. Typical acrylic elastomers show up to 500 % stress reduction after settling time of about half an hour for stretch ratios as low as 1.5 [119] while silicone elastomers can demonstrate less than 4 % stress reduction after settling time of 2 h for stretch ratios up to 2 [20]. Thus, the level of stress relaxation must be determined based on the material and the level of maximum stretch ratio used when wearing the ACB. Materials with low or negligible stress relaxation should be used in the fabrication of the ACB to lessen the reduction of mechanical compression on the limb due to the relaxation.

For the prototype investigated in this work, Figure 4-10 shows that the ACB's total pressure would reduce by around 4 % for a stretch ratio of 2 solely due to the calf compressibility. This amount of reduction in mechanical compression, as a result of the calf compressibility, would be comparable to the 4 % reduction in compression due to the stress relaxation [20]. Thus, it can be concluded that the effect of stress relaxation may considerably affect the performance of the ACB. While future investigations should address this aspect by investigating novel materials, simple pragmatic solutions could also

be implemented. For instance, the ACB could be stretched more than needed when initially donned in order to compensate for the subsequent relaxation of the material. Alternatively, the ACB could be embedded with a suitable tightening mechanism, such as the Boa closure system [120]. This solution would enable the user to tighten the ACB when needed to compensate for the compression reduction due to the relaxation.

## 4.8. Conclusion

In this chapter, the behavior of the active compression bandage (ACB) made out of dielectric elastomer actuator (DEA) was studied on a simulated human leg. ACBs could potentially be used in the treatment of different types of disorders associated with venous pooling in lower extremities such as orthostatic hypotension and edema. External compression on the lower leg helps balance the capillary filtration and venous return which in turn results in the reduction of venous pooling and normalizing the blood return. The literature suggests that compression of 35–40 mmHg (4.67–5.33 kPa) at the ankle is required to prevent edema in patients with varicose veins. Also, graded compression of 18 mmHg (2.40 kPa) at the ankle, 14 mmHg (1.87 kPa) at mid-calf and 8 mmHg (1.07 kPa) at knee optimize the blood flow in the lower leg.

Since the human calf is flexible and compressible, the size and shape of the calf change upon the application of external compression. The literature was reviewed to obtain a relation between external pressure and change in volume of the calf (i.e. compliance). Different methods were discussed in this regard and finally, a model for the relation between external compression and radial strain of the calf was developed based on [115]. This model was incorporated with analytical models available for the DEA. An iterative process was used to solve the system of equations. Also, a FEM model was developed to simulate the contact problem between the ACB and the human calf. Results from the FEM model were used to cross-validate the analytical simulations. The maximum relative difference between the FEM and the analytical modeling was as low as 2.9 %. The simulations demonstrated the values of the calf volume change under various compressions on different calf regions. For example, the calf underwent a 4.4 % volume change for an external pressure of 44 mmHg (5.82 kPa) at the ankle region. This change in volume can possibly be a considerable issue in analyzing stiff bandages with large young modulus.

In this chapter, it was shown that calf compressibility caused variations in the amount of compression exerted by elastic bandages. Specifically, the actual amount of compression by elastic bandages is different from the expected value. In the case of using the ACB, consideration of ankle flexibility resulted in approximately 9.7 % variations in the total pressure of the ACB for a case when the initial mechanical pressure of the ACB was 50 mmHg (6.70 kPa). However, results suggest that the effect of calf compressibility on the total pressure of the ACB was less than 5 % for initial mechanical pressures of less than 23 mmHg (3.07 kPa), 24.5 mmHg (3.27 kPa) and 27.5 mmHg (3.67 kPa) at the knee, mid-calf and ankle regions. Generally, the ACB with a specific value of stretch ratio exerted higher mechanical pressure and resulted in higher actuation pressure for calf regions which had smaller sizes. The study in this work suggested that the size and the compressibility of the calf should be taken into account in order to create a sufficiently accurate design of the elastic bandages that are supposed to exert a specific range of compressions.

## Chapter 5.

# Investigation on a soft Grasping Gripper Based on Dielectric Elastomer Actuators

This chapter aims at achieving OBJECTIVE 3 of the thesis: “designing a soft grasping gripper based on DEAs in a cylindrical configuration for potential use to grab delicate objects and collaborate with human counterparts”. The contents of this chapter are adapted from the following publication and may have been modified to comply with the format of this thesis:

Pourazadi S, Bui HT, Menon C. Investigation on a soft grasping gripper based on dielectric elastomer actuators. Smart Materials and Structures. 2018 Dec 10.

### 5.1. Abstract

A novel soft grasping gripper which is based on dielectric elastomer actuators (DEAs) is presented in this chapter. The gripper presents a self-contained and inherently soft approach for grasping objects. A single actuator membrane based on an acrylic elastomer inflates upon application of high electrical voltages. The actuation deformation of the membrane results in a frictional grasp of an underlying object from multiple angles simultaneously. The gripper comprises a pressurized chamber sealed by the cylindrical DEA and relies on the friction force between the DEA membrane and the object. Mathematical analyses are carried out to simulate the actuation deformation of the DEA membrane and to estimate the grasping force with 3 cylindrical objects of different sizes. Experimental results validate the analytical analyses and show up to around 20% of membrane actuation deformation and 2N of grasping forces.

### 5.2. Introduction

Innovative soft robotic systems have been developed at a growing rate with a wide range of applications in aerospace, medical, locomotion and material handling sectors [6], [121]. In this context, the need for novel actuation systems has been identified as conventional actuators are not mechanically compliant and therefore particularly not

suitable for soft devices [2], [122]. Traditionally, gripper designs use rigid hardware with complicated software and algorithms to manipulate all sorts of objects [74]. Besides complicated and tedious algorithms for the efficient and compliant interaction of rigid grippers with unknown objects, handling fragile and delicate objects by these grippers is a huge challenge[60], [69], [123]. Therefore, the development of soft grippers that could comply with unknown geometries is interesting. Recently there are a growing number of researches that focus on developing soft grippers that can handle delicate objects. The tendency is toward grippers with simplified structures and components that are often designed using compliant surfaces[68]. Gripping mechanisms that use compliant surfaces include pneumatic channels embedded in elastomer fingers[69], [70] , hydrostatic skeletons[71], inflatable rubber pockets [72], material jamming[73], [74] and vacuum suction[75]. All of these mechanisms require the gripper to be connected to at least one continuous air pressure line and consume a considerable amount of power per grasp[68].

As mentioned in chapter 2, DEAs has been proposed for the application of soft grasping [39], [60], [76]. However, in this chapter, a different take on DEA-based soft grasping grippers that undergo inflation actuation is introduced. The proposed design is an alternative solution for soft grasping and is not claiming superiority over existing solutions such as pneumatic soft grippers.

In the following section 5.3, the design of the gripper and the used materials are discussed. Also, 2 experimental set-ups are introduced to carry out experiments for the characterization of the designed gripper. In section 5.4, mathematical models are introduced and developed to simulate the behavior of the gripper both in the amount of DEAs deformation and the amount of grasping force applied to an object with a particular dimension. In section 5.5, the results are reported and discussed in details and the mathematical analyses are compared with experimental findings for the proposed soft gripper. Conclusions are followed at the end of the chapter.

## **5.3. Materials and methods**

### **5.3.1. Soft gripper prototype**

The proposed gripper consisted of a hollow cylindrical chamber with 4 circular windows and a cylindrical DEA membrane that was sitting inside the sealed hollow

chamber as shown in Figure 5-1. This design allowed for inflation of the DEA membrane as a result of pressure build-up in the chamber. The DEA was mechanically and electrically inflated using the air pressure inside the chamber and the DEA actuation respectively. The working principle of the gripper actuation was that upon high voltage application to the DEA membrane, the DEA thickness reduced and resulted in the inflation of the membrane. This actuation inflation of the DEA was exploited to create a grasping force to an encompassed object due to frictional contact.

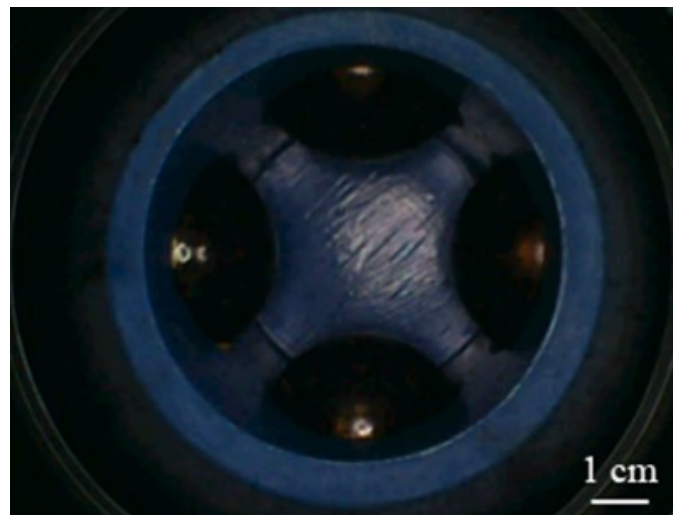
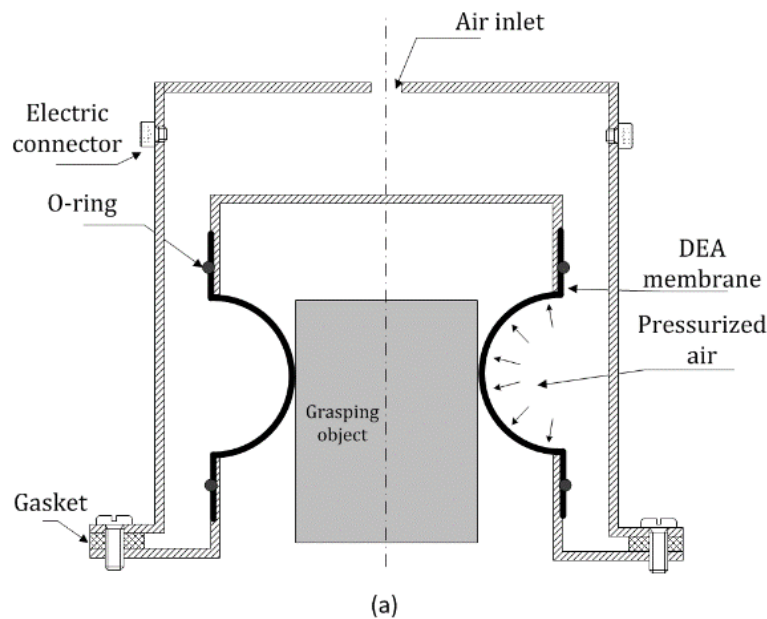


**Figure 5-1. Soft gripper with cylindrical DEA. (a) A cross-sectional view of the soft gripper and (b) view from the bottom.**

Highly stretchable, acrylic VHB™ 4910 adhesive tapes from 3M™ were used as the dielectric membrane for the gripper design since the acrylic-based DEAs usually undergo large deformations which make them suitable for grasping objects with a wider range of dimensions. A two-layer DEA was used in order to increase the amount of grasping force. Two pieces of 18cm X 5cm were cut from the tape and each piece was painted by a mix of carbon black (Vulcan XC-72R) and ethanol with a weight to volume ratio of 20mg to 10 ml to create compliant electrode layers. The painted electrode area was 16cm X 3cm. Small strips of the electrode were painted along each layer to facilitate the attachment of copper tapes to the DEA membrane. In order to improve the mechanical adhesion of the carbon black to the elastomer surface, a layer of 3M VHB- F9473PC film with a thickness of around 350µm was applied on each side of the 2-layer DEA. Next, the two edges of the planar DEA sample were curled and brought together and pressed against each other to form a cylindrical DEA sample with 5.3cm in diameter. The edges of the sample bonded strongly together due to the super adhesiveness of the tape on both sides.

A two-piece hollow cylindrical chamber was prototyped using ABS 3D printing as shown in Figure 5-2. The 3D printed parts were coated by a layer of TC-1614 epoxy (BJB Enterprises, USA) to make the gripper's chamber airtight. The inner part of the chamber had 4 circular windows to facilitate the inflation of the DEA membrane. The cylindrical DEA membrane was pre-stretched and placed on the inner part of the chamber. The cylindrical DEA was pre-stretched equi-biaxially by a stretch ratio of 1.5 in radial and longitudinal directions. Hence the initial thickness was  $\frac{1}{1.5 \times 1.5} = 0.44\text{mm}$  for the dielectric medium of each DEA layer or 0.88mm considering both DEA layers. O-rings were used on the top and bottom of the DEA membrane in order to secure an air-tight placement of the DEA on the inner part. The DEA's copper electrodes were connected to two electrical connectors which were inserted on the opposite sides of the outer part of the chamber. Once the DEA was secured and the electrical connections were established, the outer part of the chamber was placed on top of the inner chamber and screwed together to create an isolated volume. An air inlet was placed in the middle of the upper surface of the outer part of the chamber to allow for even distribution of air while inflating the DEA membrane.

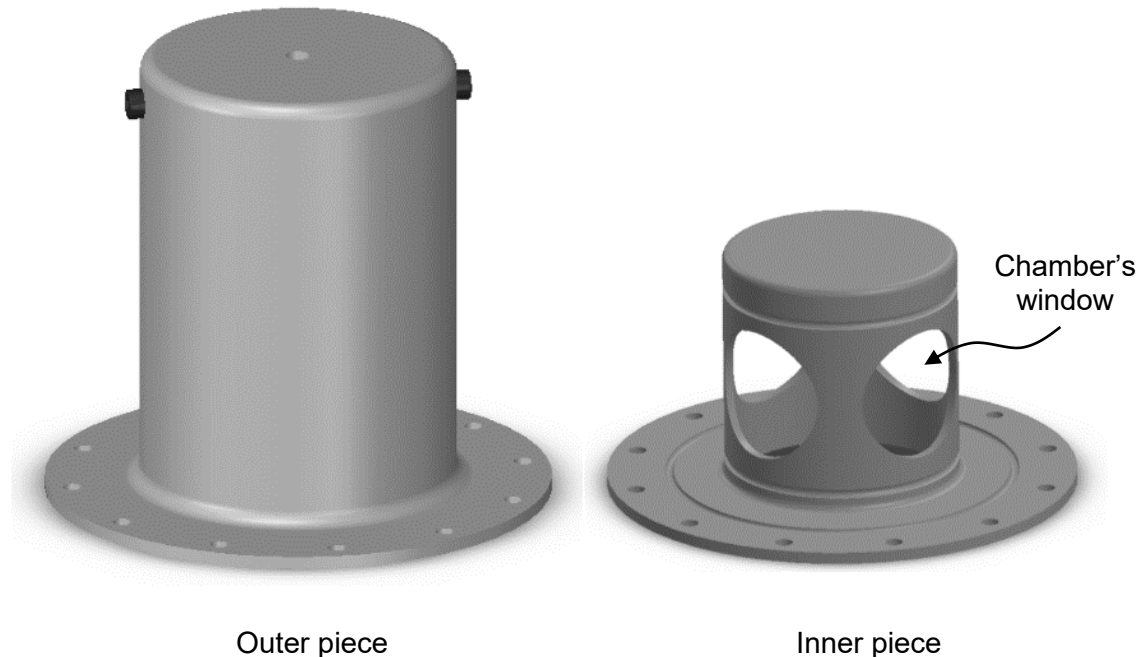


**Figure 5-2. CAD drawing of the two-piece chamber of the gripper**

As the pressure inside the chamber was increased, the free surfaces of the DEA membrane mechanically inflated in the radial direction. Once the DEA was actuated by the application of high voltage, the DEA membrane deformed further in the radial direction due to the Maxwell stress. As shown in Figure 5-1, the inflation of the DEA membrane was exploited to apply grasping forces to objects which were in the opening center of the gripper.

A video file is provided in this link ( IOP SMS journal link address): [stacks.iop.org/SMS/28/035009/mmedia](https://stacks.iop.org/SMS/28/035009/mmedia) to show the performance of the gripper in action. In the video, it is shown that the gripper was able to grasp an object upon DEA actuation, hold the object while a voltage was being applied across the DEA, and release the object quickly as the DEA was discharged. In the presented video, a power supply in the background shows the state of the input voltage and current and indicates the power consumption of the gripper during grasp, hold and release for the gripper. As shown in the video, less than 1W was required to grasp and hold the object while about 4W was required to release the object. Also, once the DEA membrane was activated, a period of about 4 seconds was waited to allow for the current stabilization and optimum grasping force. It took less than 1 second for the gripper to break the grasp and release the object upon DEA discharge.

In order to characterize the proposed gripper, analytical analysis and experiments were carried out to study the DEA deformation and the amount of grasping forces for different parameters of the gripper such as DEA voltage, the pressure inside the chamber, and volume inside the chamber. Two experimental procedures were used to characterize the performance of the gripper and verify the analytical simulations.

### **5.3.2. Experimental set-up 1: Actuator Deformation Measurement set-up**

The goal of experimental procedure 1 was to characterize the gripper's DEA deformation for various chamber pressures, chamber volumes and input voltages. A camera was placed under the gripper's opening to monitor the DEA deformation in real-time. The pressure inside the chamber was monitored using a pressure sensor (MPXV5100GP-ND, NXP Semiconductors, USA). EMCO Q101 amplifier was used to supply high voltage (HV) to the DEA using an adjustable low dc voltage of 1 to 5 volts. The signals from the pressure sensor and a voltage sensor (V1G, EMCO, USA) connected to the HV power supply were acquired using a National Instrument DAQ card. A custom-made LabVIEW program was prepared to acquire and record data from the pressure sensor and the camera with a sampling rate of 11Hz. The video from the camera was image processed frame by frame to identify the DEA membrane deformation. A detachable auxiliary air reservoir was also connected to the gripper's chamber through a valve to increase the volume of the gripper chamber  $V_c$  from 0.6L to 1L.

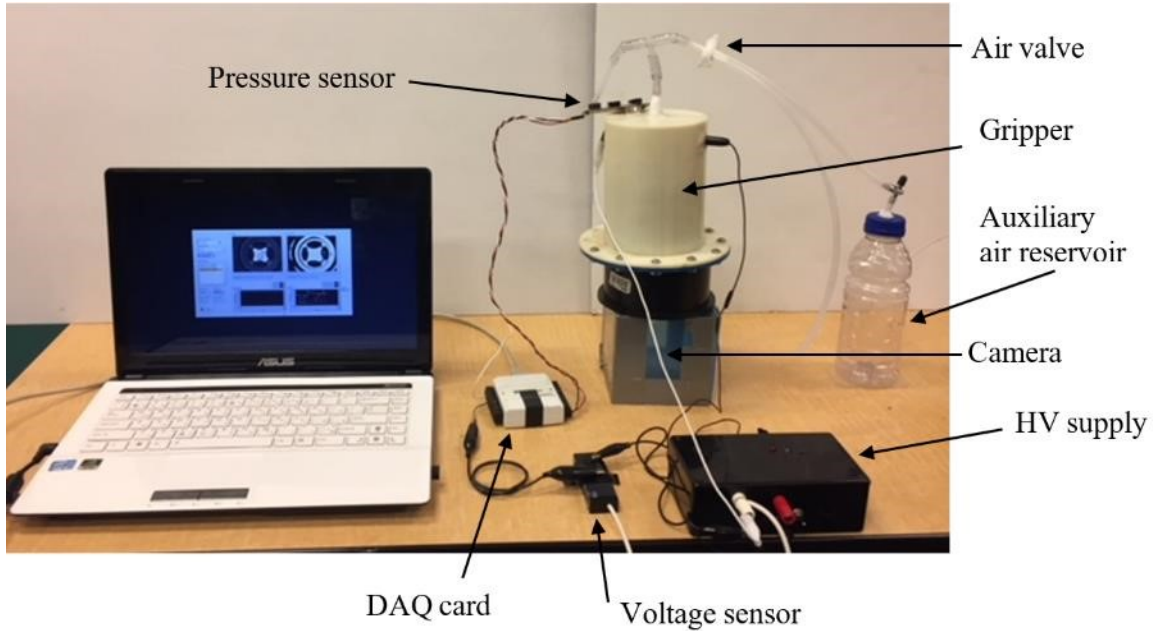


**Figure 5-3. Set-up to characterize the DEA deformation in the proposed gripper.**

A series of experiments were carried out by pressurizing the gripper's chamber to initial pressures of 6.5kPa, 6.9kPa, and 7.1kPa and then actuating the cylindrical DEA up to a voltage of 6.4kV. Upon the actuation of the cylindrical DEA, the DEA thickness reduced, resulting in out of plane deformation of the DEA and reduction in chamber pressure.

### **5.3.3. Experimental set-up 2: Pickup force measurement set-up**

A second experimental set-up was developed to test the gripper's pickup force for various object's diameters and input voltages. The goal of this experiment was to measure the force that the gripper could apply to an object purely based on the actuation of the DEA. The idea was to place the gripper around the object and actuate the DEA membrane with different voltages and then measure the DEA force to the object as the gripper was raised. In this experiment, the object was fixed to the ground via a load cell (Futek, LRF400), while the gripper was attached to a moving vertical linear stage right above the object as shown in Figure 5-4. The linear stage was used to accurately move the gripper up and down along the grasping object with a constant speed. A custom-made LabVIEW program was used to collect and record data from the pressure sensor attached to the gripper chamber, load cell, and the voltage sensor (not shown in the image) with 10Hz of sampling rate.

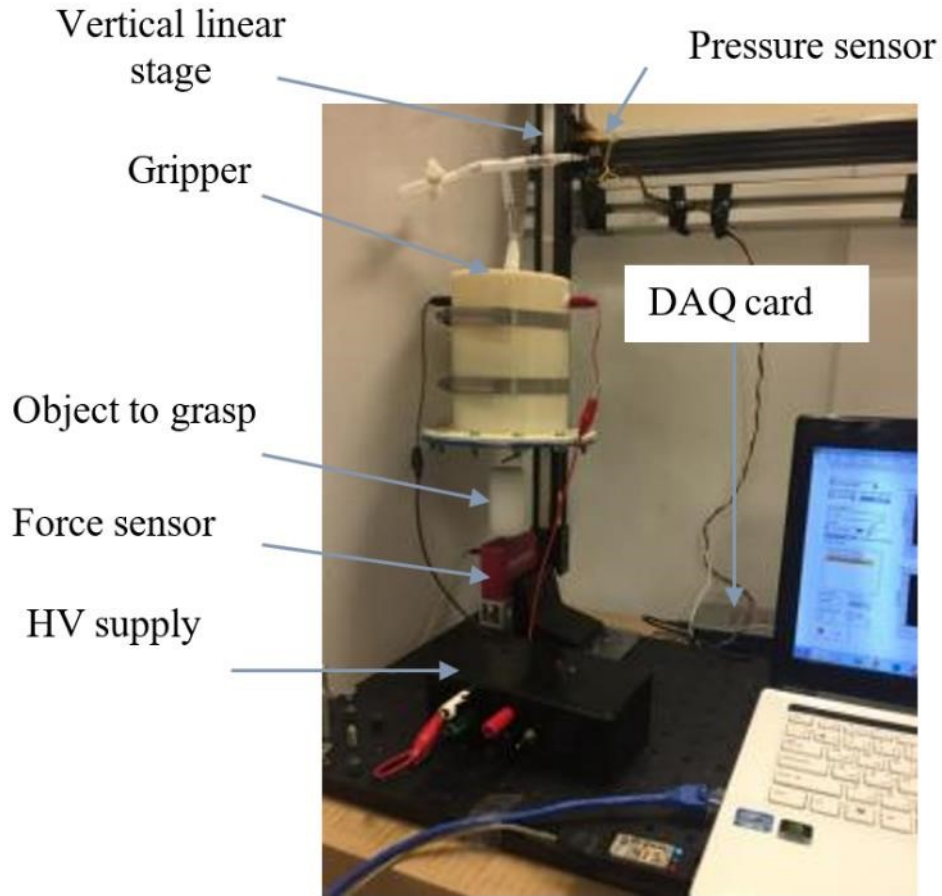


**Figure 5-4. Test set-up for force measurements.**

In order to make sure that the force between the DEA membrane and the object was purely caused by the DEA actuation and not the initial pressurization of the gripper's chamber, a special procedure was carried out during each experiment. Each experiment was started by lowering the gripper using the vertical stage until the gripper was encompassing the object properly. The pressure inside the gripper's chamber was increased such that the DEA membrane was just about to touch the object. In order to verify that the DEA was not in contact with the object, the gripper was raised by the vertical stage while the force measurements by the load cell were monitored. Monitoring a value other than 0 for the load cell meant contact between the DEA and the object. The chamber pressure was adjusted until a just about to touch status was verified. While the gripper was around the object, the DEA was actuated with a voltage. Next, the vertical stage moved the gripper at a constant speed, while the load cell was measuring the pickup force. This procedure was repeated for every voltage and all objects. 3 cylindrical objects with

diameters of 33mm, 42mm, and 48mm were tested for gripper's pickup force measurements.

In the next section, the theory of DEA deformation is discussed to simulate and estimate the behavior of the gripper under similar conditions to the discussed experimental set-ups.

## 5.4. Mathematical analysis

In this section, mathematical models are developed to estimate the applied grasping force of the gripper based on the deformation of the DEA membrane. In literature, static and dynamic modeling of inflated DEA membranes has been investigated widely under different loadings and boundary conditions [124]–[128]. When modeling a DEA's behavior, it is commonly assumed that the elastomer material is incompressible hence:

$$\lambda_1 \lambda_2 \lambda_3 = 1 \quad (1)$$

where  $\lambda_1$ ,  $\lambda_2$ , and  $\lambda_3$  are the stretch ratios in longitudinal, latitude and thickness direction of the elastomer membrane respectively.

Zhu et. al. developed a mathematical methodology based on nonlinear field theory that closely estimated the complex electromechanical behavior of inflated DEAs under different loadings and boundary conditions [125]. A more recent modeling methodology was introduced by Li et.al. which used the same methodology but incorporated the limiting stretch of the VHB 4910 polymer to yield more accurate estimations particularly in large strains [129]. To consider polymer stiffening of VHB 4910 a Gent model was used to represent the free energy of the membrane material:

$$W = -\frac{\mu J_{lim}}{2} \log \left( 1 - \frac{\lambda_1^2 + \lambda_2^2 + \lambda_3^2 - 3}{J_{lim}} \right). \quad (2)$$

In the proposed gripper design, the DEA underwent two modes of deformation. First, the membrane was inflated due to the increased pressure inside the chamber during the absence of voltage, second, the DEA membrane deformed due to the application of voltage. To model the electromechanical behavior of the DEA membrane, the following stress-stretch relations were used:

$$\sigma_1 + \varepsilon E^2 = \lambda_1 \frac{\partial W}{\partial \lambda_1}; \quad (3)$$

$$\sigma_2 + \varepsilon E^2 = \lambda_2 \frac{\partial W}{\partial \lambda_2} \quad (4)$$

where  $\sigma_1$  and  $\sigma_2$  are stresses in the membrane in longitudinal and latitudinal directions respectively caused by the chamber pressure,  $\varepsilon$  is the permittivity of elastomer and  $E$  is the electric field across the thickness of the membrane. The electric field is defined as the ratio of the voltage applied to the DEA ( $\phi$ ) over the elastomer's thickness ( $h$ );  $E = \phi/h$ . Equations 3 and 4 simply state that, in the membrane, the change in free energy with respect to stretch in a direction is directly proportional to the stress in that direction where the stress is the combination of stress from the air pressure and electric field's Maxwell stress.

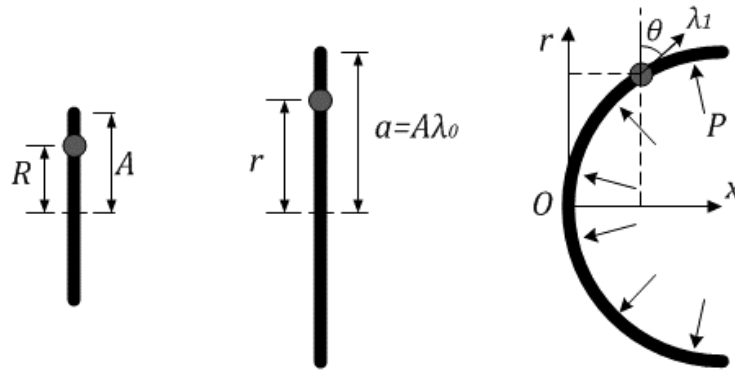


**Figure 5-5. Side view of the membrane at a chamber's window. (a) Membrane at relaxed state; (b) membrane at pre-stretch state; (c) membrane at pressurized and/or actuated state.**

Let us assume a cross-sectional view of an inflating part of the membrane as shown in Figure 5-5. Assuming  $R$  is the radius of a circular pattern in the undeformed membrane, the functions  $r(R)$ ,  $x(R)$ ,  $\theta(R)$ , and  $\lambda_1(R)$  define the deformation and geometry of the membrane after deformation. The notions  $r$ ,  $x$ ,  $\theta$ , and  $\lambda_1$  are shown in Figure 5-5 and they represent the radius, length, slope angle and longitudinal stretch in the deformed membrane. As presented in [129], the following 4 differential equations describe the deformation of the membrane:

$$\frac{\partial x}{\partial R} = \lambda_1 \sin \theta; \quad (5)$$

$$\frac{\partial r}{\partial R} = \lambda_1 \cos \theta; \quad (6)$$

$$\frac{\partial \theta}{\partial R} = -\frac{\sigma_2 \lambda_1}{\sigma_1 \lambda_2 R} \sin \theta + \frac{\lambda_1^2 \lambda_2 P}{\sigma_1 H}; \quad (7)$$

$$\frac{\partial \lambda_1}{\partial R} = \frac{1}{R \frac{\partial(\sigma_1/\lambda_1)}{\partial \lambda_1}} \left( \frac{\sigma_2}{\lambda_2} \cos(\theta) - \frac{\sigma_1}{\lambda_1} - \frac{\partial(\sigma_1/\lambda_1)}{\partial \lambda_2} (\lambda_1 \cos \theta - \lambda_2) \right); \quad (8)$$

where  $\lambda_1 = \sqrt{\left(\frac{\partial r}{\partial R}\right)^2 + \left(\frac{\partial x}{\partial R}\right)^2}$ ,  $\lambda_2 = \frac{r}{R}$ ,  $P$  is the pressure inside the chamber, and  $H$  is the thickness of the undeformed membrane or  $H = h\lambda_1\lambda_2$ . The  $\sigma_1$  and  $\sigma_2$  in (7) and (8), could be substituted with (3) and (4). Solving the coupled differential (5) to (8) will provide the DEA's deformation at equilibrium state for a given pressure  $P$  and voltage  $\phi$ . The proposed gripper in this chapter had 4 inflating windows, thus once the DEA inflation was simulated at one chamber's window, the overall volume of the chamber was obtained using the following integration [125], [129]:

$$V = V_c + 4\left(-\pi \int_0^A r^2 \frac{dx}{dR} dR\right). \quad (9)$$

Given the origin of the coordinate system at the apex of the membrane (as shown in Figure 5-5) the boundary conditions were set to  $r(0) = 0$ ;  $x(0) = 0$ ;  $r(A) = A\lambda_0$ ;  $\theta(0)=0$  where  $A$  is the undeformed DEA electrode width and  $\lambda_0$  is the pre-stretch of the DEA membrane.

In order to solve for the deformation of the DEA membrane, equations (5)-(8) subjected to the boundary conditions were solved using MATLAB's ode 113 and shooting method. Li et. al. discussed that, for relatively large chamber volumes, at a given pressure and voltage, there are multiple solutions for the set of differential equations [129]. However, in this thesis, since the chamber's volume was relatively small, snap-through instability was not relevant and only single solutions were obtained for the differential equations.

In order to obtain the Gent model parameters  $\mu$  and  $J_{lim}$  for the double layer DEA membrane of this chapter, which had thin insulating layers over its electrodes, the optimization toolbox in MATLAB was used. The set of data from experimental set-up 1, where the gripper chamber was pressurized while monitoring the DEA's deformation, was

used to obtain curves for the measured DEA climax deformation versus different pressures. Genetic algorithm was used to search for parameters  $\mu$  and  $J_{lim}$  in order to fit an optimum simulated DEA deformation profile on the experimental curves. Parameters  $\mu$  and  $J_{lim}$  were found to be 90kPa and 270 respectively.

Figure 5-6 shows a simulation of a DEA's deformation at one of the gripper's windows at pressure 6kPa and voltage 6kV. Figure 5-7 shows the pressure-volume curve inside the chamber for different voltages across the DEA. In Figure 5-7, pressure-volume curves are illustrated for the two chamber volumes  $V_c$ . The curves with no markers show characteristics of a gripper chamber with 1L volume whereas the curves with square markers demonstrate a gripper chamber with 0.6 L volume.

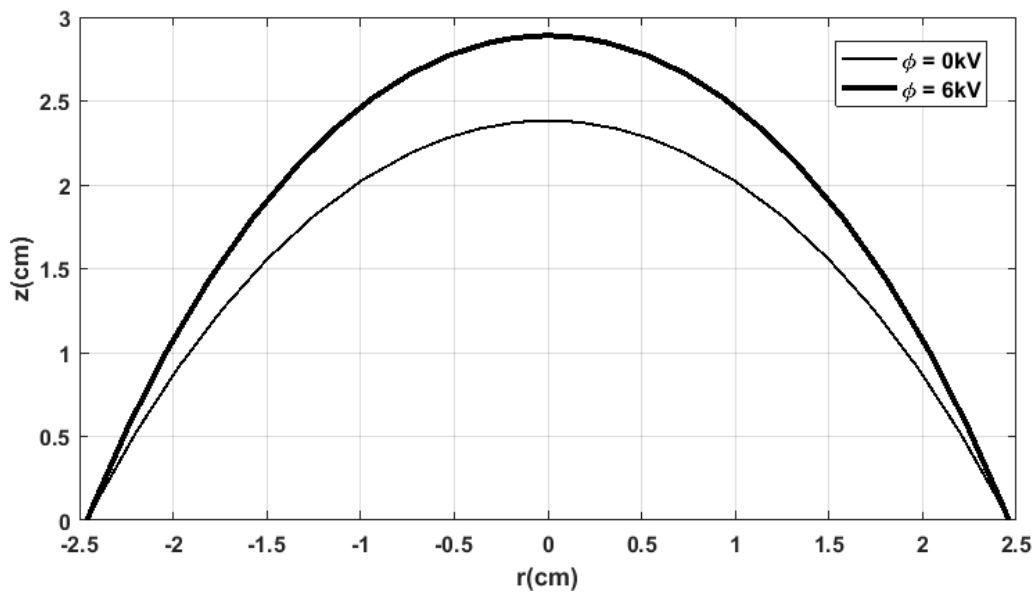


**Figure 5-6. DEA deformation profile at a single window of the gripper for an initial chamber pressure of  $P=6\text{kPa}$ .**

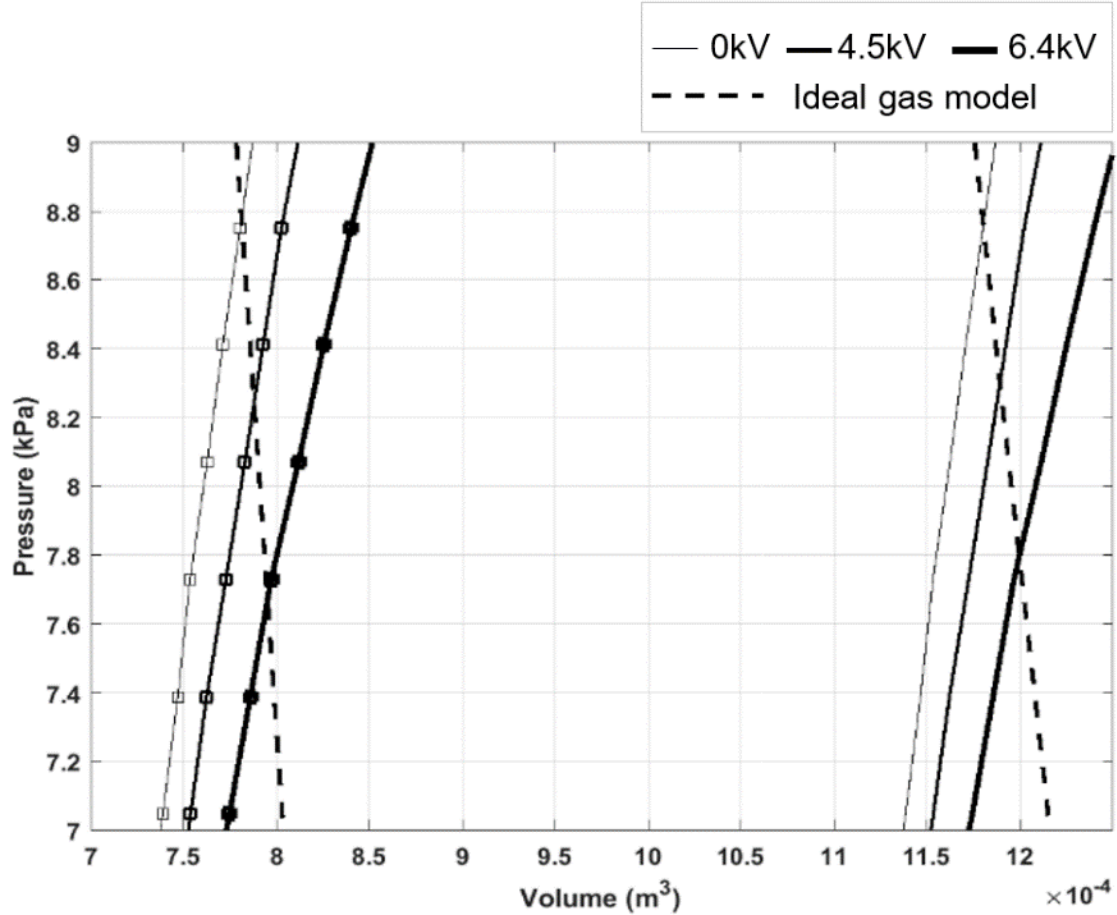


**Figure 5-7. Pressure-volume profile of the gripper's chamber and air.**

It should be noted that  $\lambda_0$  is a key parameter that affects the performance and actuation deformation of the DEA membrane as also discussed in [125]. The model presented in the manuscript could be used to find the optimum pre-stretch value by solving an optimization problem for  $\lambda_0$  using methods such as genetic algorithm. The readers are referred to reference [125] for further discussion on the effect of pre-stretch on the deformation of such inflating membranes.

During experiments with the gripper, air was introduced into the gripper's chamber, inflating the DEA membrane and increasing the air volume and pressure inside the chamber to  $V_0$  and  $P_0$ . Then, the chamber's air inlet was closed and the DEA was actuated resulting in an increase in volume to  $V_a$  and a decrease in pressure to  $P_a$ . The new pressure-volume state of the chamber could be obtained by assuming an ideal gas model and a constant temperature for the air inside the chamber:

$$P_0 \cdot V_0 = P_a \cdot V_a. \quad (10)$$

The ideal gas curve for air is drawn by dashed lines in Figure 5-7 for  $P_0=8.75\text{kPa}$ . The values for chamber pressure and volume at a given voltage is obtained at the intersection point of the ideal gas curve and the chamber's curve for that voltage. For example, for  $V_c=1\text{L}$ , after actuation with voltage  $\phi=6.4\text{ kV}$ , the volume and pressure inside the chamber were calculated to be  $1.2\text{L}$  and  $7.8\text{kPa}$  respectively. Once the pressure drop was identified, the deformation profile of the DEA membrane was obtained by solving for equations (5) to (8) again and using the new pressure for the corresponding voltage. Equation 10 and Figure 5-7 show that providing a larger volume for the chamber (larger  $V_c$ ) resulted in smaller pressure drops upon DEA actuation.

The proposed gripper applied a grasping force to an object due to the actuation inflation of the DEA membrane and produced frictional contact between the object and the DEA membrane. Assuming static friction, the friction force, in turn, depending on the friction coefficient  $\mu_s$  and the contact area  $A_c$  between the object and the membrane, and the pressure inside the chamber  $P$ :

$$F = 4 \mu_s \cdot P A_c. \quad (11)$$

It was assumed that the membrane formed a flat circular pattern after actuation inflation and coming into contact with the object, as shown in Figure 5-8. The contact area  $A_c$  was calculated by considering the actuation profile of the membrane and the dimension of the object. The point in the  $x$ -direction at which the actuated membrane profile and the object intersected was obtained and the membrane's corresponding radius  $r_c$  was used to calculate the contact area i.e.  $A_c = \pi r_c^2$ . The new volume of the chamber could be updated by considering the contact radius in the lower bound of the integration in (9).

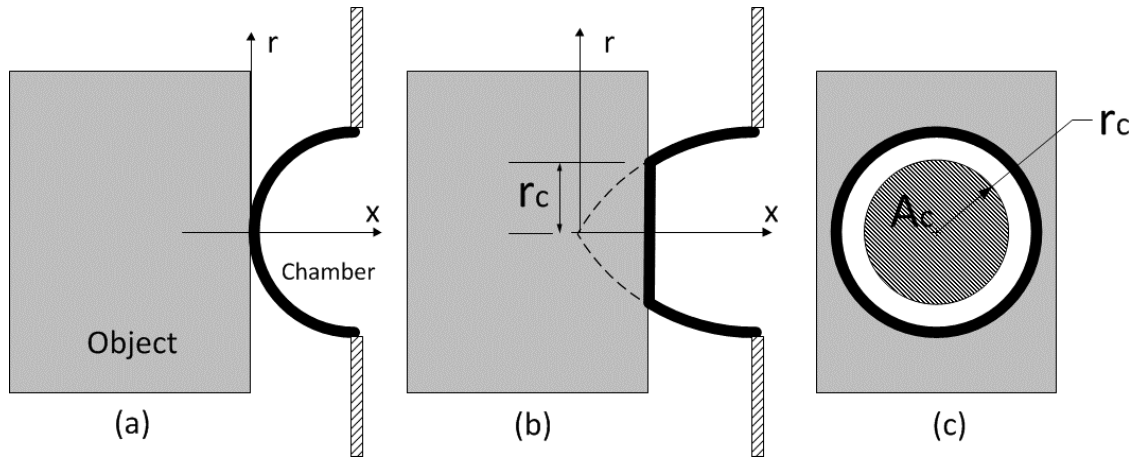


**Figure 5-8. DEA membrane and object contact at a single window of the gripper.**

Figure 5-9, shows a simulation of grasping force versus various actuation voltages by using (11) and the calculated DEA membrane deformation profile. For Figure 5-9, it was assumed that  $V_c=1L$ , the initial pressure inside the chamber was raised to  $P_0=6kPa$  and a cylindrical object with 3.2cm in diameter was subject to grasping. For the DEA membrane of the gripper in this chapter,  $\mu_s$  was obtained to be 0.35 by doing simple traction tests between the object and the membrane.

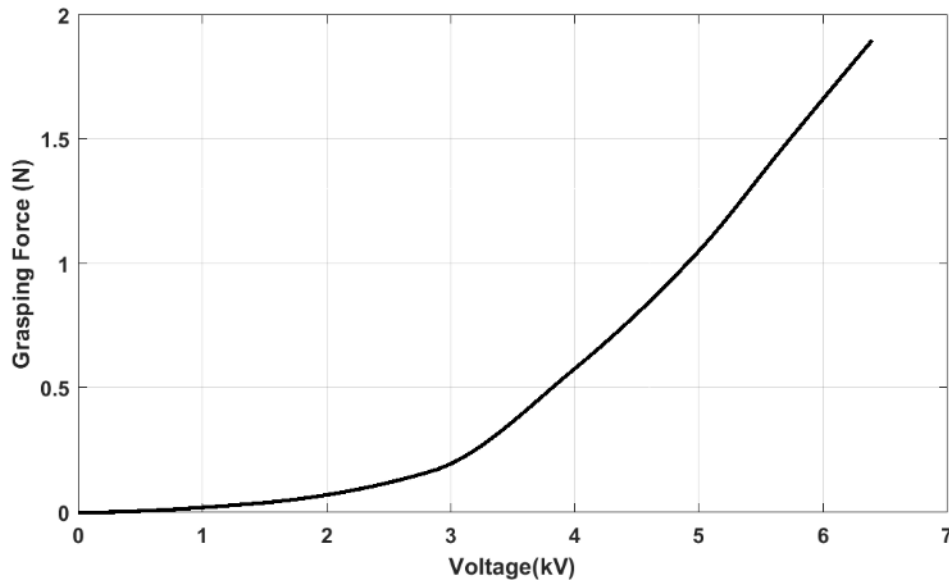


**Figure 5-9. Simulation results of the gripper's grasping force to an object of diameter 3.2cm with  $V_c=1L$  and  $P_0=6kPa$ .**

## 5.5. Results and Discussion

In order to characterize the gripper and to verify the analytical simulations, experiments were carried out using set-up 1 and set-up 2. Set-up 1 was aiming at monitoring the DEA membrane deformation profile while applying various pressures and voltages to the gripper. Experiments were carried out using 2 different chamber volumes of  $V_{C1}=0.6$  L and  $V_{C2}=1$  L. Air was introduced into the chamber to inflate the DEA membranes and raise the pressure inside the chamber to a certain pressure while monitoring DEA deformation by the camera. 3 pressures were tested in this chapter  $P_{01}=6.5$  kPa (0.95psi),  $P_{02}=6.9$  kPa (1.0psi), and  $P_{03}=7.1$  kPa (1.03psi). Once the membrane was stabilized, the membrane was actuated using high voltages up to 6.4kV. Figure 5-10 shows a sample of the acquired data from set-up 1. It should be mentioned that the source of the noise in the DEA apex graph was in the method for apex measurements. As it is discussed in section 5.3.2, the DEA deformation is measured using real-time processing of the images captured from the camera under the gripper. The noise is created due to the camera-captured image variations at the pixel level. Once the voltage across the DEA was increased, the DEA deformation quickly increased at first and then underwent a gradual increase. The gradual increase in deformation was more apparent in larger voltages. This dynamic observation is typical for acrylic elastomers due to their viscoelastic properties as discussed by literature [55]. The same behavior was observed upon removal of the voltage around time  $t=275$ s. The DEA quickly deflated at first and then underwent gradual deflation over time.

Referring to the pressure curve in Figure 5-10, at time  $T=104$ s and  $T=300$ s, a pressure of 0.918 psi was corresponding with an apex deformation of 1.69cm. Thus, after a time span of about 200 seconds the pressure and volume relation seemed unchanged. Therefore, no considerable leakage was observed in the gripper chamber either through the 3D-printed body or through the VHB elastomer.

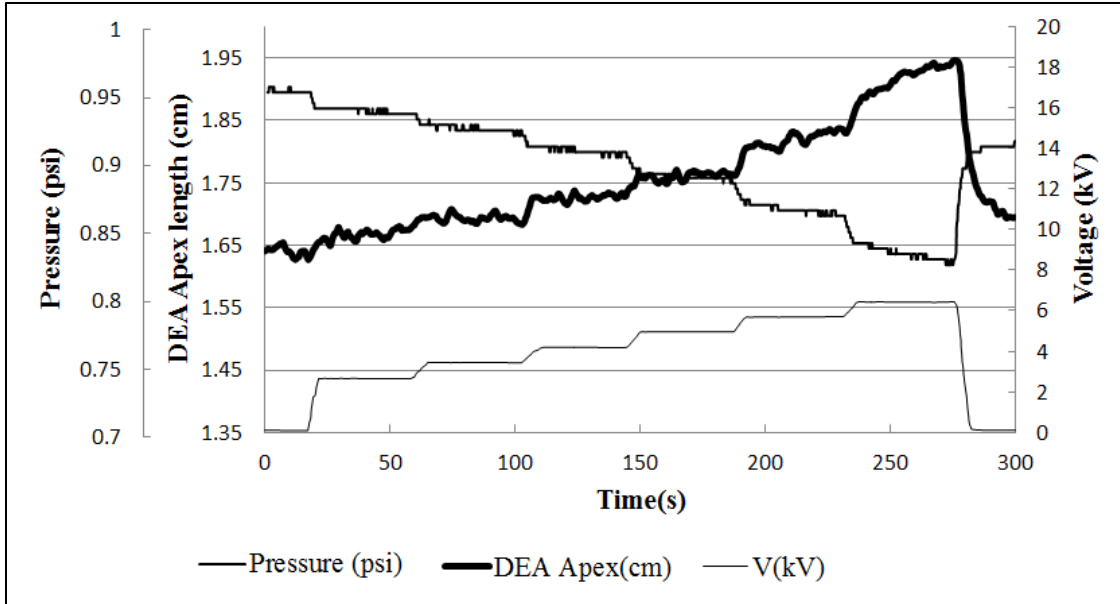


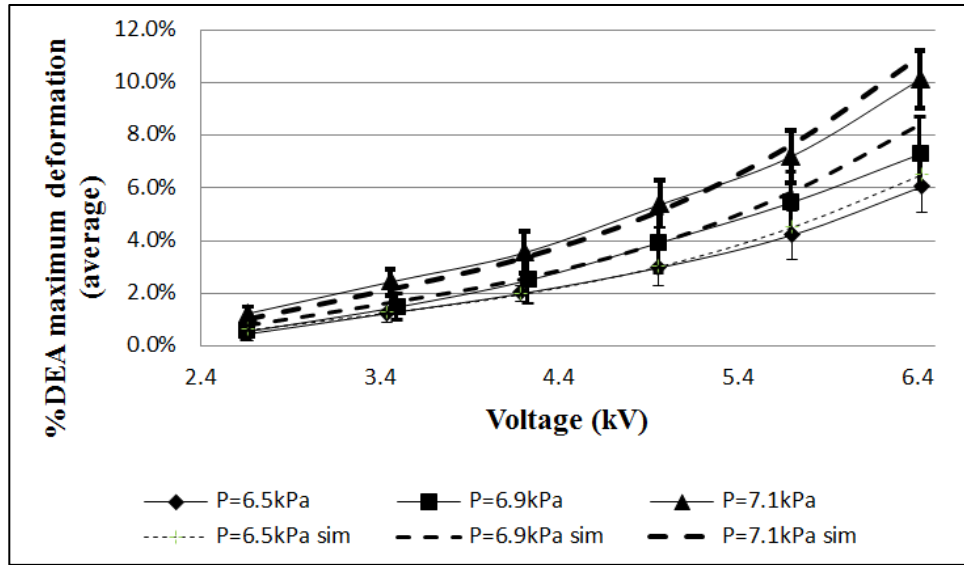
**Figure 5-10. Sample data acquired from set-up 1.**

The experimental and analytical curves of the DEA maximum deformation percentage for different voltages across the DEA membrane are shown in Figure 5-11. Figure 5-11(a) shows the results for a gripper chamber with a reservoir volume of  $V_{c1}=0.6\text{L}$  while Figure 5-11(b) shows the results for a reservoir volume of  $V_{c2}=1\text{L}$ . At a chamber pressure of  $7.1\text{kPa}$ , the percentage of DEA apex deformation was at  $10.1\%\pm 1.1\%$  for  $V_{c1}=0.6\text{L}$  compared to the deformation of  $19.6\%\pm 1.7\%$  for  $V_{c2}=1\text{L}$ . As it was also discussed in the analytical section previously, Figure 5-11 and Figure 5-12 confirm that a larger volume in the gripper's reservoir resulted in a larger DEA deformation. The reason for this behavior was that a larger chamber volume allowed for a smaller chamber pressure drop and hence an elevated DEA membrane deformation resulted. For the tested chamber volumes, the increase in initial chamber pressure resulted in more DEA actuation deformation. This increase in actuation deformation is partially due to the thinner DEA membranes. The larger the pressure, the larger was the passive inflation of the DEA and hence the thinner was the DEA membrane before actuation. Thinner DEA membrane resulted in stronger Maxwell stress and a larger actuation deformation.

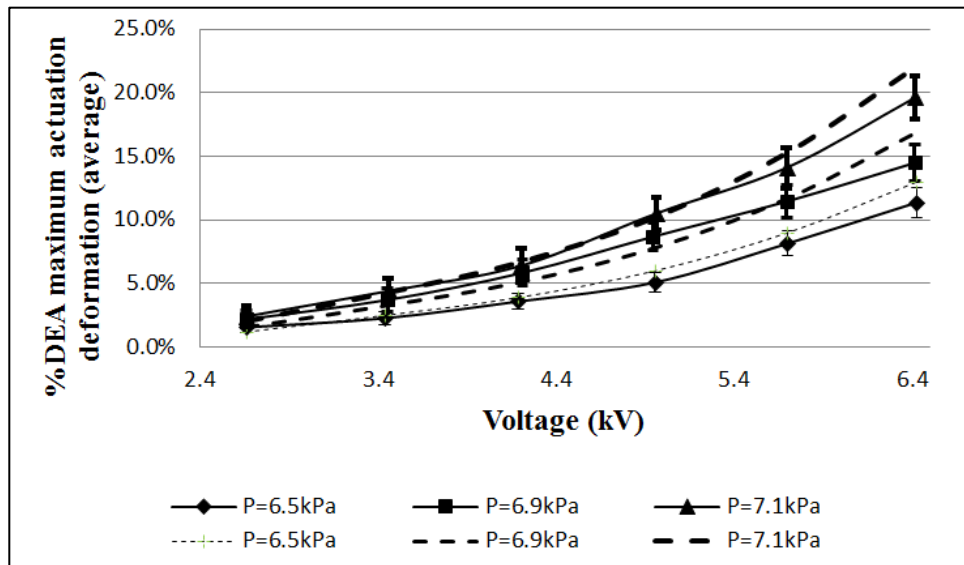
To investigate if there is an actuation gain due to the increase in pressure, the curves in Figure 5-11, were plotted for the electric field across the DEA membrane in Figure 5-12. The thickness in the experimental results was estimated using the following formula [50]:

$$h = \frac{a^2 H}{\lambda_0^2 (x(A)^2 + a^2)}. \quad (12)$$

Curves in Figure 5-12(a) and Figure 5-12(b) demonstrate that the larger chamber pressures resulted in larger actuation deformations. The analytical simulations in Figure 5-11 and Figure 5-12, closely predicted the experimental observations with a maximum error of 12%. However, generally, the simulated results were within the error range of each experimental data point. The mismatch between the experimental and simulations results might be due to a number of reasons including a slight error in the DEA membrane material model and geometrical simplifications.



(a)

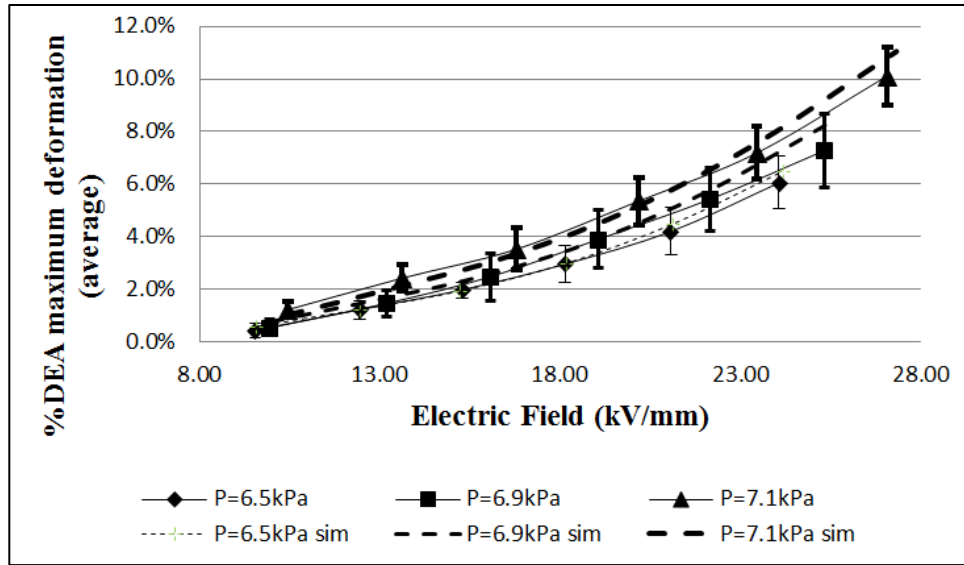


(b)

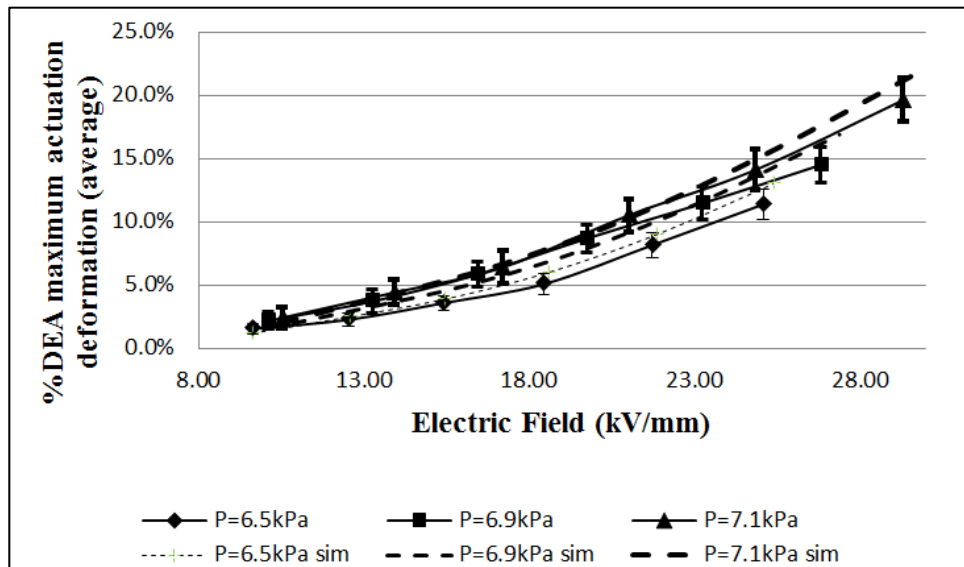
**Figure 5-11. DEA actuation deformation at the apex for various applied voltages and chamber volumes of a)  $V_{c1}=0.6L$ , and b)  $V_{c2}=1L$ .**

Since a reservoir volume of  $V_{c2}= 1L$  yielded more actuation deformation, this volume was used to perform the grasping force experiments of test set-up 2. Grasping experiments were carried out on 3 cylindrical objects with diameters of 3.3cm (small), 4.2cm (medium) and 4.8cm (large). Each experiment was started by lowering the gripper using the vertical stage to encompass the object. The procedure that was explained in section 5.3.3 was followed to assure that the grasping force was solely due to the actuation deformation of the DEA and not the passive inflation. This procedure was repeated for

various voltages and all test objects. Each experiment was repeated for 3 trials to obtain a statistical range of performance for the gripper. The pressure inside the chamber was 6.27kPa, 5.92kPa, and 4.1kPa for the small, medium, and large objects respectively. Figure 5-13 shows one of the trial experiments on grasping the small object. While lifting the gripper over the fixed object, the stick-slip phenomenon was observed [130]. In other words, the force profile at each voltage comprised of 3 stages. First, as the linear stage lifted the gripper with a constant speed, the soft membrane did not move relative to the object and a static friction was observed. Second, as the linear stage further lifted the gripper, the soft membrane slipped on the object and dynamic friction was observed. Third, as the gripper was lifted even further, the membrane lost complete contact with the object and no friction force was observed. Since static friction is much higher than dynamic friction, the force profile spiked to a maximum value at first and then was reduced with a steep slope until the membrane lost contact with the object and zero force was measured. Referring to Figure 5-13, the maximum force at each force spike indicated the amount of grasping force because the grasping force was a result of static friction force between the membrane and the object as it was also discussed for equation (11). Also, in Figure 5-13, as the voltage increased the amount of grasping force increased despite increased pressure drop in the gripper's chamber This increase in grasping force was due to the increased contact area between the membrane and the object as a result of larger actuation inflation.

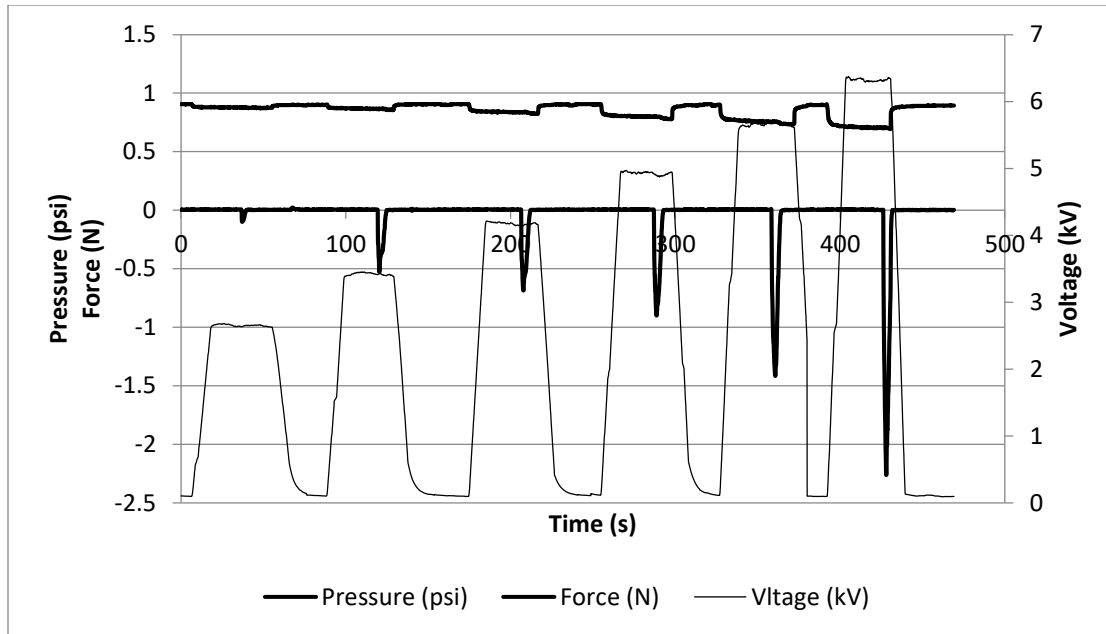


(a)



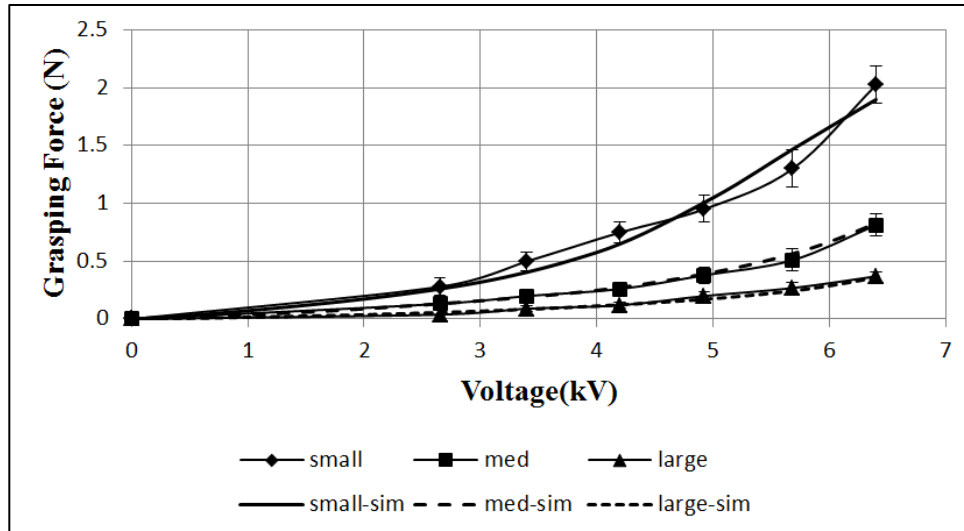
(b)

Figure 5-12. DEA actuation deformation at the apex for various electric fields and chamber volumes of a)  $V_{c1} = 0.6L$ , and b)  $V_{c2} = 1L$ .

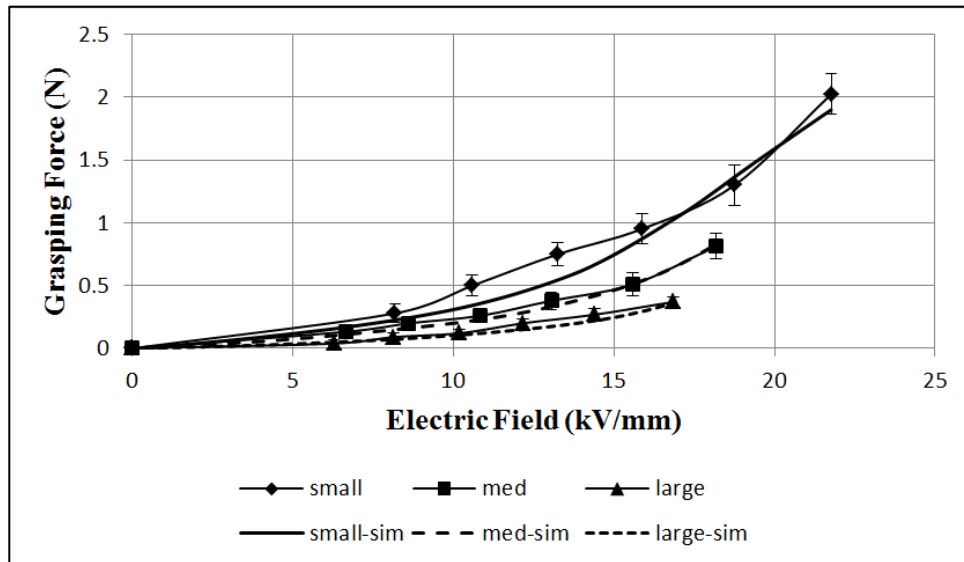


**Figure 5-13. Sample experimental data on the small (3.3cm diameter) object from test set-up 2.**

Figure 5-14(a) shows the results of the gripper's grasping force versus applied voltage to the DEA for different object sizes. Since the initial chamber pressure and hence the passive inflation is different for each object, the thickness of the membrane is different for each object size. In order to assess the amount of grasping force versus an equal amount of applied electrostatic force, the curves in Figure 5-14(a) were plotted against the electric field in Figure 5-14(b). Since the DEA deformations were not measured during force experiments, the membrane thickness could not be measured directly for the experimental data points. Therefore, the mathematical analyses in section 5.4 were used to estimate the membrane thickness under different chamber pressures. This method was assumed to be valid because the mathematical analyses were verified for simulating DEA deformations in Figure 5-11 and Figure 5-12. In Figure 5-14(a) and Figure 5-14(b), again the analytical simulations were able to predict the experimental results within the error range of each experimental data point. It was shown that for an object of 3.3cm diameter, the proposed soft gripper was able to apply up to around 2N of actuation grasping force with the application of a maximum of 6.4kV. For larger objects, smaller DEA inflations and hence smaller pressures inside the gripper's chamber was required. Thus, for larger objects smaller actuation grasping forces were observed as it was predicted by the analytical simulations.



(a)



(b)

**Figure 5-14. Gripper's grasping force for different object sizes. a) Grasping force versus the applied voltage. b) Grasping force versus the applied electric field.**

In real-life applications, the passive inflation of the membrane should be chosen carefully. The passive inflation might be less than the diameter of the object to prevent contact and interference with the object before grasping. Thus, the grasping force at a given voltage would be smaller than the characterized forces in this chapter because a part of the membrane actuation would be used to bring the membrane in contact with the object.

## 5.6. Conclusion

There is a growing need for soft robotic manipulators to efficiently and successfully handle soft and delicate target objects such as fruits, plants and live tissue. Dielectric elastomer actuators (DEAs), present interesting properties that make them suitable for potential applications of item manipulations and soft grasping.

In this chapter, a novel design of a DEA-based soft gripper was proposed and prototyped to investigate the potential application of DEAs for soft grasping and also analyze the performance of such grippers. The proposed gripper consisted of a DEA membrane that was inflated passively by initial air pressure and actively by applying actuation voltage to the DEA. The inflation of the DEA membrane was exploited to apply grasping force on objects in the opening of the gripper.

Two test set-ups were prepared to perform characterization experimentation on the gripper. Experiments were aimed at characterizing the gripper in the amount of DEA deformation and the amount of grasping force it could apply to a certain object. Developed mathematical formulations were used to successfully simulate the behavior of the DEA membrane within the gripper's boundary conditions. Analytical simulations successfully predicted the experimental results and were within the error range of the experimental data points.

It was discussed that the passive inflating pressure and the reservoir volume were the two adjustable parameters that could impact the DEA actuation. For a gripper reservoir volume of 1L and inflating pressures of around 7kPa, actuation deformations of up to around 20% were reported for the DEA membrane of the designed gripper. It was shown that the designed gripper was able to apply up to around 2N of grasping force for cylindrical objects dimensioning from 3.2 to 4.2cm in diameter. The amount of applied force was larger in smaller diameter objects due to the larger inflating pressure for smaller objects. The achieved grasping force of 2N is comparable with other proposed soft grippers based on DEAs. [39], [76] achieved forces of less than 2.4mN while [60] achieved forces of around 3.5N from both electrostatic bending and electroadhesion forces. In comparison, soft pneumatic grippers are capable of applying forces larger than 100N [73], however, they require large pressures (>300kPa) and often require relatively large power consumption (>90W) to operate the pneumatic pumps and airlines [68]. It should be noted

that the main advantage of the proposed gripper is not on the magnitude of grasping forces but rather on removing the need for a pneumatic pump for the purpose of actuation and grasping.

It was shown that larger chamber volumes resulted in larger DEA deformation due to smaller air pressure drop inside the chamber. This observation was in line with previous studies [126], [129]. For future work, larger reservoir volumes could be utilized to exploit the snap-through instability in the DEA membrane and improve the actuation deformation and the amount of applied grasping forces.

## **5.7. Limitations**

While the proposed technology presented a potential alternative solution for soft grasping, there are several limitations and challenges that need to be addressed in future studies. The initial pressure inside the chamber should be carefully adjusted off-line to cause an opening similar to the dimensions of the grasping object because the range of the DEA membrane deformation is limited. This drawback makes this design less desirable for applications where the size of the grasping object would be variable. However, snap-through instability could be used in future designs to increase the range of DEA actuation deformation and the amount of applied grasping forces. Another way to improve this drawback is to connect the gripper chamber to a pressurized reservoir via an electronic 3-way air valve to control the pressure inside the gripper chamber (no pumps required). The air valve could connect the gripper to either the compressed air reservoir or the atmosphere. The reservoir could be configured to pressurize the gripper chamber in case more pressure is required (smaller opening in the gripper) or to compensate for a possible leakage inside the chamber. The air valve could connect the gripper chamber to the atmosphere in case less pressure is required inside the chamber (larger opening).

Another improving aspect for future studies is to enhance the actuation speed of the DEA membrane both during grasp and release. An optimal controller could be designed to energize the DEA faster and decrease the required time to reach a stable voltage across the DEA. Also, other materials, such as silicone elastomers, potentially could be used to decrease the response time of the membrane and increase the speed of actuation deformations.

## Chapter 6.

# Electrical Safety of DEAs in Proximity to the Human Body

This chapter aims at achieving OBJECTIVE 4 of the thesis: “investigating the electrical safety of DEAs in applications where a DEA, particularly in planar and cylindrical configurations, is operated in proximity to the human body which may be the case either for DEA-based compression bandages (OBJECTIVE 2) and soft grasping grippers (OBJECTIVE 3)”. The contents of this chapter are adapted from the following publication and may have been modified to comply with the format of this thesis:

Pourazadi S., Shagerdmootaab A, Chan H, Moallem M, Menon C. On the electrical safety of dielectric elastomer actuators in proximity to the human body. *Smart Materials and Structures*. 2017 Oct 3;26(11):115007.

### 6.1. Abstract

Novel devices based on the use of dielectric elastomer actuators (DEA) have been proposed for a large variety of different applications. In many of these applications, DEAs are envisioned to be in direct or close proximity to the human body. Since DEAs usually require high voltage for their actuation, the safety of individuals operating or using these devices should be ensured. In this chapter, safety standards based on safe limits for electrical discharge are investigated. Flat and cylindrical DEA configurations, which are generally considered as the building blocks for the design of DEA-based systems, are investigated in detail. Relevant elements and factors that affect the electrical discharge of DEA devices are analyzed and guidelines to design DEA-based devices that are not of harm for humans are provided. The performed analyses are experimentally validated using flat DEA samples. The safety requirements that should be considered when wrapping DEAs around the body (specifically the legs) are also briefly investigated to provide a practical example of interest for the biomedical community.

## 6.2. Introduction

As mentioned throughout this thesis, a particularly interesting application of DEAs is wearable devices and collaborative robots. In these applications, DEAs are envisioned to be operated while being in close proximity or even in contact with the human body. The proper design of DEAs to ensure electrical safety is therefore of paramount relevance, especially considering that DEAs can store charges and are generally activated by using high direct current (DC) and alternating current (AC) voltages (generally higher than 1 kV), which could pose a serious threat to the user if discharged to the body.

In the following section, relevant safety standards and criteria are discussed to provide a conservative safe range for electrical discharge factors. Subsequently, a simplified electrical model of a system including a DEA and a human body is considered to introduce relationships between the DEA circuit's electrical parameters and the safety criteria factors. In the subsequent section, three possible dangerous electrical discharge scenarios are discussed and geometrical design constraints that DEA should meet to ensure safety is identified. A design procedure to ensure safety is proposed. Predictions made through analytics are experimentally validated through tests performed with a flat DEA. Subsequently, a case study of the soft DEA-based bandage of chapter 3 is discussed to present a practical example of how the proposed safe design procedure can be implemented. This case study shows how the proposed procedure can be used to ensure electrical safety when designing soft, DEA-based devices such as wearable garments and exosuits. Conclusions are drawn at the end of this manuscript.

## 6.3. Safety standards

Underwriters Laboratories (UL) and International Electrotechnical Commission (IEC) provide safety standards that are used when verifying the safety of consumer electronics [79]. These standards are widely used to verify the safety of DC and AC operated electronics. Usually, the relationship between amplitude and the duration of current passing through the body is important in designing the safety features of many electronic systems [79]. Figure 6-1 reproduces the curves that identify this relationship defined by UL and IEC in a log scale for current exposure durations from 0.1ms to 10s [79].

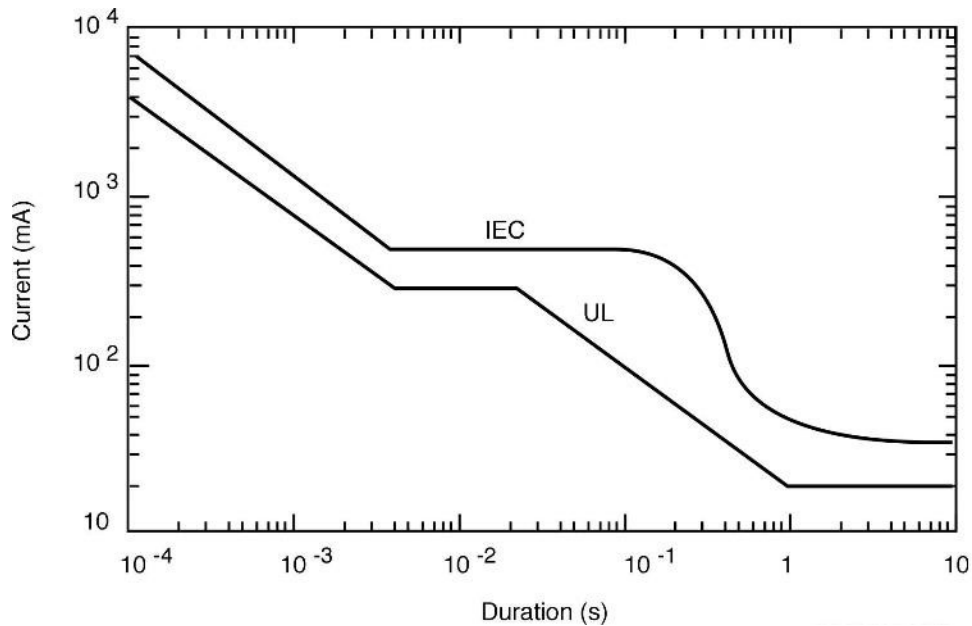


**Figure 6-1. The UL and IEC standard curves for safe limits of amplitude versus current durations. The regions below the curves are safe. Reproduced with permission [79].**

These curves consider AC electrical signals having 50/60 Hz frequency and are proposed to provide the lowest probability of ventricular fibrillation occurrence [79]. The vertical axis represents the RMS value for the current waveforms. The IEC standard suggests that the safe thresholds for DC signals are higher comparing to AC signals but converge to AC threshold for signal durations less than 10ms [131]. Also, Cadick *et al.* [132] suggest that the safe limits for DC currents are similar to those of AC currents with frequencies less than 100Hz. Thus, curves in Figure 6-1 represent a conservative safe limit for both DC and AC when the frequency of the current is less than 100Hz. Since the UL criterion provides a stricter threshold than the IEC, the UL safety limits are considered in this work.

A few clarifications are in order. First, the discharge current amplitude and duration must be below the UL thresholds in Figure 6-1 in order to have a safe system. Second, the UL curve in Figure 6-1 can be extended to its left for two additional decades by keeping its slope constant [79].

## 6.4. Electrical model for a DEA and human body

The DEA charging circuit in contact with a human body can be modeled as shown in Figure 6-2. Although this model is a very simple representation of a real case, it exposes the main parameters that affect the amplitude and current duration in high voltage discharges of DEA circuits to the human body [78], [133]. This first order, lumped model, neglects the inductance terms in all of the resistance elements. The DEA is represented by a non-ideal capacitor consisting of an ideal capacitor with a nominal capacitance of  $C_{DEA}$ , an equivalent series resistance ( $R_{ESR}$ ) and a dielectric leakage resistance ( $R_P$ ).  $R_{ESR}$  represents the electrical resistance in the DEA electrodes and  $R_P$  accounts for the electrical charge leakage through the dielectric medium[134]–[136].

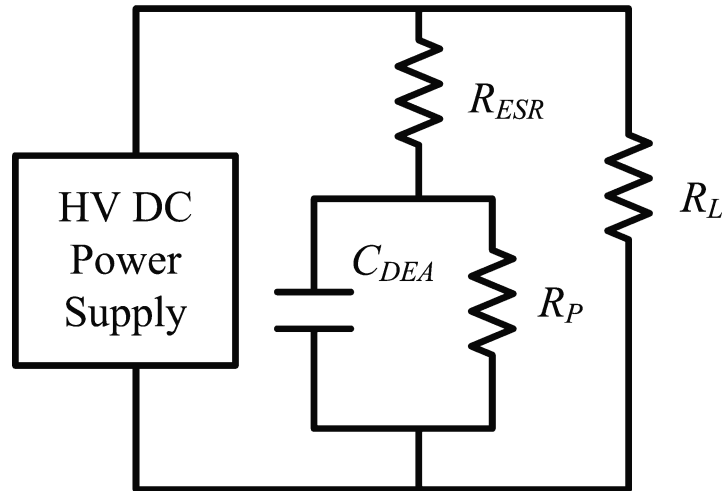


**Figure 6-2.** DEA circuit when it is in contact with the human body.

The electrical resistance of the human body ( $R_L$ ) is a complicated term and depends on many variables. There are different articles in the literature that discuss the total and regional impedance of the human body under different conditions [78], [79], [133], [137]. Particularly, the impedance of the human body depends on the touch voltage, amplitude, frequency and duration of current flow; the moisture level of the skin; and the body temperature. This impedance consists of internal body impedance and skin impedance. The skin protects the body from potential electric shocks and dry skin has a relatively high electrical resistance. However, when the human skin is wet or when voltages larger than 50V are touched, the resistance of the skin decreases rapidly and can be negligible [133]. Thus, based on the literature, the body resistance changes from 500-1000 $\Omega$ , which is the range of the internal human body impedance. Without loss of

generality, in this chapter, the simulations and results are obtained considering the lowest body resistance of  $500\Omega$ . The reader can refer to the above-mentioned references to identify the most suitable minimum resistance needed for specific applications.

## **6.5. Hazardous scenarios**

The DEA charging circuit can be in contact with the human body under three different scenarios: (1) A high voltage waveform is exposed to the human body before reaching the DEA; (2) the DEA is charged by a high voltage and while disconnected from the power source is exposed to the human body; and (3) the DEA is exposed to the human body while it is still connected to the power source. Each of the above scenarios is discussed in this section.

### **6.5.1. First scenario - High voltage power supply is touched**

In this scenario, the high voltage power supply (or alternatively high voltage amplifier) is directly in contact with the human body. In this case, the safest way is to limit the maximum output current of the power supply to just less than 20mA and use a circuit breaker that breaks for larger currents. In fact, based on the UL safety criteria of Figure 6-1, currents less than 20mA pose no threat of ventricular fibrillation for any duration.

### **6.5.2. Second scenario - The charged DEA is touched**

Capacitors are capable of storing electric charges via low currents and then discharge the stored energy via much higher currents. In this scenario, the electrical field energy stored in the DEA capacitor is discharged through the human body (Figure 6-3). Large discharge currents ( $> 1A$ ) passing through the human body are possibly very hazardous specifically if the minimum discharge resistance of the body (i.e.  $500\Omega$ ) is considered. However, based on Figure 6-1, large currents are not necessarily harmful. In fact, the duration of the current plays a key role in the harmfulness of the discharge current. Thus, the time response of the DEA discharge to the human body must be assessed and the current-duration levels must be checked with the UL safety criterion in Figure 6-1.

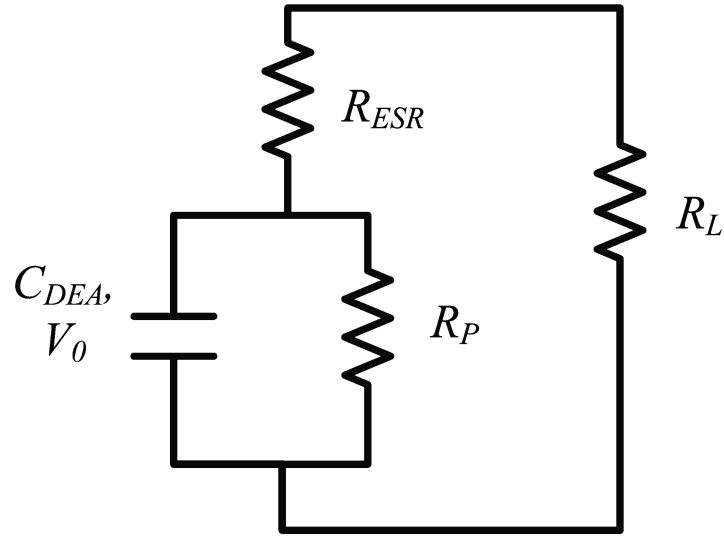


**Figure 6-3. Discharge circuit in the 2nd scenario.**

Based on Figure 6-3, the series connection of  $R_L$  and  $R_{ESR}$  is in parallel with  $R_p$  and  $C_{DEA}$ . Thus, the DEA discharge time constant and the current going through the human body load ( $i_L(t)$ ) is given by the following equations:

$$\tau = R_{EQV}C_{DEA} = (R_p \parallel (R_L + R_{ESR}))C_{DEA} = \frac{R_p(R_L + R_{ESR})}{R_p + (R_L + R_{ESR})}C_{DEA} \quad (1)$$

$$i_L(t) = i_{DEA}(t) - i_p(t) = \frac{R_p}{R_p + (R_L + R_{ESR})} \frac{V_0(R_p + (R_L + R_{ESR}))}{R_p(R_L + R_{ESR})} e^{-t/\tau} = \frac{V_0}{(R_L + R_{ESR})} e^{-t/\tau} \quad (2)$$

Where  $R_{EQV}$  is the equivalent resistance in the circuit of Figure 6-3,  $i_p(t)$  is the leakage current dissipating through the leakage resistance  $R_p$  and  $V_0$  is the voltage across the DEA capacitor at the time of human contact. Let's assume that the leakage resistance  $R_p$  is not present in Figure 6-3 circuit. In this case, the DEA discharge time constant and the load current  $i_L(t)$  is provided by:

$$\tau = (R_L + R_{ESR})C_{DEA} \quad (3)$$

$$i_L(t) = i_{DEA}(t) = \frac{V_0}{(R_L + R_{ESR})} e^{-t/\tau} \quad (4)$$

By comparing (1) and (3), and knowing  $R_p \parallel (R_L + R_{ESR}) < (R_L + R_{ESR})$ , it is evident that the discharge time constant in (1) is smaller than the time constant in (3). On the other hand, since the time constant in (2) is smaller than the time constant in (4) and the initial load currents  $i_L$  are the same, the current going through the human body is

smaller and decay faster in (2) comparing to (4). Thus, we can conclude that the presence of  $R_p$  results in a smaller amount of charge to discharge through the human body load  $R_L$  and in a shorter period of time. Subsequently, it means that considering  $R_p$  in the DEA circuit, causes a safer DEA discharge. Although there are some work that study  $R_p$  for DEAs [135], [138], [139], in this work the parameter  $R_p$  was neglected in order to investigate the most hazardous case that could possibly occur in DEA discharge to the human man body.

Equation (4) shows that increasing  $R_{ESR}$  causes the discharge load to increase, which limits the current passing through the human body. On the other hand, the UL curve in Figure 6-1 provides a safe current-duration limit. Such a curve can be digitized in the following piecewise function:

$$i_{UL}(t) = \begin{cases} 52 \times 10^{-4} \times t^{-0.72} & 10^{-6} \leq t < 4 \times 10^{-3} \\ 28 \times 10^{-2} & 4 \times 10^{-3} \leq t \leq 2 \times 10^{-2} \\ 2 \times 10^{-2} \times t^{-0.67} & 2 \times 10^{-2} < t < 1 \\ 2 \times 10^{-2} & 1 \leq t \end{cases} \quad (5)$$

For a given  $V_0$ ,  $R_L$  and  $R_{ESR}$ , the DEA capacitance can be calculated in such a way so that the current in (4) is always equal and less than the current in (5). Let us call the maximum capacitance that guarantees  $i_L(t) \leq i_{UL}(t)$  for all times, the DEA critical capacitance ( $C_{cr}$ ). Using (3), (4) and (5) and  $i_L(t) \leq i_{UL}(t)$  yields:

$$C_{DEA} \leq \frac{-t}{\ln\left(\frac{(R_L+R_{ESR})i_{UL}(t)}{V_0}\right)(R_L+R_{ESR})} \text{ for } 10^{-6} \leq t. \quad (6)$$

Using (6) and knowing that the capacitance should be a non-negative value, the DEA critical capacitance can be obtained from the following equation:

$$C_{cr} = \min\left(\frac{-t}{\ln\left(\frac{(R_L+R_{ESR})i_{UL}(t)}{V_0}\right)(R_L+R_{ESR})}\right) \text{ for } 10^{-6} \leq t \text{ and } \frac{-t}{\ln\left(\frac{(R_L+R_{ESR})i_{UL}(t)}{V_0}\right)(R_L+R_{ESR})} \geq 0. \quad (7)$$

If the DEA capacitance is equal or less than the  $C_{cr}$  calculated in (7), the discharge current to the human body is guaranteed to be in the safe region.

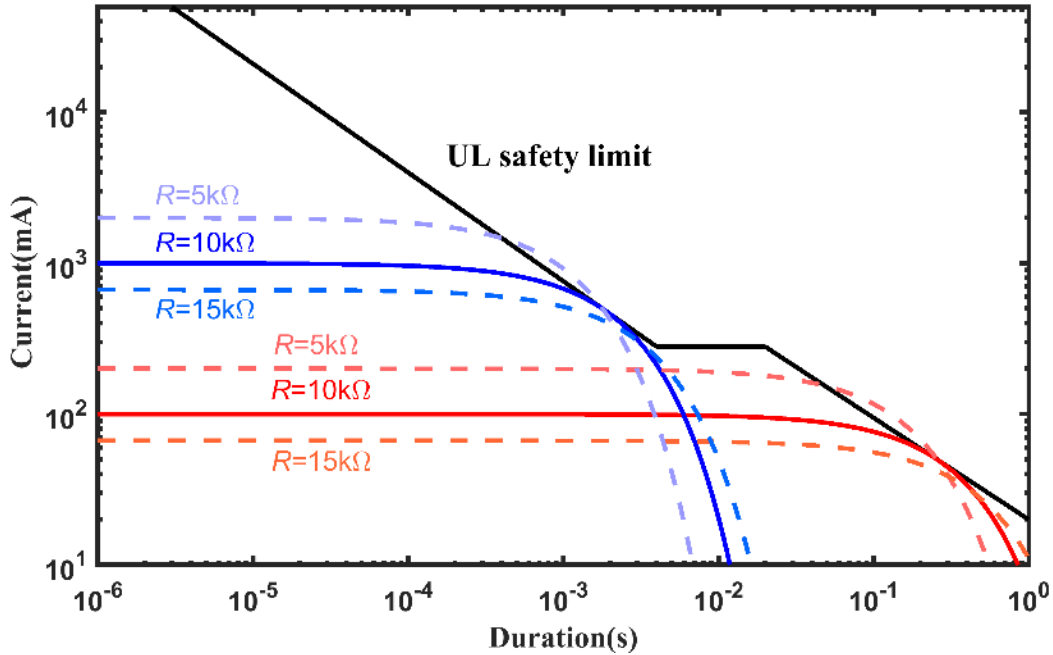


**Figure 6-4.** Simulated current-duration curves of DEA discharge circuit for the second scenario using the calculated critical capacitance given by equation (7).  $V_0$  is 10kV for the bundle of curves with blue tone and 1kV for the bundle with red tone. The solid lines are the current response using the critical capacitance for  $R=R_L + R_{ESR} = 10k\Omega$ . The dashed lines correspond to a similar capacitance as the solid lines but with a different resistance load. The critical capacitance is  $0.258\mu F$  for the blue curves and  $37.1\mu F$  for the red curves.

Figure 6-4 shows simulations of discharge current response for a charged DEA against the UL safety standard in logarithmic scale. In this figure, the initial capacitor voltage ( $V_0$ ) is 10kV for the upper bundle of curves and 1kV for the lower bundle. The solid blue curves show the discharge current state for a resistance load of  $R_L + R_{ESR} = 10k\Omega$  using the critical capacitance calculated by (6). This figure shows that the calculated optimal critical capacitance ( $C_{cr}$ ) causes the discharge current to be just within the safe region. The red dashed curves represent the discharge current using the calculated  $C_{cr}$  when different resistance loads are considered. Another observation from Figure 6-4 is that if the resistance load is lower than the expected value ( $R_L + R_{ESR} = 5k\Omega < 10k\Omega$ ), the actual discharge current may violate the safe limit. Thus, when designing the DEA capacitance, it should be made sure that the critical capacitance is calculated using the lowest possible value of the resistance load ( $R_L + R_{ESR}$ ).

Using (6), Figure 6-5 can be obtained that assists in the selection of a DEA capacitance when the initial voltage and discharge resistance load are given. For example,

if the DEA holds an initial voltage of 4kV and the discharge load value, consisting of the DEA and the human body resistance, is 16kΩ, then, according to Figure 6-5, the maximum allowable capacitance is almost 6μF. This choice of capacitance ensures that the DEA discharge current-duration is within the safe range based on the UL standard.

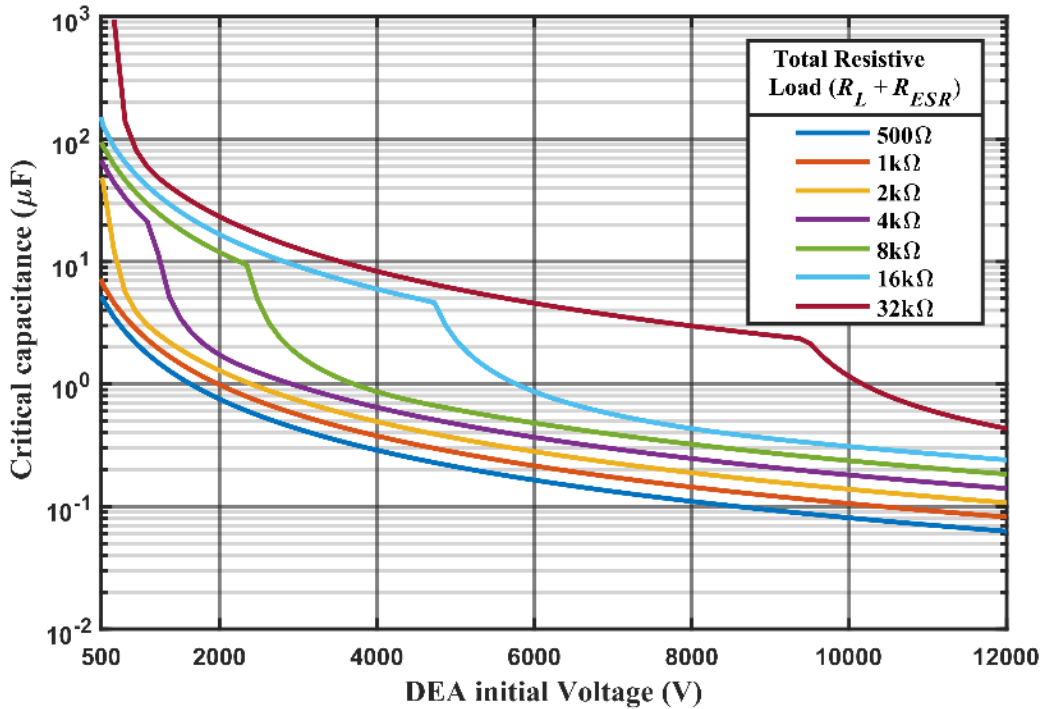


Figure 6-5. DEA critical capacitance for different initial voltages and resistance loads based on the second scenario.

### 6.5.3. Third scenario – A charged DEA while attached to a power source is touched

In this scenario, a charged DEA gets in contact with the human body while it is connected to a power supply (see Figure 6-2). Current may flow to the human body ( $R_L$ ) from both the power supply and the charged DEA. Depending on the performance of the power source two extreme cases may happen as follows:

#### ***Power source voltage output across the DEA stays equal or above the charged DEA voltage before the touch***

In this condition, the current will not flow from the charged DEA to the human body and hence a situation similar to the first scenario is observed. Similarly, in order to meet the safety requirements, the power source current should be limited to less than 20mA.

**Power source voltage output across the DEA drops below the charged DEA voltage before the touch**

In this case, the voltage across the DEA drops and hence the DEA is fully or partially discharged into the power source or human body. To consider the worst-case scenario, let us assume that the DEA is fully discharged to the human body. Thus, the current flowing into the human body is the superposition of the current from both the power source and the DEA discharge. Considering the current from the power source is limited to 20mA, the superposed current is given by:

$$i_L(t) = i_{DEA}(t) + 2 \times 10^{-2} = \frac{V_0}{(R_L + R_{ESR})} e^{-t/\tau} + 2 \times 10^{-2} \quad (8)$$

The DEA should be designed in such a way so that the superimposed current falls in the safe region of the UL curve in Figure 6-1. Similar to the second scenario, the critical capacitance can be obtained using equation (9):

$$C_{cr} = \min \left( \frac{-t}{\ln \left( \frac{(R_L + R_{ESR})}{V_0} (i_{UL}(t) - 0.02) \right) (R_L + R_{ESR})} \right) \text{ for } 10^{-6} \leq t \text{ and } \frac{-t}{\ln \left( \frac{(R_L + R_{ESR})}{V_0} (i_{UL}(t) - 0.02) \right) (R_L + R_{ESR})} \geq 0. \quad (9)$$

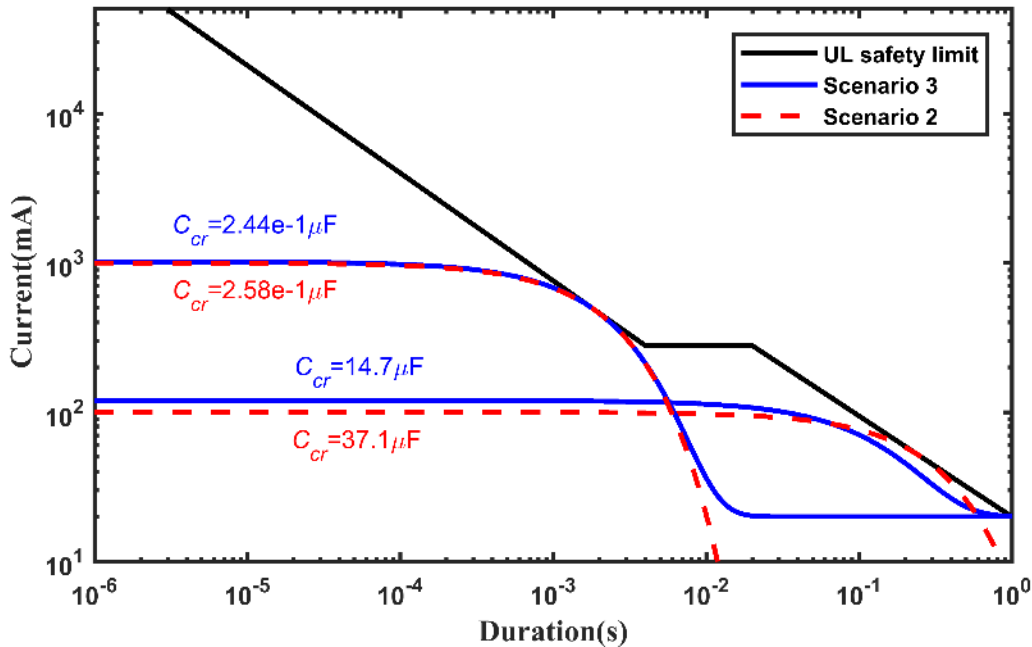


**Figure 6-6.** Current-duration simulations of DEA discharge circuit for the second and third scenarios in logarithmic scale. Discharge curves are simulated using calculated critical capacitances for a given  $V_0$  and  $R=R_L + R_{ESR} = 10k\Omega$ .  $V_0$  is 10kV for the upper curves and 1kV for the lower curves.

Figure 6-6 illustrates the current-duration simulations of DEA discharge circuits for the second and third scenarios using a logarithmic scale. These simulations show that the DEA circuit discharge current falls just below the UL safety limit using the calculated  $C_{cr}$  in both scenarios. The critical capacitances are shown beside each curve with their corresponding color and are obtained using the same  $V_0$  and  $R$  as in Figure 6-4. The solid blue lines represent curves based on the third scenario and the dashed red lines represent the curves in the second scenario. Figure 6-6 shows that, for a similar  $V_0$  and  $R$ , the DEA critical capacitance  $C_{cr}$  in the third scenario should be less than critical capacitance in the second scenario to fulfill the UL safety criterion. Another observation from the solid lower curve in Figure 6-6 is that for circuits with an initial discharge current close to 20mA, the critical capacitance in the third scenario should be small enough to allow slow discharge current decay to 20mA and below the UL safety limit. This observation can also be seen in Figure 6-7 where the DEA critical capacitance  $C_{cr}$  in the third scenario is plotted for given initial voltages and circuit resistive loads. Similar to Figure 6-5, Figure 6-7 can be used to determine the DEA capacitance knowing the initial voltage and the load resistance in the circuit.

By comparing Figure 6-5 and Figure 6-7 it is concluded that for a given  $V_0$  and  $R=R_L+R_{ESR}$  the third scenario provides a smaller DEA critical capacitance. Thus, to design a DEA, the worst-case scenario (third scenario) should be considered and the DEA critical capacitance in Figure 6-7 can be used for this purpose. Once the DEA's critical capacitance is determined for a given  $V_0$  and  $R=R_L+R_{ESR}$ , further parameters of the DEA can be optimized in order to result in a safe DEA. The design parameters depend on the geometry and configuration of the DEA. In this work, the planar and cylindrical DEA configurations, which have extensively been studied in the literature [2], [8], [27], [59], [140] and are widely used as the main components of DEA devices, are investigated. In the next section, it will be discussed that a DEA yields the maximum capacitance when it is stretched and actuated thus in order to have a safe DEA, this maximum capacitance should be equal or less than the critical capacitance in Figure 6-7.

In conclusion, if a DEA circuit gets touched by a human body, any of the three scenarios discussed above is possible. The application of circuit breaker concluded from the first scenario and the safe range of values for the DEA parameters obtained from the third scenario must be applied to ensure the safe operation of a DEA device.

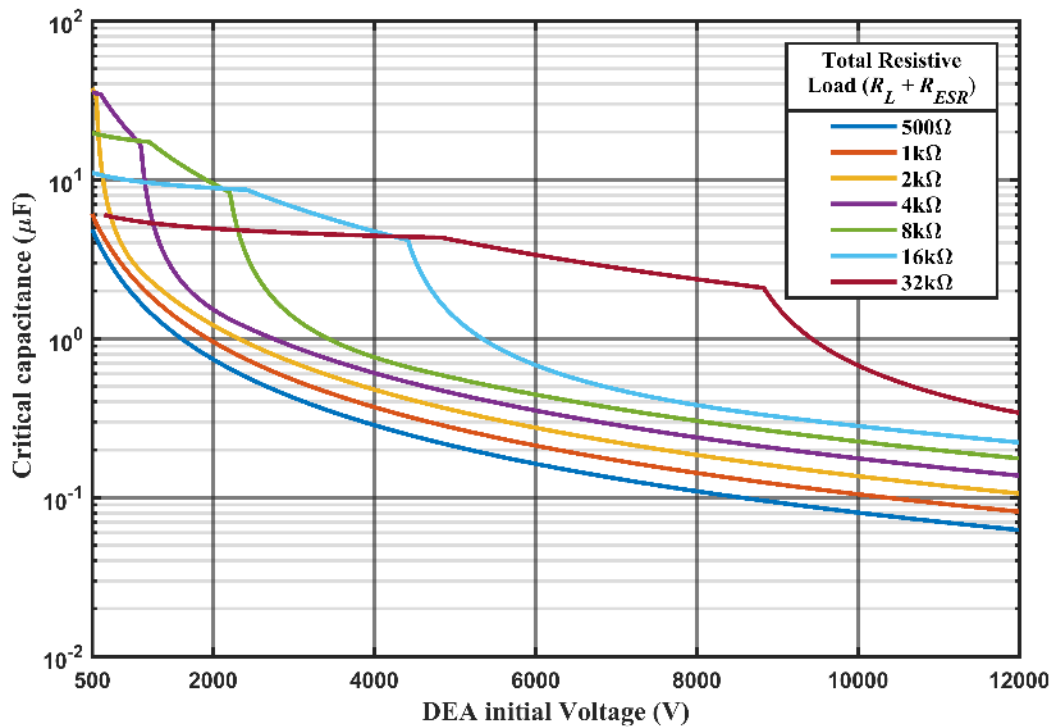


**Figure 6-7. DEA critical capacitance for different initial voltages and resistance loads based on the third scenario.**

## 6.6. DEA geometrical parameter design

### 6.6.1. Planar DEA

The capacitance of DEAs having a planar configuration is given by [141]:

$$C = N \frac{\epsilon_0 \epsilon_r A}{d} \quad (10)$$

where  $N$  is the number of DEA layers (i.e. the number of electrode layers minus 1),  $\epsilon_0=8.85 \times 10^{-12}$  F/m is the vacuum permittivity,  $\epsilon_r$  is the material's relative dielectric constant,  $A$  is the active area of the DEA and  $d$  is the dielectric thickness. Based on (10) the capacitance increases as the active area increases or as the dielectric thickness decreases. Regarding the variation of relative dielectric constant  $\epsilon_r$ , it has been shown that in general, this constant reduces when the elastomer is stretched [142]–[144]. Assuming the dielectric constant  $\epsilon_r$  is fixed throughout the stretch and is equal to its maximum value (worst-case scenario), which is when the elastomer is not strained, the DEA yields the maximum capacitance when it is stretched and actuated. For a safe DEA, this capacitance should be equal or less than the critical capacitance discussed in the previous section. The initial capacitance of the DEA before being stretch or actuated ( $C_0$ ) is given by:

$$C_0 = N \frac{\epsilon_0 \epsilon_r A_0}{d_0}. \quad (11)$$

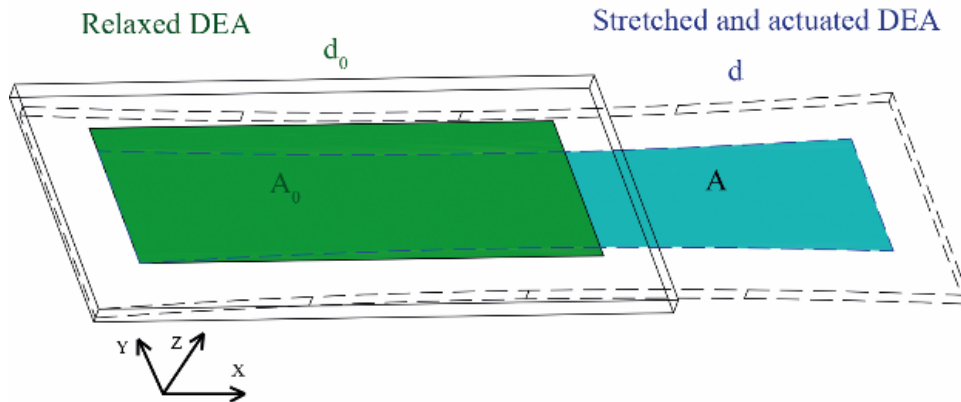


**Figure 6-8. Relaxed and stretched planar DEA.**

Figure 6-8 shows a schematic of a planar DEA in relaxed and stretched states. Assuming the dielectric elastomer is incompressible [27], [145] then:

$$\lambda_x \lambda_y \lambda_z = 1 \quad (12)$$

where  $\lambda_x$ ,  $\lambda_y$  and  $\lambda_z$  are the stretch ratios for the length (X-axis), width (Y-axis) and thickness (Z-axis) of the stretched and actuated DEA respectively (e.g.  $\lambda_z = \frac{d}{d_0}$ ).

Using (10), (11) and (12), a safe initial capacitance ( $C_0$ ) for a DEA can be achieved as follows:

$$C_0 = \lambda_z^2 C_{cr} \Rightarrow \frac{A_0}{d_0} = \frac{\lambda_z^2 C_{cr}}{N \epsilon_0 \epsilon_r}. \quad (13)$$

Figure 6-9 shows the safe limits of the initial area to thickness ratio of a planar DEA capacitor using (13) given that the DEA number of layers, the dielectric constant and  $\lambda_z$  are known.

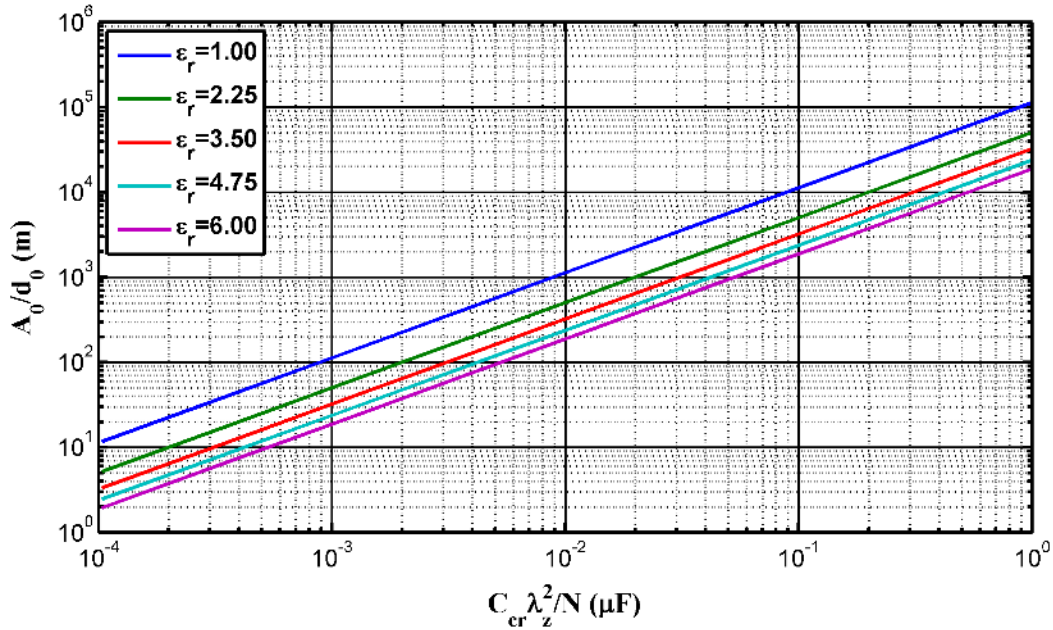


**Figure 6-9. Initial area to thickness ratio for a safe planar DEA capacitor. The area under these curves represents the safe region.**

### 6.6.2. Cylindrical DEA

The capacitance of a cylindrical DEA is given by [141]:

$$C = \frac{2\pi\epsilon_0\epsilon_r L}{\ln(b/a)} \quad (14)$$

where  $L$  is the length of the cylinder and  $a$  and  $b$  are the inner and outer radii of the cylinder respectively as shown in Figure 6-10. Similar to the case of the planar DEA,

(12) yields that the cylindrical DEA has its maximum capacitance when stretched and actuated (smaller  $b/a$  ratio). Thus, the cylindrical DEA capacitance, when stretched and actuated, should be equal or less than the critical capacitance. The safe range for  $\frac{L}{\ln(b/a)}$  ratio is illustrated in Figure 6-11 for different dielectric constants  $\epsilon_r$ .

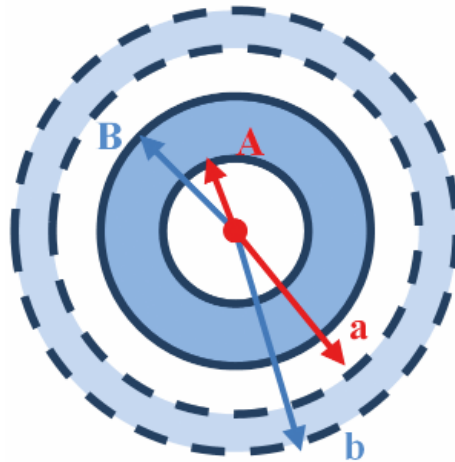


**Figure 6-10. Cross-section of a cylindrical DEA relaxed and under stretch.  $a$  and  $b$  are the inner and outer radii of the stretched and actuated DEA while  $A$  and  $B$  are the similar values when relaxed.**

In several applications, the length  $L$  of the cylinder can be assumed to be constrained during the actuation [4], [27]. In such conditions, Figure 6-11 can be broken down to Figure 6-12 that shows the dielectric thickness to inner radii ratio  $\frac{b-a}{a}$  for different values of DEA length. In Figure 6-12, the thickness to the inner radii ratio is plotted instead of the outer to inner radii ratio to improve the graphical presentation in logarithmic scale.

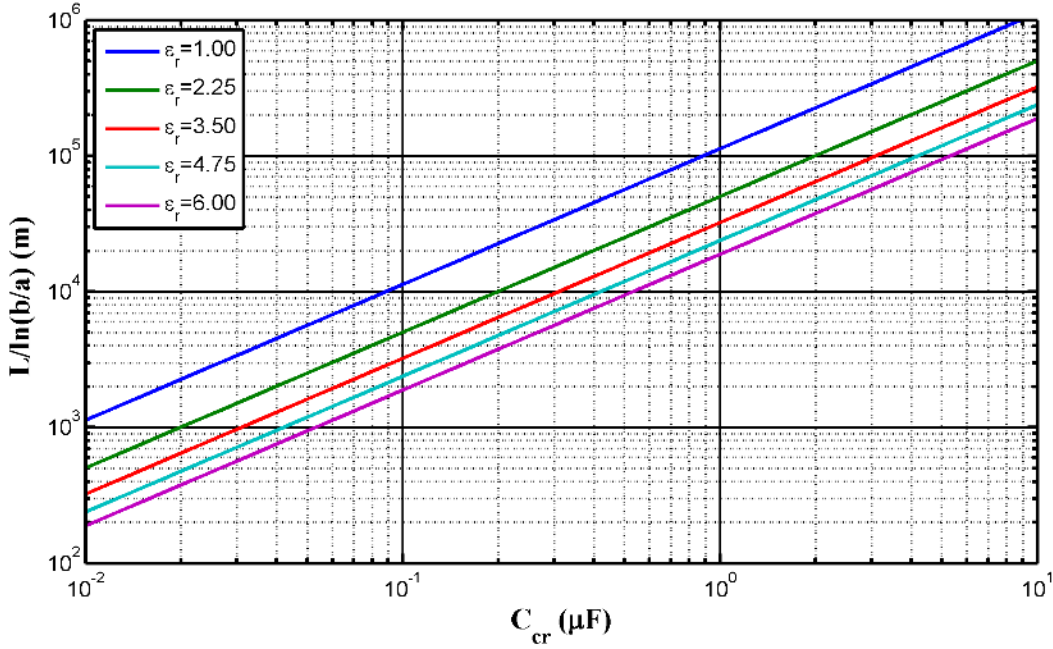


**Figure 6-11. The safe values for geometrical parameters of stretched and actuated cylindrical DEA for different dielectric relative permittivity. The area under the curves shows the safe range.**

The dielectric incompressibility yields:

$$\pi(B^2 - A^2) = \pi(b^2 - a^2). \quad (15)$$

By canceling  $\pi$  and dividing both sides by  $A^2$ , a relationship for the initial geometry of the cylinder is obtained:

$$\frac{B}{A} = \sqrt{((b/a)^2 - 1)\lambda_a^2 + 1} \quad (16)$$

where  $\lambda_a$  is the inner radii stretch ratio, defined as  $\frac{a}{A}$ . Figure 6-13 represents the curves for initial thickness to the inner radii ratio required to provide a safe cylindrical DEA for different inner radial stretch ratios. In this figure, the initial thickness to the inner radii ratio is plotted on the vertical axis for convenience. Figure 6-11 to Figure 6-13 can be used in conjunction with each other to design a safe cylindrical DEA. It should be noted that in Figure 6-12 and Figure 6-13 the regions above the curves are safe.

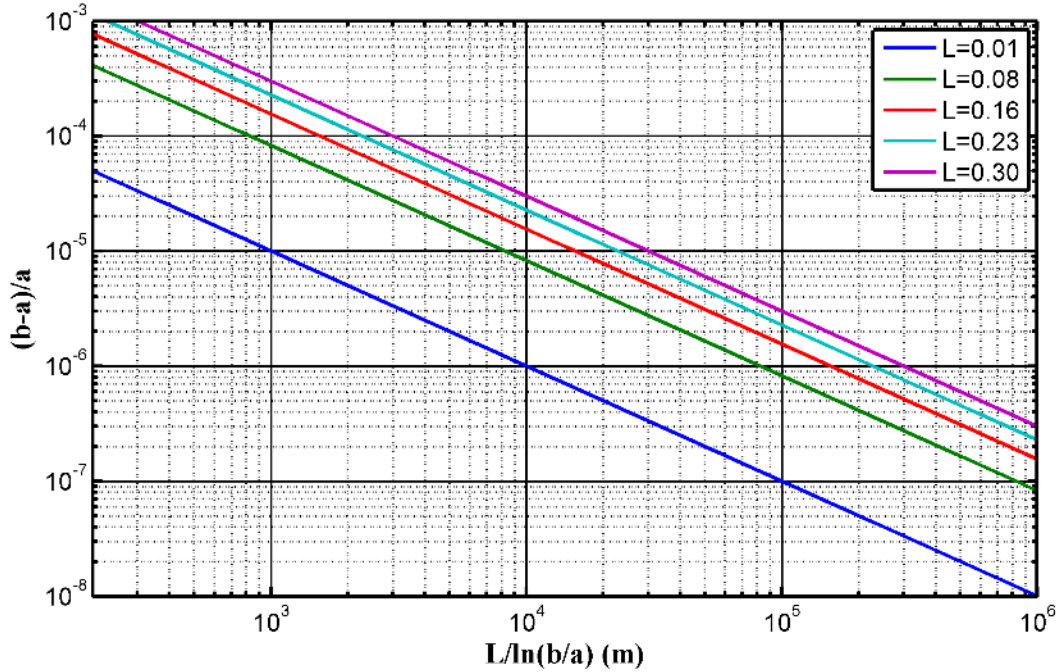


Figure 6-12. Stretched and actuated dielectric thickness to inner radii ratio for different lengths of cylindrical DEAs. The regions above the curves are safe.

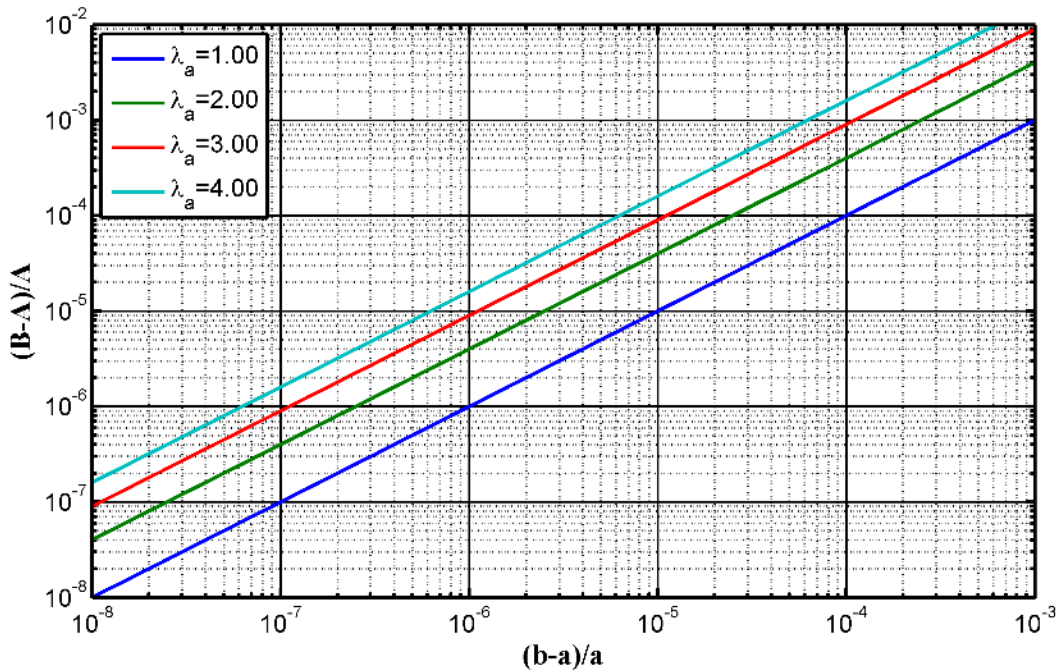


Figure 6-13. Initial thickness to inner radii ratio of a safe cylindrical DEA for different stretch ratios. The safe region is the area above the curves.

## 6.7. Experimental Verification

In the first hazardous scenario, the body is connected to the output of the power supply without a DEA. In this scenario, if the output current on the power supply is limited to 20 mA the safety of the circuit is ensured as long as it is connected to the body based on the UL safety criteria. However, for the second and the third scenarios, a DEA circuit model was used to introduce DEA critical capacitance which can be used to design DEAs that result in a safe current discharge to the human body. To verify the analytical models that were described in the second and third hazardous scenarios, an experimental procedure was developed in the second scenario. In this chapter, the second scenario was experimented to avoid the experimental dynamics of the power supply, present in the third scenario. By verifying the second scenario, the third scenario is also verified knowing that the third scenario is, in general, the superposition of the first and the second scenarios.

Prepared planar DEA samples were charged with a high voltage and then discharged into a 500Ω resistance that represented the worst-case scenario of human body resistance. By measuring the charge passing through this resistor, the DEA capacitance was calculated. This capacitance was compared with the capacitance calculated from (10) to verify the analytical procedure.

The schematic diagram of a DEA charge and discharge circuit is shown in Figure 6-14. Components were selected to simulate the condition where a planar DEA was actuated by providing up to 10kV. This is a very common scenario representing a realistic condition [33], [146]–[148].

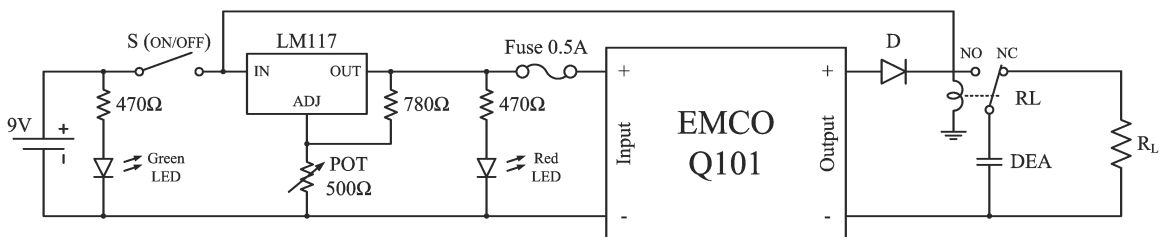


**Figure 6-14. Circuit of the DEA discharge to an equivalent human body load.**

The specifications of the main components used in this circuit were as follows:

1. EMCO Q101, proportional dc-dc converter, 10kV output voltage;

2. D: FCI Semiconductor HV03-12, high voltage diode, 12kV;
3. RL: Relay;
4.  $R_L$ : Load resistor 500 $\Omega$  (non-inductive).

The circuit on the input of the EMCO Q101 provided a variable dc voltage up to 5V. The output voltage of the EMCO Q101 could reach up to 10kV and was proportional to its input voltage. Therefore, by changing the input voltage using the potentiometer POT, the output voltage could be adjusted. Figure 6-14 shows the normal condition of the circuit when the switch S was OFF and the input of the EMCO was not energized. When the switch S turned ON, the regulator LM117 provided the voltage for the input of the EMCO converter based on the value of potentiometer POT. In this condition, RL relay switched to its normally open (NO) state and the output voltage of the EMCO converter was applied across the DEA. This switching resulted in the DEA to be charged up to the output voltage of the EMCO converter. When the switch S turned OFF, the input voltage of the EMCO converter and accordingly its output voltage, dropped down to zero. Meanwhile, RL switched to normally close (NC) state and the stored energy in the DEA was dissipated through the load resistor  $R_L$ . This set-up simulated the charged DEA discharge into the human body described by the second scenario. By measuring the voltage across  $R_L$ , the DEA discharge current and consequently its total charge could be calculated.

Based on the schematic in Figure 6-14, a circuit for measuring the DEA discharge current was developed as shown in Figure 6-15. Due to the high voltage on the converter's output, all the components were assembled on a non-copper pre-drilled board and far enough from each other to prevent any arc. A 0.5A fuse was placed on the input of the converter to prevent it from damage in case of any fault. The red LED turns ON when the switch S is ON, which is an indicator of the presence of high voltage in the circuit. It should be noted that for the HV converter in this study, i.e., EMCO Q101, the output current was limited to 50 $\mu$ A. Thus, the safe condition for the first hazardous scenario was met.

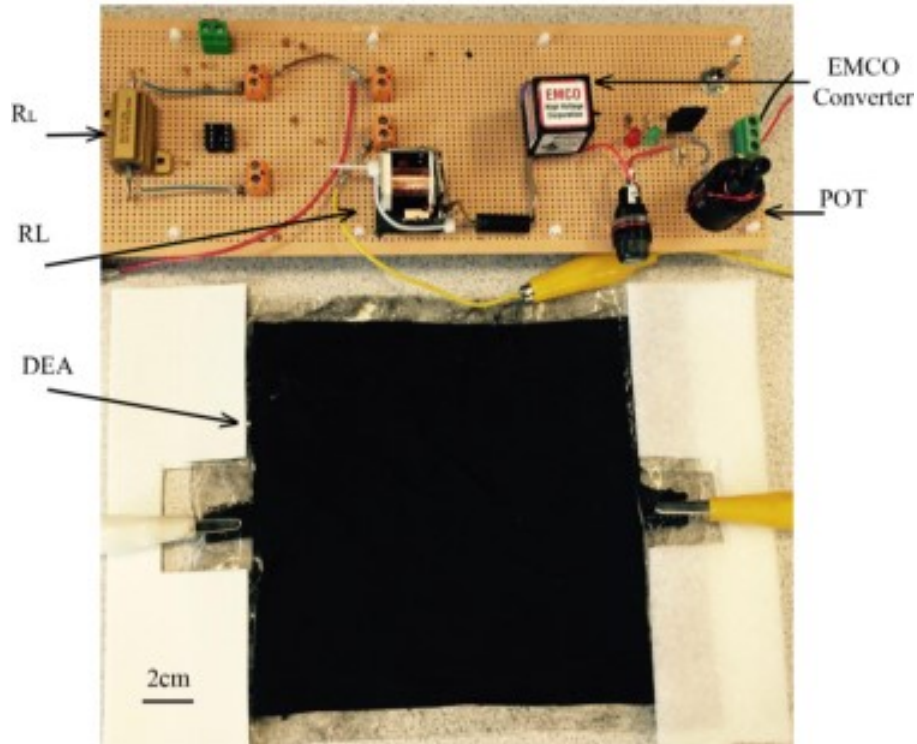


**Figure 6-15.** The prototype of the DEA discharge circuit.

### 6.7.1. Experimental procedure

Two planar DEA samples were fabricated using a silicone elastomer coated with carbon black electrodes. The geometrical dimensions of each sample are provided in Table 6-1. First, the DEA was stretched to a certain strain and then it was charged up to 2.8 kV, which was the minimum output voltage of the converter based on our design. Subsequently, the DEA was discharged to the load resistance  $R_L$  while the voltage across this resistance was measured. This procedure was repeated three times for a certain DEA strain and then measured voltages were used to calculate the DEA capacitance. Finally, the three capacitances were averaged for each DEA in each stretch for more accuracy. For measuring the load voltage, while the DEA was discharged, a high-resolution (20GS/s) scope LeCroy 604Zi was utilized. Each test was saved in an Excel file format and then imported to Excel for further calculations and analysis.

**Table 6-1. Geometrical properties of experimental DEA samples.**

	Number of layers $N$	Electrode length (cm)	Electrode area, $A_0$ (cm <sup>2</sup> )	Dielectric thickness, $d_0$ (cm)	Area to thickness ratio, $\frac{A_0}{d_0}$ (cm)
Sample 1	1	15.1	226.3	0.040	5657.5
Sample 2	1	15.2	233.7	0.036	6490.0

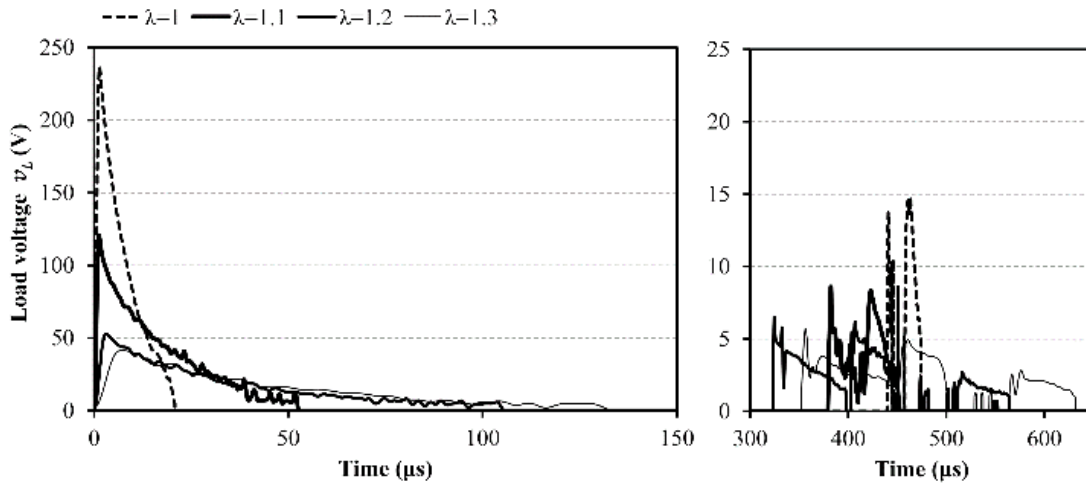


**Figure 6-16. Load voltage while the DEA is discharged.  $\lambda$  represents the DEA stretch ratio in the longitudinal direction.**

### 6.7.2. Model verification

Figure 6-16 shows the experimental load voltage for the DEA Sample 1 in four different arbitrary stretch ratios ( $\lambda$ ), i.e., 1.0, 1.1, 1.2, and 1.3. The main DEA voltage decay happened around the first hundred microseconds of the discharge which is shown on the left plot in Figure 6-16. In addition to the main decay, the plot on the right of Figure 6-16 shows a smaller discharge decay that occurred a few hundred microseconds later and with lower amplitude. This separation was due to the spark between the contacts of the RL relay that turned ON and OFF when it switched to NC. In other words, when RL changed to NC, the high voltage across the DEA ignited a spark along the switch and that was when the discharge occurred. It caused the DEA voltage to drop down and turn off the spark before the RL reached NC. The rest of the DEA charge flew to the load resistor

when the switch was in NC state. This phenomenon was due to the fact that it took some finite time for the RL relay to mechanically switch state. For the performed experiment, it was assumed that the charges stored in the DEA pass through the load resistance  $R_L$ . By taking the integral of the load voltage  $v_L(t)$  over time and dividing by the charge voltage  $V$  and load resistance  $R_L$  the DEA capacitance can be obtained as follows:

$$C = \frac{\int_0^{\infty} v_L(t) dt}{VR_L}. \quad (17)$$

This procedure was followed for the load voltages of all experiments and the capacitances were calculated as listed in Table 6-2 and Table 6-3.

**Table 6-2. Experimental and analytical capacitances for DEA Sample 1.**

Stretch Ratio ( $\lambda$ )	Areal stretch ratio $\lambda_x\lambda_y$ , (by image processing)	Analytical capacitance (nF)	Experimental capacitance (nF)	Model relative error (%)
1.0	1.00	1.50	1.51	0.7
1.1	1.05	1.66	1.61	3.0
1.2	1.10	1.83	1.65	9.8
1.3	1.15	2.00	1.83	8.5

**Table 6-3. Experimental and analytical capacitances for DEA Sample 2.**

Stretch Ratio ( $\lambda$ )	Areal stretch ratio $\lambda_x\lambda_y$ , (by image processing)	Analytical capacitance (nF)	Experimental capacitance (nF)	Model relative error (%)
1.0	1.00	1.79	1.85	3.4
1.1	1.08	2.00	2.10	5.0
1.2	1.12	2.18	2.30	5.5
1.3	1.16	2.31	2.35	1.7

During the experiments, for each stretch ratio, a photo was taken from the DEA. Each image was processed to analytically calculate the DEA capacitance using (10). Since the DEA electrodes were black in contrast to the translucent dielectric elastomer, the active electrode part of the DEA in the image was easily isolated. Then based on the number of pixels in the area and the image scale, the areal stretch ratio  $\lambda_x\lambda_y$  was calculated by which  $\lambda_z$  can be obtained using (12). Finally, by knowing the initial area to thickness ratio  $\frac{A_0}{a_0}$ , given in Table 6-1, and the relative dielectric constant for the silicone elastomer  $\epsilon_r = 3$ , the DEA capacitance was calculated using (10). For comparison, the

analytical capacitances obtained from this method and the experimental capacitances obtained from the discharge measurement method were listed in Table 6-2 and Table 6-3 for Sample 1 and Sample 2, respectively. The results in these tables show that the DEA model considered in this study (Figure 6-3) shows a relative error of less than 10.0%. The resulted error may be due to the uneven thickness of the DEA samples. Moreover, the voltage measurement error in the experimental calculations contributed to the overall error.

The DEA model shown in Figure 6-3 was estimated using the load voltage obtained in the experiments as shown in Figure 6-16. The relationship between the peak of the DEA voltage and the peak of the load voltage during the discharge is given by:

$$v_{L\text{peak}} = v_{DEA\text{peak}} \times \frac{R_L}{R_{ESR} + R_L} \quad (18)$$

where  $v_{DEA\text{peak}}$  and  $R_L$  are 2.8 kV and 500  $\Omega$ , respectively. By measuring the peak of the load voltage  $v_{L\text{peak}}$  using Figure 6-16, the DEA series resistance  $R_{ESR}$  could be obtained. This resistance was obtained for four different stretches as listed in Table 6-4. Also, given the DEA model shown in Figure 6-3, the parallel resistance  $R_p$  was calculated by using (1). An exponential function in the form of  $v_L(t) = v_{L\text{peak}}e^{t/\tau}$  was fitted to each measured load voltage and the time constant  $\tau$  was calculated. Then using (17) and having  $R_{ESR}$ ,  $R_L$ , and  $C_{DEA}$  the parallel resistance was obtained as listed in Table 6-4. The results for  $R_p$  showed that this resistance was very large compared with the series and load resistances. The results in Table 6-2 and Table 6-3 neglect the  $R_p$  parameter in the DEA modelling, which may account for potential prediction errors. A magnified plot for two waveforms of Figure 6-16 is shown in Figure 6-17 with their corresponding exponential fitted curve.

**Table 6-4. Circuit parameters of experimental DEAs.**

Stretch Ratio ( $\lambda$ )	Sample 1			Sample 2		
	$R_{ESR}$ (k $\Omega$ )	$R_p$ (k $\Omega$ )	$\tau$ ( $\mu$ s)	$R_{ESR}$ (k $\Omega$ )	$R_p$ (k $\Omega$ )	$\tau$ ( $\mu$ s)
1.0	5.5	430.7	8.95	5.5	372.1	9.9
1.1	10.8	289.7	18.10	8.2	256.3	15.1
1.2	25.9	205.0	42.80	11.0	198.1	20.0
1.3	31.1	167.8	53.20	12.8	147.6	21.3

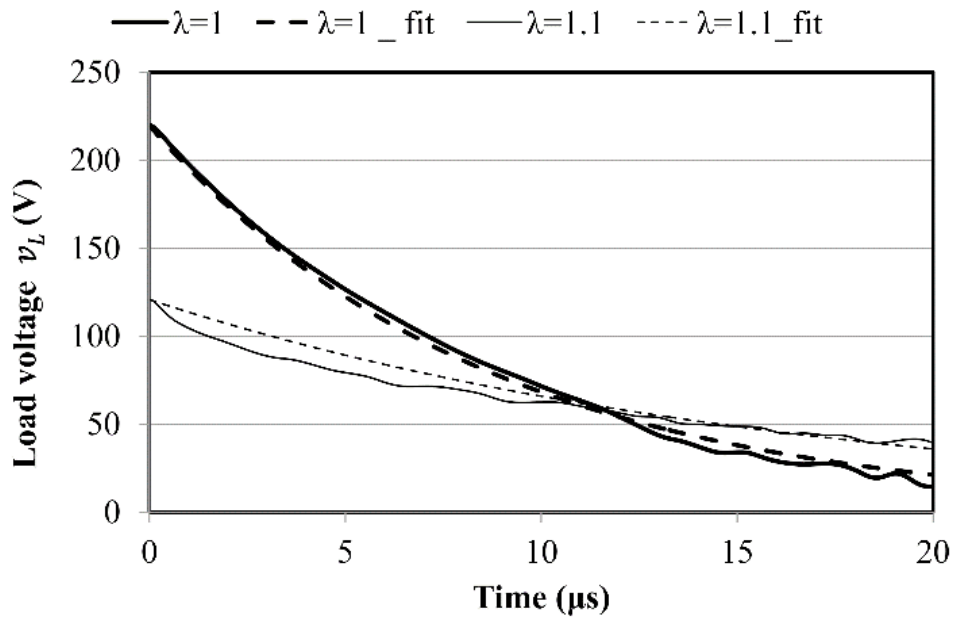


**Figure 6-17. Load voltages for  $\lambda=1$  and 1.1 with their fitted exponential plots.**

The experimental DEA discharge current to a  $500\Omega$  load resistance, which simulates the human body's resistance, for four different stretches of Sample 1 compared with the UL standard are plotted in logarithmic scale in Figure 6-18. It shows that these discharge currents for all stretches are well below the safety threshold given by the standard.

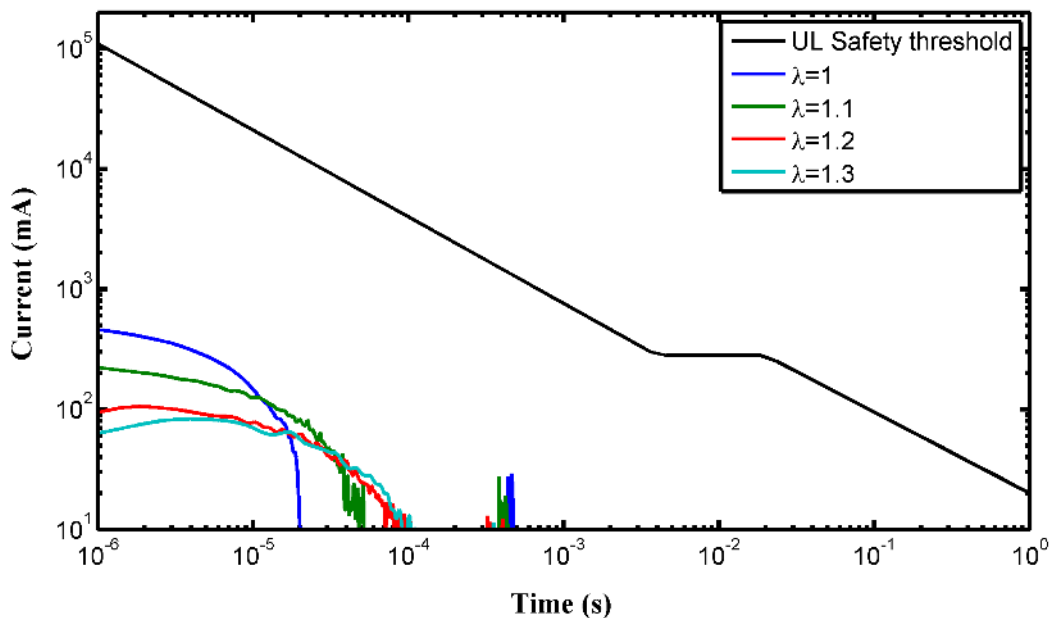


**Figure 6-18. DEA discharge current through  $500\Omega$  load resistance for four different stretch ratios compared to the UL safety threshold.**

Also, Figure 6-9 could be used to identify if the experimented DEA samples are safe or not. In this regard, based on Figure 6-5, the DEA critical capacitance for a 2.8 kV charging voltage and a minimum load resistance of  $5.5\text{k}\Omega + 0.5\text{k}\Omega = 6\text{k}\Omega$  ( $5.5\text{ k}\Omega$  is the minimum  $R_{ESR}$  for both samples) is  $1.3\mu\text{F}$ . Using this critical capacitance and the information given in Table 6-1 to Table 6-3., the status for DEA Samples 1 and Sample 2 can be indicated inside Figure 6-9. This status is shown in Figure 6-19. Since the corresponding initial area to thickness ratio  $\frac{A_0}{d_0}$  for Sample 1 and Sample 2 are below the safe limit, these experimented samples are determined to be safe.

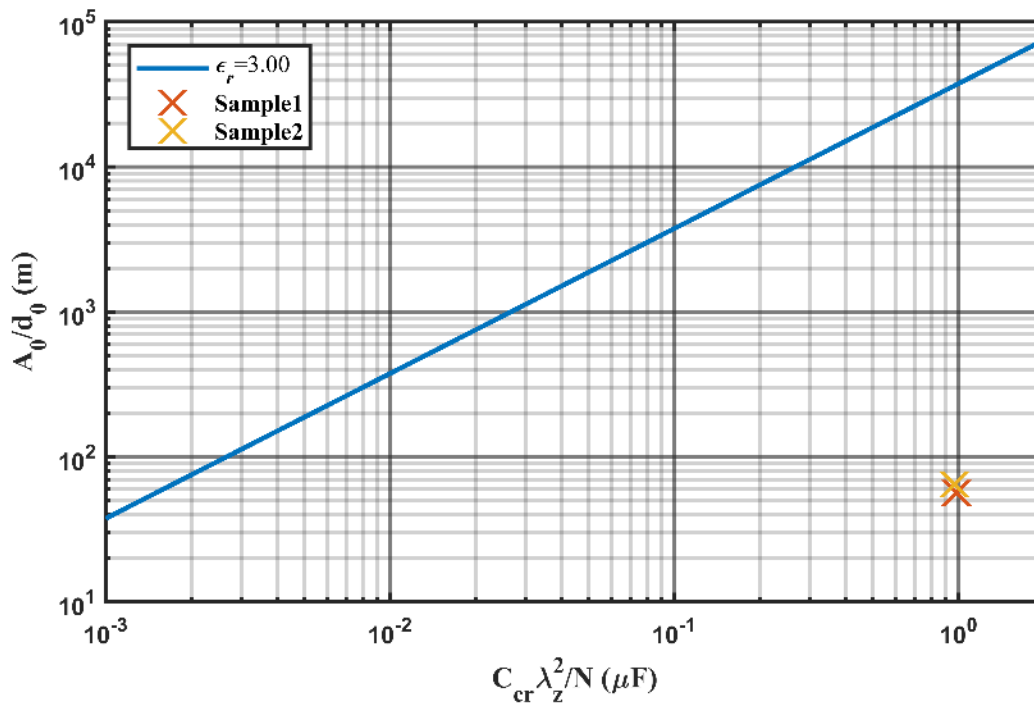


**Figure 6-19. Status of the initial area to thickness ratio for DEA Sample 1 and Sample 2 inside Figure 6-9. Since both samples are under the safety limit curve, they are safe.**

## 6.8. Case study - DEA active compression bandage

DEAs have the potential to be used as soft actuation system of soft-exosuits and other soft smart garments, such as compression garments. In this section, we investigate the practical use case of chapter 3 where a DEA is used as an active compression bandage, which could form the building block of a compression garment. In this practical application, the DEA bandage should be in direct or close contact with the human body. Despite the fact that the DEA bandage can be properly insulated, the study of the DEA's

electrical discharge to the body is investigated in this study in case of any failure of the insulating layer. The investigated DEA has a planar geometry and is to be wrapped around the leg, thus assuming a final cylindrical shape as shown in Figure 6-20.



**Figure 6-20. DEA based compression garment.**

The DEA is charged using a high voltage DC-DC converter (EMCO Q101) to voltages up to 11.3kV. Note that the converter maximum output current is limited to 50 $\mu$ A. Therefore, the 1st exposure scenario does not pose a risk to the human body since the discharge current is well below the safety limit of 20mA.

Although the converter output current is very low, the DEA is capable of storing a considerable amount of charge. If the charged DEA is touched by the human body, it discharges a potentially large amount of current. The 50 $\mu$ A output current of the converter applies a voltage drop of 25mV across the lowest human body resistance of 500 $\Omega$ . Thus, the worst-case scenario happens when the converter connected to the fully charged DEA is touched which resembles the scenario described in section 6.5.3. Considering a maximum charging voltage of 11.3kV and assuming the lowest human body resistance of 500 $\Omega$  and minimum resistance of zero for DEA series resistance  $R_{ESR}$ , a critical capacitance of 6.8 $\times 10^{-2}\mu$ F is obtained using Figure 6-7. Similar to the work presented in chapter 3, it is assumed that single layer DEA with a dielectric that presumably did not

exceed a stretch ratio of 2 and had a dielectric constant of 4.7 is used in this case. Considering a planar geometry for the DEA for when the bandage is flattened out and using Figure 6-9, the dielectric elastomer's initial area to thickness ratio must be less than  $4.0 \times 10^2 \text{m}$  to have a safe DEA bandage. Assuming a dielectric thickness of 1.34mm, the initial active area of DEA can have an area up to  $5.36 \times 10^{-1} \text{m}^2$ , which is very large for the considered application.

Considering the planar DEA bandage is wrapped around the limb a cylindrical geometry is formed with the same critical capacitance of  $6.8 \times 10^{-2} \mu\text{F}$ . Using Figure 6-11 to Figure 6-13 and assuming a constrained length of 0.23m and a maximum radial stretch ratio of 4, the initial thickness to inner radii must be less than  $2.24 \times 10^{-3}$  to have safe DEA bandage. Assuming 1.34mm for the initial thickness of the elastomer, the initial radii of the cylindrical DEA should be less than 0.6m which is equivalent to a DEA with an active area of  $8.67 \times 10^{-1} \text{m}^2$  ( $0.6\text{m} \times 2\pi \times 0.23\text{m} = 8.67 \times 10^{-1} \text{m}^2$ ). Thus, if the planar DEA with a  $5.36 \times 10^{-1} \text{m}^2$  active area and a 0.23m width is wrapped around a limb, the DEA would be safe in both planar and cylindrical configurations.

Let's assume a hypothetical case in which a 10-layer planar DEA uses the same dielectric medium with a thickness of 100 $\mu\text{m}$ , and across each layer 11.3kV is applied. In this case, the critical capacitance is similarly 68nF, however, the initial area to thickness ratio of the DEA must be less than  $1.8 \times 10^1 \text{m}$  using Figure 6-9. Thus, the initial allowable active area should not be larger than  $1.8 \times 10^{-3} \text{m}^2$  ( $1.8 \times 10^1 \text{m} \times 1 \times 10^{-4} \text{m} = 1.8 \times 10^{-3} \text{m}^2$ ).

## 6.9. Conclusion

The use of dielectric elastomer actuators (DEA) is rapidly growing in a variety of different applications. Many of the DEA applications are developed for human users requiring direct or close contact with the human body. Examples include wearables, human assistive devices, soft exoskeletons, and smart compressive garments. Since DEAs are generally operated with high voltages, their use in human consumer devices poses safety concerns. While the high voltage lines and surfaces in DEA devices can be properly insulated, the safety of the device should still be investigated in case of a high voltage leakage and electric shock. In this chapter, safety standards for consumer products that establish a safe limit relationship between exposed current amplitude and duration based on ventricular fibrillation were studied.

A simplified circuit model to represent both a DEA in contact with the human body and its related high voltage circuit was considered. By considering the worst-case in which the human body was modeled with a  $500\Omega$  resistance, three possible hazardous scenarios were studied. Each of the three scenarios was discussed to provide general safety measures based on the UL safety standard. It was discussed that, in general, the current from the high voltage power supply should be limited to 20mA. It was shown that the worst-case hazard scenario could happen when a charged DEA connected to its high voltage power supply is touched. In this case, the current discharged through the human body should be limited by the charging voltage, the capacitance of the DEA and the resistance loads in the circuit. Based on the UL safety standard, a relationship and a graph for a critical capacitance were found as a function of charging voltage and load resistance. It was discussed that the DEA capacitances smaller than the critical capacitance were safe. It was noted that DEAs undergo substantial capacitance changes and a DEA yields the maximum capacitance when it is maximally stretched and actuated. Hence, for a DEA, this maximum capacitance should be less than the introduced critical capacitance to ensure safety. Subsequently, relationships between the geometrical parameters of the DEA and the critical capacitance were introduced. These relationships could be used in the design procedure of DEAs to create capacitances below the critical capacitance to satisfy the UL safety standard. Two common geometrical configurations of DEAs, namely planar and cylindrical DEAs, which are the building blocks of many DEA devices, were studied.

To verify the proposed DEA discharge model, an experimental circuit was designed to charge DEA samples up to 2.8 kV and then discharge to a resistor representing the human body. Utilizing this circuit, two planar DEAs under arbitrary stretch ratios of 1.0, 1.1, 1.2, and 1.3 were studied for their total amount of discharge to a  $500\Omega$  resistance. It was shown that the total amount of discharge in these stretches were well below the UL standard. In addition, using this circuit a procedure for measuring the series and parallel resistance of DEAs were proposed.

To illustrate the advantage of the proposed safety measure, a case study of a DEA-based biomedical device was investigated. In this case study, a DEA with planar and cylindrical configurations was considered. Based on the safety design procedure that was developed in the chapter, safe geometrical dimensions were calculated for the DEA.

## Chapter 7.

### Conclusion

The general goal of this Ph.D. thesis was to explore cylindrical DEAs for real-life and practical applications, particularly, for applications where some sort of compressive force could be achieved using cylindrical DEAs. This goal was met by addressing the following three main objectives:

OBJECTIVE 1: Identify compression modalities of cylindrical DEAs

OBJECTIVE 2: Use the first modality identified in OBJECTIVE 1, i.e. negative active pressure, for a realistic application (Active compression bandage for the human lower leg)

OBJECTIVE 3: Use the second modality identified in OBJECTIVE 1, i.e. positive active pressure, for a realistic application (Robotic soft grasping gripper)

OBJECTIVE 4: Identify conditions to operate DEAs safely when operated in proximity to the human body.

OBJECTIVE 2 was addressed by setting two sub-objectives:

2.1. Designing a DEA-based ACB by characterizing its performance through mathematical simulations and experiments; and

2.2. Considering the interaction of the ACB with the flexible and compliant human lower extremity.

OBJECTIVE 2.1. was addressed in Chapter 3 by designing and prototyping DEA-based bandages that were capable of applying passive and active compression when wrapped around a cylindrical body. When wrapped around on a cylindrical body, the DEA bandages were designed to apply a passive compression which was reduced by activating the DEA using a high voltage stimulus. Prototypes were designed based on geometrical properties of the human lower leg and passive compression levels of typical compression stockings to investigate and observe the potential application of the DEA bandages for use in compression therapy. Particularly, the prototypes were designed to conform lower

leg sections and apply compression levels similar to mildest compression stockings from 15mmHg at the ankle to 20mmHg at the knee.

Analytical equations representing the amount of active and passive compression of DEA bandages around a cylindrical body were developed to provide insights for designing the prototypes. Besides analytical equations, FEM models, which generally provide improved geometrical representation, were developed to simulate the performance of the DEA bandage. An experimental procedure was developed to perform experimental analysis on the prototyped DEA bandages. The experimental results verified the validity of analytical and FEM simulations. The validated mathematical models were used to further simulate the performance of the DEA bandage by varying several parameters of the DEAs.

OBJECTIVE 2.2. was met in Chapter 4 by analyzing the behavior of an ACB on the flexible human lower leg. Mathematical models representing the compliance of human leg to external compression were obtained from the literature. The obtained mathematical models were coupled to the validated ACB models from Chapter 3 to simulate the behavior of ACB on the human lower leg. Both analytical and FEM simulations were developed. Results of the simulations showed that the volumetric changes of the lower leg upon application of external compression could be considerable and in fact, these volumetric changes affect the eventual amount of applied external compression by ACB. Thus, it was discussed that to properly design a DEA-based ACB for potential use in compression therapy, the size and compressibility of the human leg should be considered. Chapter 4 presented mathematical models to carry out such design considerations.

OBJECTIVE 3 was achieved in Chapter 5 by proposing a gripper configuration based on cylindrical DEAs for potential application in soft-touch grasping particularly for grasping delicate objects. The proposed gripper configuration included a chamber enclosed by a cylindrical DEA membrane which is initially passively inflated and could change its inflation by activating the DEA, the active inflation ultimately resulting in grasping an object. The proposed gripper was designed and prototyped to analyze the performance and functionality of the gripper in experimental set-ups. Two test procedures were developed to characterize the DEA inflation in the gripper and the amount of grasping force on certain objects.

Mathematical equations were constructed to represent the behavior of the DEA membrane within the boundary conditions defined by the gripper configuration. Mathematical simulation successfully anticipated the experimental results in the passive and active inflation of the DEA membrane and the amount of applied force to an encompassing object. The proposed gripper design successfully showed up to 2N of grasping force which is comparable with other proposed DEA based grippers.

Finally, OBJECTIVE 4 was met in Chapter 6 by investigating the electrical safety of DEAs in applications where a DEA, particularly in planar and cylindrical configurations, is operated in proximity to the human body which may be the case either for DEA-based compression bandages (OBJECTIVE 2) and soft grasping grippers (OBJECTIVE 3). Three possible scenarios of electrical discharge from a DEA circuitry to a human body were discussed and UL safety standard was used as a basis to provide general safety measures for each scenario.

In accordance with UL safety standard It was argued that, at all times, the current from the high voltage power supply of a DEA should be limited to 20mA. It was shown that the worst-case hazard scenario could happen when a charged DEA connected to its high voltage power supply is exposed to the human body. Based on the UL safety standard, a criterion for a critical capacitance of a DEA was found as a function of charging voltage and load resistance. It was discussed that the DEA capacitances smaller than the critical capacitance were safe. Subsequently, relationships between the geometrical parameters of a DEA and the critical capacitance were introduced. These relationships could be used in the design procedure of DEAs to create capacitances below the critical capacitance to satisfy the UL safety standard.

In Chapter 6, to illustrate the use of the developed safety measures, a case study of a DEA-based ACB (based on Chapter 3) was considered. The safety design procedure was used to obtain safe geometrical dimensions for the bandage to ensure electrical safety in case the ACB is exposed to the human body.

Although the presented work provided a considerable contribution toward the proposed DEA-based devices, it is noted that the investigated technologies are still in the early stage of development and certain limitations exist. Both designed devices, the ACB, and the soft grasping gripper provided specific limitations that were already discussed in

chapters 3, 4, and 5. Particularly, it was discussed that the stress relaxation in the DEA membrane may considerably affect the performance of the ACB and result in generating undesirable compression levels. This limitation could be addressed by considering DEA material relaxation in the design of the ACB. Readily available mathematical models in the literature that model the relaxation behavior of DEA membranes could be adapted and integrated with the developed models in this work to improve mathematical driven simulations and designs.

The soft grasping gripper required an initial pressure inside the chamber which should be carefully adjusted offline based on the size of the grasping object. This limitation could be addressed by using snap-through instability in the actuation of the DEA membrane to provide a wider range of actuation deformations and/or connecting the gripper's chamber to a pressurized reservoir using a controlled air valve to enable online adjustment of the gripper's opening.

Further future work directions could include improving the actuation performance of the DEA bandage and gripper membrane to generate larger pressure variations around a cylindrical body. This improvement could be achieved by choosing optimal geometrical parameters for the DEA and stacking multiple DEAs into one membrane.

Furthermore, the operation of the proposed devices could be improved by designing a controller to provide electrical input to the DEAs. Optimal controllers may be designed for both the ACB and the soft grasping gripper using control theory algorithms to enable the desired actuation of the DEA devices. As a preliminary work toward this improving aspect, a nonlinear controller is designed and proposed to track and set the applied compression levels of an ACB on the flexible human lower leg. This preliminary work is presented in Appendix A of this thesis.

## References

- [1] S. M. Mirvakili, A. Pazukha, W. Sikkema, C. W. Sinclair, G. M. Spinks, R. H. Baughman, and J. D. W. Madden, "Niobium Nanowire Yarns and their Application as Artificial Muscles," *Adv. Funct. Mater.*, Sep. 2013, **23**, no. 35, pp. 4311–4316.
- [2] Y. Bar-Cohen, *Electroactive Polymer (EAP) Actuators as Artificial Muscles: Reality, Potential, and Challenges, Second Edition*, 2nd ed. Bellingham, WA: SPIE Optical Engineering Press, 2004.
- [3] Y. Bar-Cohen and Q. Zhang, "Electroactive Polymer Actuators and Sensors," *MRS Bull.*, Mar. 2008, **33**, no. 03, pp. 173–181.
- [4] F. Carpi, C. Menon, and D. De Rossi, "Electroactive Elastomeric Actuator for All-Polymer Linear Peristaltic Pumps," *IEEE/ASME Trans. Mechatronics*, Jun. 2010, **15**, no. 3, pp. 460–470.
- [5] G.-Y. Gu, J. Zhu, L.-M. Zhu, and X. Zhu, "A survey on dielectric elastomer actuators for soft robots," *Bioinspir. Biomim.*, 2017, **12**, no. 1, p. 011003.
- [6] C. Majidi, "Soft Robotics: A Perspective—Current Trends and Prospects for the Future," *Soft Robot.*, Mar. 2014, **1**, no. 1, pp. 5–11.
- [7] G. M. Whitesides, "Soft Robotics," *Angewandte Chemie - International Edition*, **57**, no. 16. John Wiley & Sons, Ltd, pp. 4258–4273, 09-Apr-2018.
- [8] S. Pourazadi, S. Ahmadi, and C. Menon, "Towards the development of active compression bandages using dielectric elastomer actuators," *Smart Mater. Struct.*, Jun. 2014, **23**, no. 6, p. 065007.
- [9] S. Pourazadi, S. Ahmadi, and C. Menon, "On the design of a DEA-based device to potentially assist lower leg disorders: An analytical and FEM investigation accounting for nonlinearities of the leg and device deformations," *Biomed. Eng. Online*, 2015, **14**, no. 1.
- [10] S. Pourazadi, M. Moallem, and C. Menon, "Nonlinear Control and Simulation of a Dielectric Elastomer Actuator-Based Compression Bandage on Flexible Human Calf," in *International Conference on Bioinformatics and Biomedical Engineering*, 2017, pp. 289–300.
- [11] S. Pourazadi, H. Bui, and C. Menon, "Investigation on a soft grasping gripper based on dielectric elastomer actuators," *Smart Mater. Struct.*, Feb. 2019, **28**, no. 3.
- [12] S. Pourazadi, A. Shagerdmootaab, H. Chan, M. Moallem, and C. Menon, "On the Electrical Safety of Dielectric Elastomer Actuators in Proximity to the Human Body," *Smart Mater. Struct.*, 2017, **305**, no. 1–3, pp. 54–57.

- [13] R. Kornbluh, R. Pelrine, Q. Pei, R. Heydt, S. Stanford, S. Oh, J. Eckerle, S. R. I. International, R. Avenue, and M. Park, "Electroelastomers : Applications of Dielectric Elastomer Transducers for Actuation , Generation and Smart Structures," *Proc. SPIE 4698, Smart Struct. Mater. 2002 Ind. Commer. Appl. Smart Struct. Technol.*, 2002, **4698**, pp. 254–270.
- [14] H. Zhang, L. Düring, G. Kovacs, W. Yuan, X. Niu, and Q. Pei, "Interpenetrating polymer networks based on acrylic elastomers and plasticizers with improved actuation temperature range," *Polym. Int.*, 2010, **59**, no. 3, pp. 384–390.
- [15] P. Brochu and Q. Pei, "Advances in Dielectric Elastomers for Actuators and Artificial Muscles," *Macromol. Rapid Commun.*, Jan. 2010, **31**, no. 1, pp. 10–36.
- [16] F. Carpi, D. De Rossi, R. Kornbluh, R. Pelrine, and P. Sommer-Larsen, *Dielectric elastomers as electromechanical transducers: Fundamentals, Materials, Devices, Models and Applications of an Emerging Electroactive Polymer Technology*. Elsevier, 2008.
- [17] R. Shankar, T. K. Ghosh, and R. J. Spontak, "Dielectric elastomers as next-generation polymeric actuators," *Soft Matter*, 2007, **3**, no. 9, p. 1116.
- [18] A. O'Halloran, F. O'Malley, and P. McHugh, "A review on dielectric elastomer actuators, technology, applications, and challenges," *J. Appl. Phys.*, 2008, **104**, no. 7, p. 071101.
- [19] F. Carpi, D. De Rossi, R. Kornbluh, R. Pelrine, and P. Sommer-Larse, *Dielectric Elastomers as Electromechanical Transducers*. Amsterdam: Elsevier, 2008.
- [20] L. Meunier, G. Chagnon, D. Favier, L. Orgéas, and P. Vacher, "Mechanical experimental characterisation and numerical modelling of an unfilled silicone rubber," *Polym. Test.*, 2008, **27**, no. 7, pp. 765–777.
- [21] S. Michel, X. Q. Zhang, M. Wissler, C. Löwe, and G. Kovacs, "A comparison between silicone and acrylic elastomers as dielectric materials in electroactive polymer actuators," *Polym. Int.*, Dec. 2009, **59**, no. 3, pp. 391–399.
- [22] R. Pelrine, R. Kornbluh, Q. Pei, and J. Joseph, "High-Speed Electrically Actuated Elastomers with Strain Greater Than 100%," *Science (80-. )*, Feb. 2000, **287**, no. 5454, pp. 836–839.
- [23] F. Carpi, P. Chiarelli, A. Mazzoldi, and D. De Rossi, "Electromechanical characterisation of dielectric elastomer planar actuators: Comparative evaluation of different electrode materials and different counterloads," *Sensors Actuators, A Phys.*, 2003, **107**, no. 1, pp. 85–95.
- [24] Q. Pei, R. Pelrine, M. A. Rosenthal, S. Stanford, H. Prahlad, and R. D. Kornbluh, "Recent progress on electroelastomer artificial muscles and their application for biomimetic robots," 2004, p. 41.

- [25] Q. Pei, M. a. Rosenthal, R. Pelrine, S. Stanford, and R. D. Kornbluh, "Multifunctional electroelastomer roll actuators and their application for biomimetic walking robots," *SPIE Smart Struct. Mater.*, 2003, **5051**, pp. 281–290.
- [26] G.-K. Lau, H.-T. Lim, J.-Y. Teo, and Y.-W. Chin, "Lightweight mechanical amplifiers for rolled dielectric elastomer actuators and their integration with bio-inspired wing flappers," *Smart Mater. Struct.*, Feb. 2014, **23**, no. 2, p. 025021.
- [27] S. Ahmadi, a Camacho Mattos, a Barbazza, M. Soleimani, P. Boscaroli, and C. Menon, "Fabrication and performance analysis of a DEA cuff designed for dry-suit applications," *Smart Mater. Struct.*, Mar. 2013, **22**, no. 3, p. 035002.
- [28] F. Carpi, A. Migliore, G. Serra, and D. De Rossi, "Helical dielectric elastomer actuators," *Smart Mater. Struct.*, Dec. 2005, **14**, no. 6, pp. 1210–1216.
- [29] F. Carpi and D. De Rossi, "Small-Strain Modeling of Helical Dielectric Elastomer Actuators," *IEEE/ASME Trans. Mechatronics*, Apr. 2012, **17**, no. 2, pp. 318–325.
- [30] S. Ahmadi, M. Gooyers, M. Soleimani, and C. Menon, "Fabrication and electromechanical examination of a spherical dielectric elastomer actuator," *Smart Mater. Struct.*, 2013, **22**, no. 11, p. 115004.
- [31] M. Artusi, M. Potz, J. Aristizabal, C. Menon, S. Cocuzza, and S. Debei, "Electroactive Elastomeric Actuators for the Implementation of a Deformable Spherical Rover," *IEEE/ASME Trans. Mechatronics*, Feb. 2011, **16**, no. 1, pp. 50–57.
- [32] D. McCoul and Q. Pei, "Tubular dielectric elastomer actuator for active fluidic control," *Smart Mater. Struct.*, Sep. 2015, **24**, no. 10, p. 105016.
- [33] R. Pelrine, R. Kornbluh, J. Joseph, R. Heydt, Q. Pei, and S. Chiba, "High-field deformation of elastomeric dielectrics for actuators," *Mater. Sci. Eng.*, 2000, **11**, no. 2, pp. 89–100.
- [34] G. Kofod, M. Paajanen, and S. Bauer, "New design concept for dielectric elastomer actuators," *Electroact. Polym. Actuators Devices*, Mar. 2006, **6168**, pp. 689–697.
- [35] J. D. W. Madden, N. A. Vandesteeg, P. A. Anquetil, P. G. A. Madden, A. Takshi, R. Z. Pytel, S. R. Lafontaine, P. A. Wieringa, and I. W. Hunter, "Artificial muscle technology: Physical principles and naval prospects," *IEEE J. Ocean. Eng.*, Jul. 2004, **29**, no. 3, pp. 706–728.
- [36] F. B. Madsen, A. E. Daugaard, S. Hvilsted, and A. L. Skov, "The Current State of Silicone-Based Dielectric Elastomer Transducers," *Macromolecular Rapid Communications*, **37**, no. 5, pp. 378–413, 01-Mar-2015.
- [37] P. Lotz, M. Matysek, and H. F. Schlaak, "Fabrication and Application of

- Miniaturized Dielectric Elastomer Stack Actuators,” *IEEE/ASME Trans. Mechatronics*, Feb. 2011, **16**, no. 1, pp. 58–66.
- [38] S. Rosset, O. A. Araromi, S. Schlatter, and H. R. Shea, “Fabrication Process of Silicone-based Dielectric Elastomer Actuators,” *J. Vis. Exp.*, Feb. 2016, no. 108, p. e53423.
- [39] O. A. Araromi, I. Gavrilovich, J. Shintake, S. Rosset, M. Richard, V. Gass, and H. R. Shea, “Rollable Multisegment Dielectric Elastomer Minimum Energy Structures for a Deployable Microsatellite Gripper,” *IEEE/ASME Trans. Mechatronics*, Feb. 2015, **20**, no. 1, pp. 438–446.
- [40] R. Sarban, R. W. Jones, B. R. MacE, and E. Rustighi, “A tubular dielectric elastomer actuator: Fabrication, characterization and active vibration isolation,” *Mechanical Systems and Signal Processing*, **25**, no. 8, pp. 2879–2891, 2011.
- [41] S. Reitelshöfer, M. Göttler, P. Schmidt, P. Treffer, M. Landgraf, and J. Franke, “Aerosol-Jet-Printing silicone layers and electrodes for stacked dielectric elastomer actuators in one processing device,” *Proc. SPIE 9798, Electroact. Polym. Actuators Devices 2016*, 2016, **9798**, no. 0, pp. 8–16.
- [42] J. Rossiter, P. Walters, and B. Stoimenov, “Printing 3D dielectric elastomer actuators for soft robotics,” 2009, **7287**, p. 72870H.
- [43] F. Carpi, C. Salaris, and D. De Rossi, “Folded dielectric elastomer actuators,” *Smart Mater. Struct.*, 2007, **16**, no. 2, pp. S300–S305.
- [44] F. Carpi and D. De Rossi, “Dielectric elastomer cylindrical actuators: Electromechanical modelling and experimental evaluation,” *Mater. Sci. Eng. C*, Jun. 2004, **24**, no. 4, pp. 555–562.
- [45] S. Rosset and H. R. Shea, “Flexible and stretchable electrodes for dielectric elastomer actuators,” *Appl. Phys. A*, Nov. 2012, **110**, no. 2, pp. 281–307.
- [46] K. Jung, K. J. Kim, and H. R. Choi, “A self-sensing dielectric elastomer actuator,” *Sensors Actuators A Phys.*, May 2008, **143**, no. 2, pp. 343–351.
- [47] L. A. Toth and A. A. Goldenberg, “Control system design for a dielectric elastomer actuator: the sensory subsystem,” in *Proceedings Volume 4695, Smart Structures and Materials 2002: Electroactive Polymer Actuators and Devices (EAPAD)*, 2002, **4695**, pp. 323–334.
- [48] H. F. Schlaak, M. Jungmann, M. Matysek, and P. Lotz, “Novel Multilayer Electrostatic Solid State Actuators with Elastic Dielectric,” *Proc. SPIE*, 2005, **5759**, pp. 121–133.
- [49] M. Aschwanden and A. Stemmer, “Low voltage, highly tunable diffraction grating based on dielectric elastomer actuators,” in *Proceedings Volume 6524*,

*Electroactive Polymer Actuators and Devices (EAPAD) 2007*, 2007, **6524**, p. 65241N.

- [50] S. Rosset, M. Niklaus, P. Dubois, and H. R. Shea, "Mechanical characterization of a dielectric elastomer microactuator with ion-implanted electrodes," *Sensors Actuators, A Phys.*, 2008, **144**, no. 1, pp. 185–193.
- [51] A. Poulin, S. Rosset, and H. Shea, "Fully printed 3 microns thick dielectric elastomer actuator," 2016, **9798**, pp. 1–11.
- [52] D. J. Griffiths, *Introduction to Electrodynamics*, 3rd ed. Upper Saddle River, New Jersey: Prentice-Hall, 1999.
- [53] I. M. Koo, K. Jung, J. C. Koo, J. Do Nam, Y. K. Lee, and H. R. Choi, "Development of soft-actuator-based wearable tactile display," *IEEE Trans. Robot.*, 2008, **24**, no. 3, pp. 549–558.
- [54] H. Edher, L. Maupas, S. Nijjer, and A. Salehian, "Utilizing tension reduction in a dielectric elastomer actuator to produce compression for physiological application," *J. Intell. Mater. Syst. Struct.*, Mar. 2018, **29**, no. 5, pp. 998–1011.
- [55] M. T. Wissler, "Modeling Dielectric Elastomer Actuators," ETH, 2007.
- [56] G. Kofod, "Dielectric elastomer actuators," Risø National Laboratory, 2001.
- [57] Z. Suo, "Theory of dielectric elastomers," *Acta Mech. Solida Sin.*, 2010, **23**, no. 6.
- [58] Y. Bar-Cohen, "Electroactive Polymers as Artificial Muscles: Capabilities, Potentials and Challenges," in *Robotics 2000*, 2000, pp. 188–196.
- [59] C. Menon, F. Carpi, and D. De Rossi, "Concept design of novel bio-inspired distributed actuators for space applications," *Acta Astronaut.*, Sep. 2009, **65**, no. 5–6, pp. 825–833.
- [60] J. Shintake, S. Rosset, B. Schubert, D. Floreano, and H. Shea, "Versatile Soft Grippers with Intrinsic Electro-adhesion Based on Multifunctional Polymer Actuators," *Adv. Mater.*, 2016, **28**, no. 2, pp. 231–238.
- [61] K. Wei, N. W. Domicone, and Y. Zhao, "Electroactive liquid lens driven by an annular membrane," *Opt. Lett.*, Mar. 2014, **39**, no. 5, p. 1318.
- [62] T. Lewis, "A lecture on vasovagal syncope and the carotid sinus mechanism," *Br. Med. J.*, 1932, **1**, no. 932, p. 873.
- [63] M. B. Stenger, A. K. Brown, S. M. C. Lee, J. P. Locke, and S. H. Platts, "Gradient Compression Garments as a Countermeasure to Post-Spaceflight Orthostatic Intolerance," *Aviat. Space. Environ. Med.*, Sep. 2010, **81**, no. 9, pp. 883–887.

- [64] C. Burrows, R. Miller, D. Townsend, R. Bellefontaine, G. Mackean, H. L. Orsted, and D. H. Keast, "Best practice recommendations for the prevention and treatment of venous leg ulcers : update 2006," *Adv. Skin Wound Care*, 2006, **20**, pp. 611–621.
- [65] A. Ramelet, "Compression therapy," *Dermatologic Surg.*, 2002, **28**, pp. 6–10.
- [66] C. L. Protheroe, A. Dikareva, C. Menon, and V. E. Claydon, "Are compression stockings an effective treatment for orthostatic presyncope?," *PLoS One*, Jan. 2011, **6**, no. 12, p. e28193.
- [67] C. A. Latz, K. R. Brown, and R. L. Bush, "Compression therapies for chronic venous leg ulcers : interventions and adherence," *Chronic Wound Care Manag. Res.*, Jan. 2015, **2**, pp. 11–21.
- [68] J. M. Krahn, F. Fabbro, and C. Menon, "A soft-touch gripper for grasping delicate objects," *IEEE/ASME Trans. Mechatronics*, Jun. 2017, **22**, no. 3, pp. 1276–1286.
- [69] F. Ilievski, A. D. Mazzeo, R. F. Shepherd, X. Chen, and G. M. Whitesides, "Soft robotics for chemists," *Angew. Chemie - Int. Ed.*, 2011, **50**, no. 8, pp. 1890–1895.
- [70] R. Deimel and O. Brock, "A compliant hand based on a novel pneumatic actuator," in *Proceedings - IEEE International Conference on Robotics and Automation*, 2013, pp. 2047–2053.
- [71] M. E. Giannaccini, I. Georgilas, I. Horsfield, B. H. P. M. Peiris, A. Lenz, A. G. Pipe, and S. Dogramadzi, "A variable compliance, soft gripper," *Auton. Robots*, Jan. 2014, **36**, no. 1–2, pp. 93–107.
- [72] H. Choi and M. Koç, "Design and feasibility tests of a flexible gripper based on inflatable rubber pockets," *Int. J. Mach. Tools Manuf.*, Oct. 2006, **46**, no. 12–13, pp. 1350–1361.
- [73] J. R. Amend, E. Brown, N. Rodenberg, H. M. Jaeger, and H. Lipson, "A positive pressure universal gripper based on the jamming of granular material," *IEEE Trans. Robot.*, Apr. 2012, **28**, no. 2, pp. 341–350.
- [74] E. Brown, N. Rodenberg, J. Amend, A. Mozeika, E. Steltz, M. R. Zakin, H. Lipson, and H. M. Jaeger, "Universal robotic gripper based on the jamming of granular material," *Proc. Natl. Acad. Sci.*, Nov. 2010, **107**, no. 44, pp. 18809–18814.
- [75] R. Kolluru, K. P. Valavanis, and T. M. Hebert, "Modeling, analysis, and performance evaluation of a robotic gripper system for limp material handling," *IEEE Transactions on Systems, Man, and Cybernetics, Part B: Cybernetics*, **28**, no. 3, pp. 480–486, Jun-1998.
- [76] J. Shintake, B. Schubert, S. Rosset, H. Shea, and D. Floreano, "Variable stiffness actuator for soft robotics using dielectric elastomer and low-melting-point alloy," in

2015 IEEE/RSJ International Conference on Intelligent Robots and Systems (IROS), 2015, **2015-Decem**, pp. 1097–1102.

- [77] F. Carpi, G. Frediani, C. Gerboni, J. Gemignani, and D. De Rossi, “Enabling variable-stiffness hand rehabilitation orthoses with dielectric elastomer transducers.,” *Med. Eng. Phys.*, Feb. 2014, **36**, no. 2, pp. 205–11.
- [78] Rui Zhang, A. Kunz, P. Lochmatter, and G. Kovacs, “Dielectric Elastomer Spring Roll Actuators for a Portable Force Feedback Device,” in *2006 14th Symposium on Haptic Interfaces for Virtual Environment and Teleoperator Systems*, 2006, pp. 347–353.
- [79] J. P. Reilly, *Applied Bioelectricity : From Electrical Stimulation to Electropathology*. Springer New York, 1998.
- [80] A. J. Nimunkar and J. G. Webster, “Safety of pulsed electric devices.,” *Physiol. Meas.*, Jan. 2009, **30**, no. 1, pp. 101–14.
- [81] O. Z. Roy and A. S. Podgorski, “Tests on a shocking device—the stun gun,” *Med. Biol. Eng. Comput.*, Jul. 1989, **27**, no. 4, pp. 445–448.
- [82] M. N. Robinson, C. G. Brooks, and G. D. Renshaw, “Electric shock devices and their effects on the human body.,” *Med. Sci. Law*, 1990, **30**, no. 4, pp. 285–300.
- [83] W. C. McDaniel, R. A. Stratbucker, M. Nerheim, and J. E. Brewer, “Cardiac Safety of Neuromuscular Incapacitating Defensive Devices,” *Pacing Clin. Electrophysiol.*, Jan. 2005, **28**, no. s1, pp. S284–S287.
- [84] G. Kovacs, P. Lochmatter, and M. Wissler, “An arm wrestling robot driven by dielectric elastomer actuators,” *Smart Mater. Struct.*, Apr. 2007, **16**, no. 2, pp. S306–S317.
- [85] R. Hainsworth, “Pathophysiology of syncope.,” *Clin. Auton. Res.*, Oct. 2004, **14 Suppl 1**, pp. 18–24.
- [86] S. Pierson, D. Pierson, R. Swallow, and G. Johnson, “Efficacy of graded elastic compression in the lower leg.,” *JAMA*, Jan. 1983, **249**, no. 2, pp. 242–3.
- [87] N. A. G. Jones, P. J. Webb, R. I. Rees, and V. V Kakkar, “A physiological study of elastic compression stockings in venous disorders of the leg.,” *Br. J. Surg.*, 1980, **67**, no. 8, pp. 569–572.
- [88] D. P. Brandjes, H. R. Büller, H. Heijboer, M. V Huisman, M. de Rijk, H. Jagt, and J. W. ten Cate, “Randomised trial of effect of compression stockings in patients with symptomatic proximal-vein thrombosis.,” *Lancet*, Mar. 1997, **349**, no. 9054, pp. 759–62.
- [89] J. S. Ginsberg, J. Hirsh, J. Julian, M. Vander LaandeVries, D. Magier, B.

- MacKinnon, and M. Gent, "Prevention and treatment of postphlebotic syndrome: results of a 3-part study.," *Arch. Intern. Med.*, 2001, **161**, no. 17, pp. 2105–9.
- [90] A. O. Kanaan, J. E. Lepage, S. Djazayeri, and J. L. Donovan, "Evaluating the Role of Compression Stockings in Preventing Post thrombotic Syndrome: A Review of the Literature.," *Thrombosis*, Jan. 2012, **2012**, p. 694851.
- [91] Y. Silbersack, B.-M. Taute, W. Hein, and H. Podhaisky, "Prevention of deep-vein thrombosis after total hip and knee replacement," *J. Bone Jt. Surg.*, Aug. 2004, **86**, no. 6, pp. 809–812.
- [92] L. R. Pedegana, E. M. Burgess, a J. Moore, and M. L. Carpenter, "Prevention of thromboembolic disease by external pneumatic compression in patients undergoing total hip arthroplasty," *Clin. Orthop. Relat. Res.*, 1977, **128**, pp. 190–193.
- [93] L. Walker and S. Lamont, "The use of antiembolic stockings. Part 1: a literature review," *Br. J. Nurs.*, 2007, **2**, no. 22, pp. 1408–1413.
- [94] [Http://www.velcro.com/](http://www.velcro.com/), "Velcro." [Online]. Available: <http://www.velcro.com/>.
- [95] R. J. Morris and J. P. Woodcock, "Intermittent pneumatic compression or graduated compression stockings for deep vein thrombosis prophylaxis? A systematic review of direct clinical comparisons.," *Ann. Surg.*, Mar. 2010, **251**, no. 3, pp. 393–6.
- [96] S. Watanuki and H. Murata, "Effects of wearing compression stockings on cardiovascular responses," *Ann. Physiol. Anthropol.*, 1994, **13**, no. 3, pp. 121–127.
- [97] A. Ali, M. Hosseini, and B. B. Sahari, "A review of constitutive models for rubber-like materials," *Am. J. Eng. Appl. Sci.*, 2010, **3**, no. 1, pp. 232–239.
- [98] R. W. Ogden, "Large deformation isotropic elasticity - on the correlation of theory and experiment for incompressible rubberlike solids," 1972, **326**, no. 1567, pp. 565–584.
- [99] N. J. Fuller, C. R. Hardingham, M. Graves, N. Screamon, a K. Dixon, L. C. Ward, and M. Elia, "Predicting composition of leg sections with anthropometry and bioelectrical impedance analysis, using magnetic resonance imaging as reference.," *Clin. Sci. (Lond)*., Jun. 1999, **96**, no. 6, pp. 647–57.
- [100] P. Karakaş and M. G. Bozkir, "Determination of normal calf and ankle values among medical students.," *Aesthetic Plast. Surg.*, 2007, **31**, no. 2, pp. 179–82.
- [101] [Www.bjbenterprises.com/](http://www.bjbenterprises.com/), "TC-5005 BJB Enterprises," 2013. [Online]. Available: [www.bjbenterprises.com/](http://www.bjbenterprises.com/).

- [102] [www.sigvarisusa.com](http://www.sigvarisusa.com), "Sigvaris Compression Stocking." [Online]. Available: [www.sigvarisusa.com](http://www.sigvarisusa.com).
- [103] [www.ansys.com](http://www.ansys.com), "ANSYS Workbench." ANSYS Inc., 2011.
- [104] K. G. Burnand and L. G. T, "Graduted elastic stockings," *Br. Med. J.*, 1986, **293**, no. July, pp. 224–225.
- [105] Y. Silbersack, B.-M. Taute, W. Hein, and H. Podhaisky, "Prevention of deep-vein thrombosis after total hip and knee replacement," *J. Bone Jt. Surg.*, Aug. 2004, **86**, no. 6, pp. 809–812.
- [106] R. Stemmer, "Ambulatory elasto-compressive treatment of the lower extrimities particularly with elastic stokcings," *Der Kassenarzt*, 1969, **9**, pp. 1–8.
- [107] B. Sigel, A. Edelestein, L. Savitch, J. Hasty, and W. Felix, "Types of compression for reducing venous stasis," *Arch. Surg.*, 1975, **110**, pp. 171–5.
- [108] J. R. Halliwill, C. T. Minson, M. J. Joyner, and R. John, "Measurement of limb venous compliance in humans: technical considerations and physiological findings," *J. Appl. Physiol.*, 1999, **87**, no. 4, pp. 1555–1563.
- [109] K. D. Monahan, F. a Dinunno, D. R. Seals, and J. R. Halliwill, "Smaller age-associated reductions in leg venous compliance in endurance exercise-trained men.," *Am. J. Physiol. Heart Circ. Physiol.*, Sep. 2001, **281**, no. 3, pp. H1267-73.
- [110] K. D. Monahan and C. a Ray, "Gender affects calf venous compliance at rest and during baroreceptor unloading in humans.," *Am. J. Physiol. Heart Circ. Physiol.*, Mar. 2004, **286**, no. 3, pp. H895-901.
- [111] a Lipp, P. Sandroni, J. E. Ahlskog, D. M. Maraganore, C. W. Shults, and P. a Low, "Calf venous compliance in multiple system atrophy.," *Am. J. Physiol. Heart Circ. Physiol.*, 2007, **293**, no. 1, pp. H260-5.
- [112] J. a Sielatycki, S. Shamimi-Noori, M. P. Pfeiffer, and K. D. Monahan, "Adrenergic mechanisms do not contribute to age-related decreases in calf venous compliance," *J. Appl. Physiol.*, 2011, **110**, no. 1, pp. 29–34.
- [113] T. Binzoni, V. Quaresima, M. Ferrari, E. Hiltbrand, and P. Cerretelli, "Human calf microvascular compliance measured by near-infrared spectroscopy.," *J. Appl. Physiol.*, 2000, **88**, no. 2, pp. 369–372.
- [114] M. Zicot, K. H. Parker, and C. G. Caro, "Effect of positive external pressure on calf volume and local venous haemodynamics.," *Phys. Med. Biol.*, 1977, **22**, no. 6, pp. 1146–1159.
- [115] R. B. Thirsk, R. D. Kamm, and a H. Shapiro, "Changes in venous blood volume produced by external compression of the lower leg.," *Med. Biol. Eng. Comput.*,

Sep. 1980, **18**, no. 5, pp. 650–6.

- [116] R. J. Whitney, “The measurement of volume changes in human limbs,” *J. Physiol.*, 1953, **121**, no. 1, pp. 1–27.
- [117] R. B. Thirsk, R. D. Kamm, and A. H. Shapiro, “Changes in venous blood volume produced by external compression of the lower leg,” *Med. Biol. Eng. Comput.*, 1980, **18**, no. 5, pp. 650–656.
- [118] A. Hoyos and P. Prendergast, *Complications of High-Definition Body Sculpting*. Berlin: Springer, 2014.
- [119] M. Wissler and E. Mazza, “Modeling and simulation of dielectric elastomer actuators,” *Smart Mater. Struct.*, 2005, **14**, no. 6, p. 1396.
- [120] “Boa closure system.” [Online]. Available: <http://www.boatechnology.com>.
- [121] D. Trivedi, C. D. Rahn, W. M. Kier, and I. D. Walker, “Soft robotics: Biological inspiration, state of the art, and future research,” *Appl. Bionics Biomech.*, Dec. 2008, **5**, no. 3, pp. 99–117.
- [122] D. Rus and M. T. Tolley, “Design, fabrication and control of soft robots Terms of Use Design, fabrication and control of soft robots,” *Nature*, 2015, **521**, no. 7553, pp. 467–475.
- [123] R. Lumia and M. Shahinpoor, “IPMC microgripper research and development,” *J. Phys. Conf. Ser.*, 2008, **127**, p. 012002.
- [124] J. W. Fox and N. C. Goulbourne, “On the dynamic electromechanical loading of dielectric elastomer membranes,” *J. Mech. Phys. Solids*, Aug. 2008, **56**, no. 8, pp. 2669–2686.
- [125] J. Zhu, S. Cai, and Z. Suo, “Resonant behavior of a membrane of a dielectric elastomer,” *Int. J. Solids Struct.*, Dec. 2010, **47**, no. 24, pp. 3254–3262.
- [126] C. Keplinger, T. Li, R. Baumgartner, Z. Suo, and S. Bauer, “Harnessing snap-through instability in soft dielectrics to achieve giant voltage-triggered deformation,” *Soft Matter*, Dec. 2012, **8**, no. 2, pp. 285–288.
- [127] P. Dubois, S. Rosset, M. Niklaus, M. Dadras, and H. Shea, “Voltage control of the resonance frequency of dielectric electroactive polymer (DEAP) membranes,” *J. Microelectromechanical Syst.*, 2008, **17**, no. 5, pp. 1072–1081.
- [128] M. Vatankhah-Varnoosfaderani, W. F. M. Daniel, A. P. Zhushma, Q. Li, B. J. Morgan, K. Matyjaszewski, D. P. Armstrong, R. J. Spontak, A. V. Dobrynin, and S. S. Sheiko, “Bottlebrush Elastomers: A New Platform for Freestanding Electroactuation,” *Adv. Mater.*, 2017, **29**, no. 2, pp. 1–7.

- [129] T. Li, C. Keplinger, R. Baumgartner, S. Bauer, W. Yang, and Z. Suo, "Giant voltage-induced deformation in dielectric elastomers near the verge of snap-through instability," *J. Mech. Phys. Solids*, Feb. 2013, **61**, no. 2, pp. 611–628.
- [130] B. Feeny, A. Guran, N. Hinrichs, and K. Popp, "A Historical Review on Dry Friction and Stick-Slip Phenomena," *Appl. Mech. Rev.*, May 1998, **51**, no. 5, p. 321.
- [131] IEC, "Effects of current passing through the human body. Part 2: Special Effects.," *Int. Electrotech. Comm.*, 2006, no. Number IEC 60479-2.
- [132] Cadick, John, Mary Capelli-Schellpfeffer, Dennis Neitzel, and Al Winfield., *Electrical safety handbook*, 3rd ed. New York: McGraw-Hill, 2006.
- [133] R. Zhang, "Development of dielectric elastomer actuators and their implementation in a force feedback interface," ETH Zürich, 2008.
- [134] P. Lochmatter, G. Kovacs, and M. Wissler, "Characterization of dielectric elastomer actuators based on a visco-hyperelastic film model," *Smart Mater. Struct.*, Apr. 2007, **16**, no. 2, pp. 477–486.
- [135] C. Chiang Foo, S. Cai, S. Jin Adrian Koh, S. Bauer, and Z. Suo, "Model of dissipative dielectric elastomers," *J. Appl. Phys.*, Feb. 2012, **111**, no. 3, p. 034102.
- [136] C. Graf, J. Maas, and D. Schapeler, "Energy harvesting cycles based on electro active polymers," *Proc. SPIE 7642, Electroact. Polym. Actuators Devices*, Mar. 2010, **7642**, pp. 764217-764217–12.
- [137] D. Zipse, "Electrical shock hazard due to stray current," *Ind. Commer. Power Syst. Tech. Conf. 1999 IEEE.*, 1999, pp. 6-pp.
- [138] L. Di Lillo, A. Schmidt, A. Bergamini, P. Ermanni, and E. Mazza, "Dielectric and Insulating Properties of an Acrylic DEA Material at High near-DC Electric Fields," *Proc. SPIE 7976, Electroact. Polym. Actuators Devices*, Mar. 2011, **7976**, pp. 79763B-79763B–6.
- [139] S. Hammami, C. Jean-Mistral, F. Jomni, O. Gallot-Lavallée, P. Rain, B. Yanguì, A. Sylvestre, and S. A., "Leakage current and stability of acrylic elastomer subjected to high DC voltage," in *Proc. SPIE 9430, Electroactive Polymer Actuators and Devices (EAPAD)*, 2015, **9430**, pp. 943015-1-943015–8.
- [140] F. Carpi, D. De Rossi, and R. Kornbluh, *Dielectric elastomers as electromechanical transducers: Fundamentals, materials, devices, models and applications of an emerging electroactive polymer*. 2011.
- [141] D. A. Bell, *Fundamentals of electric circuits*, 7. ed. Don Mills, Ont. : Oxford University Press, 2009.

- [142] G. Kofod, P. Sommer-Larsen, R. Kornbluh, and R. Pelrine, "Actuation Response of Polyacrylate Dielectric Elastomers," *J. Intell. Mater. Syst. Struct.*, 2003, **14**, no. 12, pp. 787–793.
- [143] C. Jean-Mistral, a Sylvestre, S. Basrour, and J.-J. Chaillout, "Dielectric properties of polyacrylate thick films used in sensors and actuators," *Smart Mater. Struct.*, Jul. 2010, **19**, no. 7, p. 075019.
- [144] G. Kofod and P. Sommer-Larsen, "Silicone dielectric elastomer actuators: Finite-elasticity model of actuation," *Sensors Actuators, A Phys.*, 2005, **122**, no. 2, pp. 273–283.
- [145] J. S. Plante and S. Dubowsky, "Large-scale failure modes of dielectric elastomer actuators," *Int. J. Solids Struct.*, 2006, **43**, no. 25–26, pp. 7727–7751.
- [146] J. Plante and S. Dubowsky, "On the Nature of Dielectric Elastomer Actuators and Its Implications for Their Design," *Proc. SPIE 6168, Smart Struct. Mater. 2006 Electroact. Polym. Actuators Devices*, 2006, **6168**, pp. 61681J 1–11.
- [147] G. Kofod, "The static actuation of dielectric elastomer actuators: how does pre-stretch improve actuation?," *J. Phys. D. Appl. Phys.*, Nov. 2008, **41**, no. 21, p. 215405.
- [148] M. Soleimani and C. Menon, "Preliminary investigation of a balloon-shape actuator based on electroactive elastomers," *Smart Mater. Struct.*, Apr. 2010, **19**, no. 4, p. 047001.

## **Appendix.**

### **Nonlinear Control and Simulation of a Dielectric Elastomer Actuator-based Compression Bandage on Flexible Human Calf**

This appendix chapter aims to present a preliminary work toward a future improving aspect of DEA-based active compression bandage. Analytical models are adapted from chapters 3 and 4 to design and simulate a nonlinear controller based on the input-output linearization control strategy. This chapter is adapted from the following publication and has been slightly modified to comply with the format of this thesis:

Pourazadi S, Moallem M, Menon C. Nonlinear control and simulation of a dielectric elastomer actuator-based compression bandage on the flexible human calf. International Conference on Bioinformatics and Biomedical Engineering 2017 Apr 26 (pp. 289-300). Springer, Cham.

#### **Abstract**

Compression bandages are widely used for a number of disorders associated with lower human leg including edema, orthostatic hypotension, and deep vein thrombosis. In recent years, dielectric elastomer actuators (DEAs) are proposed to be used as an active compression bandage to potentially augment or treat the lower leg disorders. DEA bandage applies a variable compression around the leg that varies upon voltage stimulation in the DEA. Prediction and control of the DEA behavior interacting with a soft object like a human calf can be a very challenging and complex problem. In this appendix, a nonlinear analytical model is developed to represent the interaction between a silicon-based DEA compression bandage and soft human calf. An input-output linearization control strategy is utilized to design a controller that applies a desired compression profile to the calf. Lastly, MATLAB Simulink is used to simulate and illustrate the performance of the controller and the model.

## Introduction

DEA-based compression bandages were proposed in chapter 3 and 4 of this thesis with an aim to overcome some of the shortcomings of the currently available compression therapy devices such as compression bandages, compression stockings, and intermittent pneumatic compression devices. DEA compression bandage potentially provides a better compliance for the patients and help to alter the amount of compression based on the need of the body and also apply a different range of compression for a wide group of individuals with different leg dimensions and hemodynamic characteristics. Moreover, DEA bandages can actuate very fast and are very lightweight and portable.

As mentioned in chapter 3 and 4, the quantity of external compression is an important factor in augmentation and treatment of the mentioned lower leg disorders. For instance, it has been suggested that a graded compression of 18 mmHg at the ankle, 14 mmHg at mid-calf, and 8 mmHg at the knee is required to optimize the venous blood flow in the lower leg [1]. Also, it is shown that a compression of 35–40 mmHg at the ankle is required to prevent edema in patients with intense venous disease [2]. Thus, the bandages used for compression therapy should be designed to apply the proper range of compression. In doing so, as suggested by Stenger et. al. volumetric changes of the leg as a result of applied compression should be considered prior to the design of compressive elastic bandages [3].

In this appendix, first, the behavior of the soft human calf, which was introduced in chapter 4, is presented in a slightly modified model. Next, this model is integrated with the DEA nonlinear model to describe the interaction between the DEA and the soft human calf. An input-output linearization control method is used to control the nonlinear behavior of the DEA on a human calf. Finally, the analytical model and the controller are implemented in MATLAB Simulink.

## Analytical Modeling

An illustration of the DEA compression bandage is shown in figure A1(a). DEA bandage applies a compression on the calf and the calf deforms based on the amount of this compression. This deformation in the calf results in a variation in the DEA applied

compression in turn. In order to explain this coupled behavior, the mathematical model for each component should be defined.

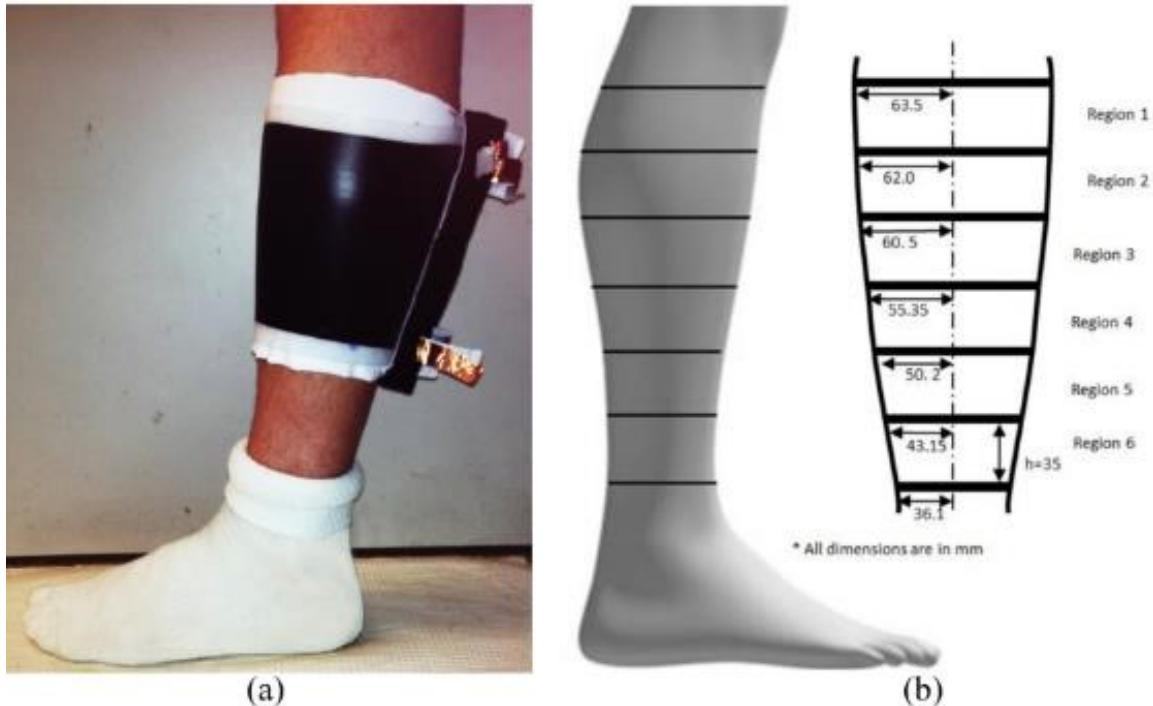


**Figure A1.** DEA bandage and the human calf. (a) A prototype of DEA active compression bandage. (b) Dimensions for an average human calf.

## Human calf

The human calf compresses upon application of pressure. The calf volume changes considerably with the application of an external compression and is usually determined by the calf compliance  $C$ :

$$C = \frac{\delta\Delta V}{\delta P} \quad (1)$$

where  $\delta\Delta V$  and  $\delta P$  represent volume and external compression changes. Calf compliance can be measured using different methods [4]–[11]. Common clinical method of calf compliance measurement is by monitoring the calf volume changes using plethysmography while applying an external compression proximal to the knee with congestion cuffs [4]–[8]. In this method, it is assumed that the volume change in the limb is equivalent to the volume change of the underlying venous vessel. This assumption

however, is argued to be not very accurate [11]. Moreover, this method is believed to not precisely predict the compliance of the calf as the external pressure is applied proximal to the knee and not to the calf itself. A more sophisticated method was however used to accurately measure the calf compliance by monitoring cross-sectional changes of the calf under application of an external compression to the calf area [10], [11]. In [12] the compliance data acquired by Thirsk *et al* [11] was used and a term was developed for steady-state radial strain in the calf:

$$\frac{R_i - R_e}{R_i} = \varepsilon_r = a \cdot e^{b \cdot P} + c \cdot e^{d \cdot P} = f(P) \quad (2)$$

where  $\varepsilon_r$  is the radial strain in the calf,  $R_e$  is the calf radius in steady-state,  $R_i$  is the initial calf radius,  $P$  is the external compression on the calf and,  $a, b, c$  and  $d$  are constants that vary for different regions of the calf and are given in [12]. Figure A1(b) shows the average human calf initial radius  $R_i$  for different calf regions [12]. In [10] the calf volumetric response was estimated for a given compression on the calf:

$$\frac{dV}{dt} = \frac{V_e - V}{R_c C_c} \quad (3)$$

where,  $V$ ,  $V_i$ , and  $V_e$  represent the instantaneous, initial and steady-state volume of the calf.  $R_c$  and  $C_c$  are the resistance and compliance in the calf veins and are 3.8s.kPa/% and 1.1 %/kPa respectively. [10]. The study of radius changes is more desirable in this study thus we write (3) in terms of calf radius. Assuming a uniform conical or cylindrical geometry for the calf, the following equations can be written:

$$d \frac{V}{V_i} = 2 \frac{R}{R_i} d \frac{R}{R_i} \quad (8)$$

$$\frac{V}{V_i} = \left( \frac{R}{R_i} \right)^2 \quad (5)$$

$$\frac{\Delta V}{V_i} = 2 \frac{\Delta R}{R_i} \Rightarrow \frac{V_i - V_e}{V_i} = 2 \frac{R_i - R_e}{R_i} \quad (6)$$

where  $R$  is the instantaneous calf radius. Equation (6) is valid considering a uniform geometrical shape for the calf cross-section area [13]. Using (2) in (6) results in:

$$\frac{V_e}{V_i} = 1 - 2f(P). \quad (7)$$

Equation (3) can be written in terms of calf radius using equations (4),(5) and (7):

$$\frac{d\frac{R}{R_i}}{dt} = \frac{\frac{1-2f(P)}{R_i} \frac{R}{R_i}}{2R_c C_c}. \quad (8)$$

Equation (8) describes the calf radius changes for a given external compression.

## **Silicon DEA bandage**

The total compression applied by the DEA bandage has two components, the mechanical pressure which is the compression resulting from the mechanical stress in the DEA before actuating the DEA, and the actuation pressure, which is the compression variation while actuating the DEA.

### ***Mechanical component.***

The DEA bandage is assumed to be made out of a flat DEA [14]. This flat DEA can be bent to form a cylindrical bandage with inner and outer radii of  $A$  and  $B$ . This DEA bandage is stretched radially as it is wrapped around the calf radius  $R$  and the following stretch ratios  $\lambda_a$  and  $\lambda_b$  can be obtained:

$$\lambda_a = \frac{R}{A}, \quad \lambda_b = \frac{b}{B} \quad (9)$$

where  $b$  is the DEA outer radii after stretch. Since the geometry of the calf is conical, the DEA undergoes different stretch ratios along the height of the calf. As the stretch ratio of the DEA bandage  $\lambda$  changes the amount of its compression on the calf also changes. The amount of this compression is obtained using the following equation [15]:

$$P_m = \int_{\lambda_b}^{\lambda_a} \frac{\mu_1(\lambda^{\alpha_1} - \lambda^{-\alpha_1}) + \mu_2(\lambda^{\alpha_2} - \lambda^{-\alpha_2})}{\lambda(\lambda^2 - 1)} d\lambda \quad (10)$$

where,  $\mu_1, \mu_2, \alpha_1, \alpha_2$  are the ogden parameters for the DEA hyperelastic material which are obtained from tensile tests [14], [15].

### ***Electrical component.***

The DEA electrical circuit can be simplified as shown in figure A2. The DEA can be represented with a simple capacitance and is obtained from[16]:

$$C = \frac{2\pi\epsilon_0\epsilon_r L}{\ln\left(\frac{b}{R}\right)} \quad (11)$$

where,  $\epsilon_0$  is the vacuum permittivity,  $\epsilon_r$  is the relative permittivity and L is the height of the DEA cylinder or the calf section. As the DEA compression on the calf changes the calf radius changes and as a result the DEA capacitance changes based on (11). The DEA charging circuit shown in figure A2 is an RC circuit with a variable capacitance. Thus, it can be written:

$$V_{in} = V_c + R_{elec} \left( C \frac{dV_c}{dt} + V_c \frac{dC}{dt} \right) = V_c \left( 1 + R_{elec} \frac{dC}{dt} \right) + R_{elec} C \frac{dV_c}{dt}. \quad (12)$$

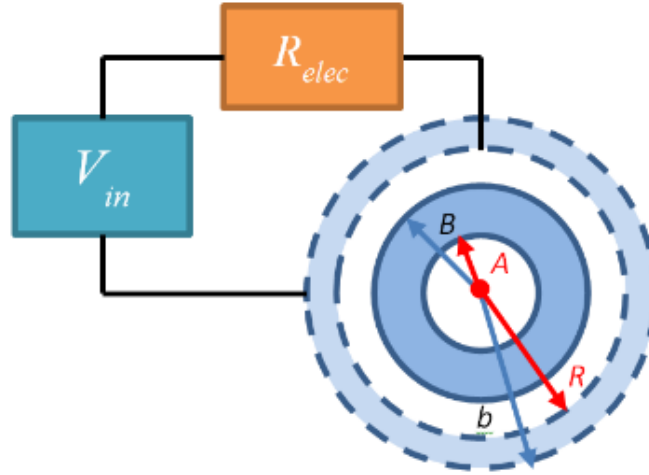


**Figure A2. The electrical circuit and geometry of the DEA bandage.**

$R_{elec}$  represents the DEA equivalent series resistance plus other resistive dissipations in the charging circuit and  $V_c$  is the voltage across the DEA.

### ***Electromechanical component.***

The DEA actuation pressure is calculated from the following equation [15]:

$$P_a = \frac{\epsilon_0\epsilon_r V_C^2}{2\ln^2(b/R)} \frac{b^2 - R^2}{R^2 b^2}. \quad (13)$$

As discussed earlier the total DEA compression on the calf is composed of  $P_a$  and  $P_m$  and is given by:

$$P = P_m - P_a \quad (14)$$

As it can be realized for Equation (14), the DEA compression is reduced upon actuation. Thus, the radius of the calf is increased which in turn results in an increase of the DEA mechanical pressure.

Summarizing the developed analytical equations in this section, a system of coupled, nonlinear equations should be solved to explain the behavior of the DEA performance on the soft human calf:

$$\begin{cases} \frac{dR}{dt} = \frac{\frac{1-2f(P)}{R} \frac{R}{R_i}}{2R_c C_c} \\ \frac{dV_c}{dt} = \frac{V_{in} - V_c (R_{elec} \frac{dC}{dt} + 1)}{R_{elec} C} \\ P = P_m - P_a \end{cases} \quad (15)$$

The following section presents a nonlinear control strategy to design a controller in order for the DEA bandage to track a desired compression on the calf.

## Controller Design

As mentioned earlier, it is interesting to have a compression bandage that provides a desirable and controlled compression profile on the calf. Equation (14) shows that the DEA compression can be controlled by the actuation pressure and using the input voltage to the DEA. However, the system of equations in (15) is nonlinear and it can be challenging to design a controller that tracks a desired compression profile. While a linear control design can be used to obtain a controller for a small linearized region, more sophisticated, nonlinear controller design methods can be used to obtain a controller for a wider range of the system operation. In order to address the nonlinearities in the system an input-output linearizer controller [17], [18] is utilized in this chapter. Using (15) and considering the DEA input voltage  $V_{in}$  as the system input and the DEA bandage compression  $P$  as the output, a controller can be designed. A nonlinear input control law should be calculated to remove the nonlinearities from the system.

Differentiating the output yields:

$$\dot{y} = \dot{P} = \dot{P}_m - \dot{P}_a = \frac{df(R)}{dt} - \frac{df(V_c, R)}{dt}. \quad (16)$$

For simpler differentiation,  $P_m$  and  $P_a$  which are nonlinear functions of calf radius  $R$  and/or DEA voltage  $V_C$  can be estimated using:

$$P_m = f(R) \approx p_0 R^3 + p_1 R^2 + p_2 R^1 + p_4 R^0 \quad (9)$$

$$P_a = f(V_C, R) \approx \varepsilon_0 \varepsilon_r V_C^2 (k_0 R^{k_1} + k_2) \quad (18)$$

where,  $p_0, p_1, p_2, p_3, k_0, k_1,$  and  $k_2$  are constants and are given in Table A1.

**Table A1. Constants obtained for equation (17) and (18).**

Parameter	Value	Unit	Parameter	Value	Unit
$p_0$	6.4e3	Pa/m <sup>3</sup>	$k_0$	9.3e-6	1/m <sup>k<sub>1</sub>+2</sup>
$p_1$	-2.9e4	Pa/m <sup>2</sup>	$k_1$	-3.9	-
$p_2$	4.7e4	Pa/m	$k_2$	4.0e4	1/m <sup>2</sup>
$p_3$	-2.4e4	Pa			

Using (12), (17) and (18) in (16) yields:

$$\frac{dy}{dt} = \frac{df(R)}{dt} - 2\varepsilon_0 \varepsilon_r V_C (k_0 R^{k_1} + k_2) \frac{V_{in} - V_C (R_{elec} \frac{dC}{dt} + 1)}{R_{elec} C} + \varepsilon_0 \varepsilon_r V_C^2 (k_0 k_1 \frac{dR}{dt} R^{k_1-1}). \quad (19)$$

In (19), if the input  $V_{in}$  is selected wisely the nonlinearities can be removed. Let us choose:

$$V_{in} = \frac{(-v + \frac{df(R)}{dt} + \varepsilon_0 \varepsilon_r V_C^2 (k_0 k_1 \frac{dR}{dt} R^{k_1-1}))}{2\varepsilon_0 \varepsilon_r V_C (k_0 R^{k_1} + k_2)} R_{elec} C + V_C (R_{elec} \frac{dC}{dt} + 1). \quad (20)$$

By substituting (20) into (19), the output derivative  $dP/dt = dy/dt$  is obtained as:

$$\frac{dP}{dt} = \frac{dy}{dt} = v. \quad (21)$$

To make the DEA compression  $P$  track a desired profile  $P_d(t)$  let us choose:

$$v = \frac{dP_d}{dt} - k(P - P_d). \quad (22)$$

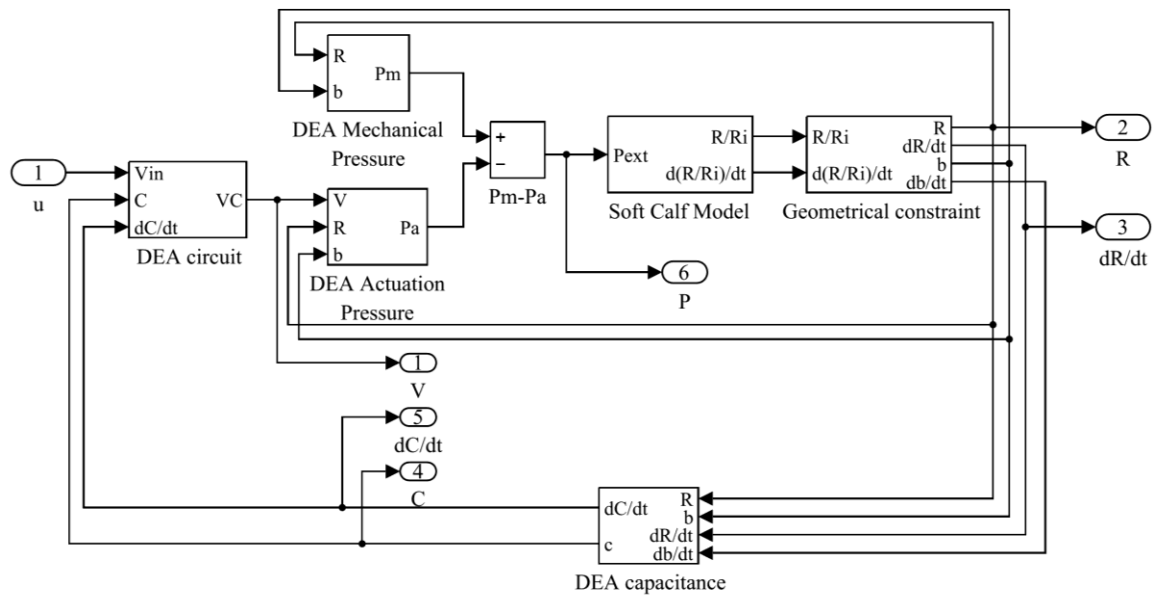
By setting the error as  $e = P - P_d$  and using (21) and (22):

$$\frac{de}{dt} + ke = 0 \quad (23)$$

which ensures the stability of the system by the convergence of the error to zero for positive  $k$ . However, it should be noted that the selected control input in (20) is singular for  $V_C=0$ . Thus, at all times the desired pressure should be in a way to require  $V_C \neq 0$ .

## Simulations and Results

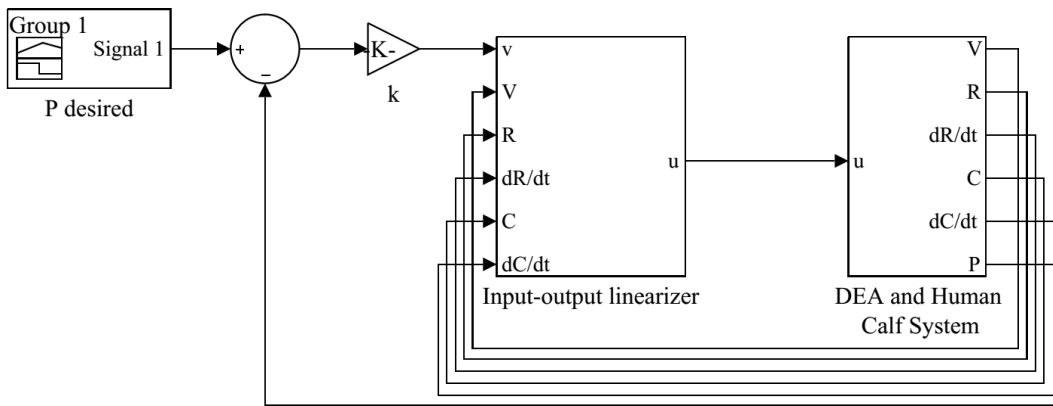
The analytical equations and the controller developed in section 2 and 3 were simulated in MATLAB Simulink. Figure A3 shows the DEA bandage and the soft human calf model block diagram.



**Figure A3. DEA bandage and soft human calf system block diagram model.**

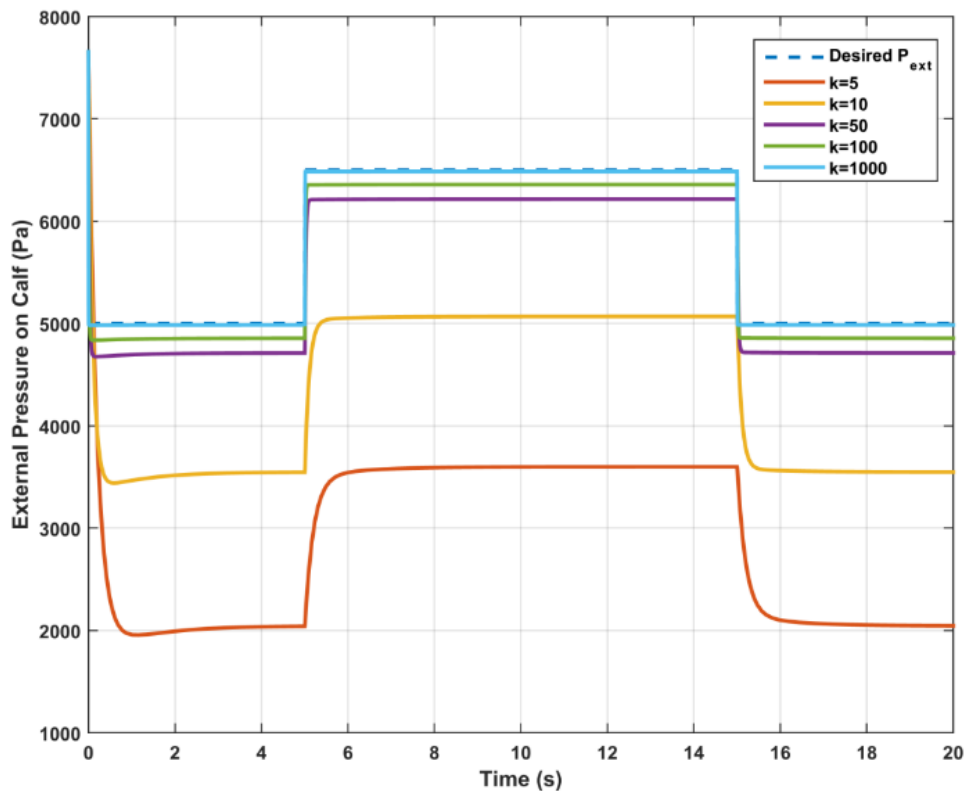
For this study, a silicone DEA with ogden parameters similar to [14] was used. The integration in (10) was solved using a Simpson's numerical integration method constructed into a custom MATLAB *S-function*.

Figure A4 shows the nonlinear controller block diagram. A desired compression profile can be set up and by tuning the controller gain  $k$  the DEA bandage can be controlled to exert the desired compression profile on the calf.



**Figure A4. Nonlinear Controller block diagram.**

The block diagram in figure A4 was simulated in Simulink for a duration of 20 seconds and using the ode23t solver with automatic variable step sizes. The DEA bandage was considered to be wrapped around the calf section region 4 (see figure A1(b)) with a height of 35mm.



**Figure A5. Step compression profile and the performance of the DEA for different controller gains  $k$ .**

Figure A5 shows the performance of the controlled DEA for a compression profile with a step increase and decrease. It is shown that as the gain  $k$  is increased the error between the actual and desired compression on the calf is reduced and the DEA bandage tracks the desired profile faster.

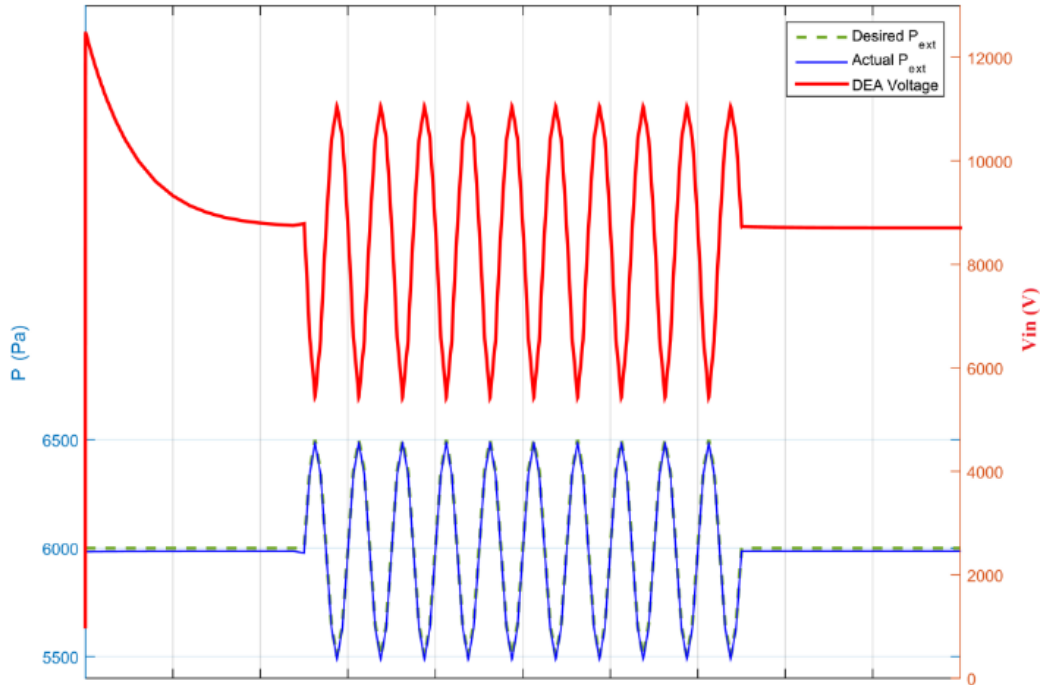


**Figure A6. DEA bandage tracking a 1Hz sine wave compression profile with  $k=1000$ . The input voltage to the DEA  $V_{in}$  is shown on the secondary axes of the plot.**

Figure A6 shows the simulation of the controlled system for an alternating compression profile. The figure shows that the design is capable of controlling the DEA to track an alternating compression profile with errors smaller than 0.05%. The required voltage to actuate the DEA  $V_{in}$  is plotted on the secondary axes of figure A6. Voltages between 5 to 11kV are required to keep the DEA track the compression profile.

## Conclusion

In this chapter, the behavior of the active compression bandage made out of silicone dielectric elastomer actuator (DEA) was studied on a simulated human leg. The DEA active compression bandage could potentially be used in the treatment of different types of disorders associated with venous pooling in lower extremities such as orthostatic hypotension and edema. External compression on the lower leg helps balance the

capillary filtration and venous return which in turn results in the reduction of venous pooling and normalizing the blood return. The literature suggests that a controlled compression on the calf is desirable in order to augment and treat the lower leg disorders.

In this chapter, analytical models were studied for the DEA bandage and flexible human calf. Due to the calf flexibility and compressibility, the size of the calf changes upon application of external compression by the DEA bandage which in turn affects the compression created by the bandage. A system of nonlinear and coupled equations was developed to represent the DEA interaction with the human calf. An input-output linearization control technique was used to design a controller for the DEA behavior on the calf. The designed controller and the system were implemented in MATLAB Simulink for simulations. Simulations were performed for a desired step and alternating compression profiles. It was shown that using the designed controller, the DEA was able to track the desired compression profile with errors less than 0.05%.

## References

- [1] B. Sigel, A. Edelestein, L. Savitch, J. Hasty, and W. Felix, "Types of compression for reducing venous stasis," *Arch. Surg.*, 1975, **110**, pp. 171–5.
- [2] R. Stemmer, "Ambulatory elasto-compressive treatment of the lower extremities particularly with elastic stockings," *Der Kassenarzt*, 1969, **9**, pp. 1–8.
- [3] M. B. Stenger, A. K. Brown, S. M. C. Lee, J. P. Locke, and S. H. Platts, "Gradient Compression Garments as a Countermeasure to Post-Spaceflight Orthostatic Intolerance," *Aviat. Space. Environ. Med.*, Sep. 2010, **81**, no. 9, pp. 883–887.
- [4] J. R. Halliwill, C. T. Minson, M. J. Joyner, and R. John, "Measurement of limb venous compliance in humans: technical considerations and physiological findings," *J. Appl. Physiol.*, 1999, **87**, no. 4, pp. 1555–1563.
- [5] K. D. Monahan, F. a Dinunno, D. R. Seals, and J. R. Halliwill, "Smaller age-associated reductions in leg venous compliance in endurance exercise-trained men.," *Am. J. Physiol. Heart Circ. Physiol.*, Sep. 2001, **281**, no. 3, pp. H1267-73.
- [6] K. D. Monahan and C. a Ray, "Gender affects calf venous compliance at rest and during baroreceptor unloading in humans.," *Am. J. Physiol. Heart Circ. Physiol.*, Mar. 2004, **286**, no. 3, pp. H895-901.
- [7] a Lipp, P. Sandroni, J. E. Ahlskog, D. M. Maraganore, C. W. Shults, and P. a Low, "Calf venous compliance in multiple system atrophy.," *Am. J. Physiol. Heart Circ. Physiol.*, 2007, **293**, no. 1, pp. H260-5.

- [8] J. a Sielatycki, S. Shamimi-Noori, M. P. Pfeiffer, and K. D. Monahan, "Adrenergic mechanisms do not contribute to age-related decreases in calf venous compliance," *J. Appl. Physiol.*, 2011, **110**, no. 1, pp. 29–34.
- [9] T. Binzoni, V. Quaresima, M. Ferrari, E. Hiltbrand, and P. Cerretelli, "Human calf microvascular compliance measured by near-infrared spectroscopy.," *J. Appl. Physiol.*, 2000, **88**, no. 2, pp. 369–372.
- [10] M. Zicot, K. H. Parker, and C. G. Caro, "Effect of positive external pressure on calf volume and local venous haemodynamics.," *Phys. Med. Biol.*, 1977, **22**, no. 6, pp. 1146–1159.
- [11] R. B. Thirsk, R. D. Kamm, and a H. Shapiro, "Changes in venous blood volume produced by external compression of the lower leg.," *Med. Biol. Eng. Comput.*, Sep. 1980, **18**, no. 5, pp. 650–6.
- [12] S. Pourazadi, S. Ahmadi, and C. Menon, "On the design of a DEA-based device to potentially assist lower leg disorders: An analytical and FEM investigation accounting for nonlinearities of the leg and device deformations," *Biomed. Eng. Online*, 2015, **14**, no. 1.
- [13] R. J. Whitney, "The measurement of volume changes in human limbs," *J. Physiol.*, 1953, **121**, no. 1, pp. 1–27.
- [14] S. Pourazadi, S. Ahmadi, and C. Menon, "Towards the development of active compression bandages using dielectric elastomer actuators," *Smart Mater. Struct.*, Jun. 2014, **23**, no. 6, p. 065007.
- [15] S. Ahmadi, a Camacho Mattos, a Barbazza, M. Soleimani, P. Boscariol, and C. Menon, "Fabrication and performance analysis of a DEA cuff designed for dry-suit applications," *Smart Mater. Struct.*, Mar. 2013, **22**, no. 3, p. 035002.
- [16] D. A. Bell, *Fundamentals of electric circuits*, 7th editio. New York: Oxford University Press, 2009.
- [17] S. H. Žak, *Systems and control*. Oxford University Press, 2003.
- [18] J. J. E. Slotine and W. Li, *Applied Nonlinear Control*. Prentice Hall, 1991.